

N72-22207

**NASA TECHNICAL
MEMORANDUM**

NASA TM X-64642

February 1972

NASA TM X-64642

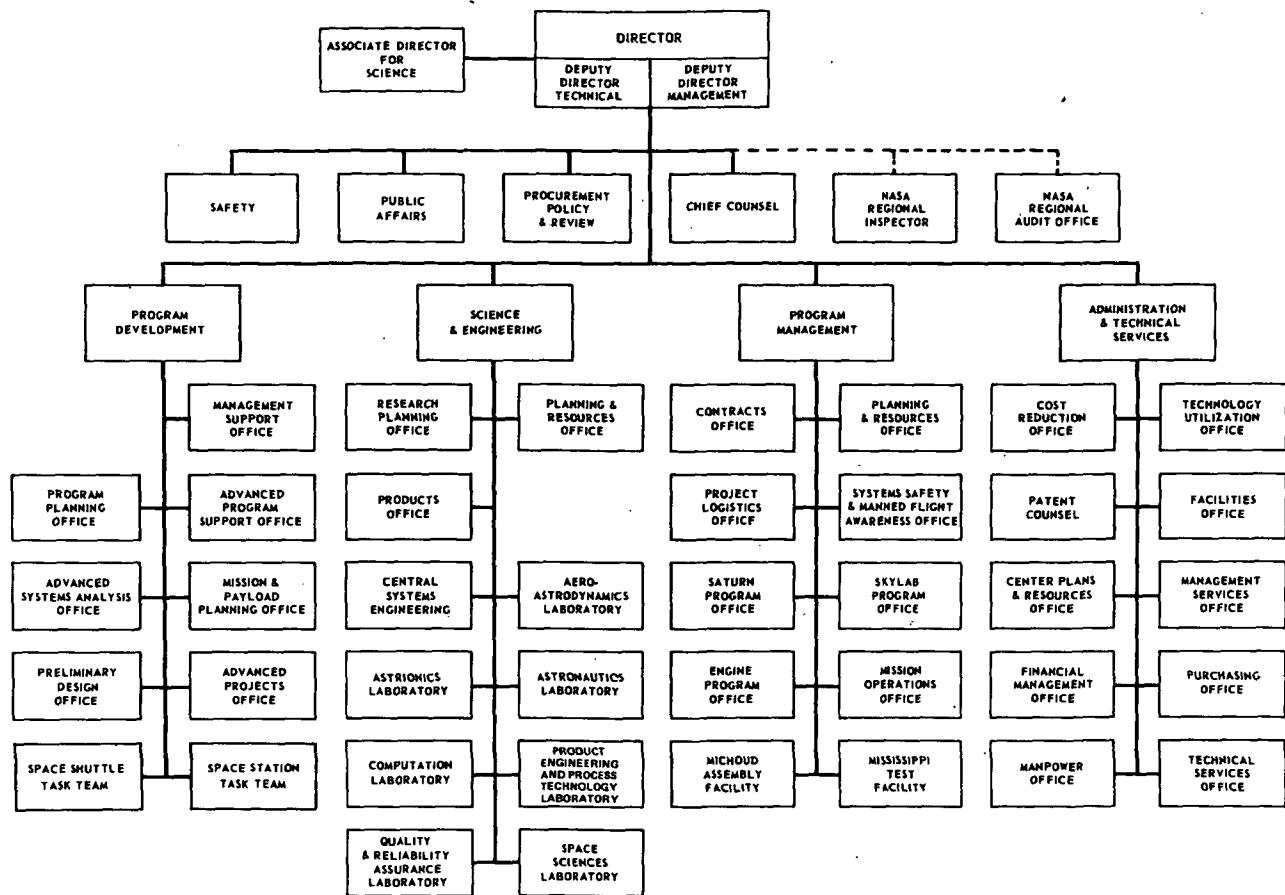
**CASE FILE
COPY**

**ELECTRICAL POWER SYSTEMS RESEARCH
AT MSFC**

**RESEARCH ACHIEVEMENTS REVIEW
VOLUME IV REPORT NO. 4**

SCIENCE AND ENGINEERING DIRECTORATE
GEORGE C. MARSHALL SPACE FLIGHT CENTER
MARSHALL SPACE FLIGHT CENTER, ALABAMA

GEORGE C. MARSHALL SPACE FLIGHT CENTER



RESEARCH ACHIEVEMENTS REVIEWS COVER
THE FOLLOWING
FIELDS OF RESEARCH

- Radiation Physics
- Thermophysics
- Chemical Propulsion
- Cryogenic Technology
- Electronics
- Control Systems
- Materials
- Manufacturing
- Ground Testing
- Quality Assurance and Checkout
- Terrestrial and Space Environment
- Aerodynamics
- Instrumentation
- Power Systems
- Guidance Concepts
- Astrodynamics
- Advanced Tracking Systems
- Communication Systems
- Structures
- Mathematics and Computation
- Advanced Propulsion
- Lunar and Meteoroid Physics

PREFACE

The Research Achievement Reviews document research accomplished by the laboratories of Marshall Space Flight Center. Each review covers one or two fields of research and attempts to present the results in a form readily useable by specialists, system engineers, and program managers.

Reviews of this fourth series are designated Volume IV and will span the period from May 1970 through May 1972.

In accordance with NASA policy the International System of Units (SI Units), as defined in NASA SP-7012, are used in this publication.

The papers in this report were presented March 25, 1971.

William G. Johnson
Director
Research Planning Office

Page intentionally left blank

CONTENTS...

INTRODUCTION TO ELECTRIC POWER SYSTEMS RESEARCH

Page

By C. B. Graff	1
----------------------	---

SKYLAB ELECTRICAL POWER SYSTEM

By Roy Lanier, Jr.	Page
--------------------	------

SUMMARY	3
INTRODUCTION	3
MISSION RELATED DESIGN CONSIDERATIONS	4
SKYLAB EPS	4
AM EPS	5
ATM EPS	7
SKYLAB EPS PERFORMANCE	10
CONCLUSIONS	11

LIST OF ILLUSTRATIONS

Figure	Title	Page
1.	Skylab electrical power subsystems	3
2.	Skylab electrical power subsystems schematic	5
3.	AM electrical power system	6
4.	ATM electrical power system	8
5.	ATM EPS equivalent circuit	9
6.	ATM EPS characteristics	9
7.	Modular power subsystem reliability	11

CONTENTS (Continued) . . .

ANALYSIS OF EFFECTS OF SHADOWED AND OPEN SOLAR CELLS ON OWS SOLAR CELL ARRAY PERFORMANCE

By J. L. Miller

	Page
ABSTRACT	13
SUMMARY	13
LIST OF SYMBOLS	13
INTRODUCTION	14
ANALYTICAL METHOD	14
TEST METHOD FOR OBTAINING SINGLE CELL REVERSE BIAS DATA	16
REVERSE BIAS TEST RESULTS AND INTEGRATION WITH THERMAL ANALYSIS DATA	18
ANALYSIS OF THE "HOT SPOT" PHENOMENON	19
CONCLUSIONS AND RECOMMENDATIONS	26
FUTURE EFFORTS	27
REFERENCES	27

LIST OF ILLUSTRATIONS

Figure	Title	Page
1.	M \times N string matrix and V-I characteristic	15
2.	Composite V-I characteristic for series string	15
3.	Composite V-I characteristic for parallel group	15
4.	Composite V-I characteristic of an [M \times (N-1)] cell matrix and an [(M-1) \times 1] submodule in series	16
5.	Test setup schematic for reverse characteristics test	17
6.	Dark leakage distribution for 34 cells at selected voltages	18
7.	Temperature versus power dissipated curve from thermal analysis	19
8.	Steady-state reverse voltage curves for high leakage cell 9-1	20
9.	Steady-state reverse voltage curves for low leakage cell 6-1	20

CONTENTS (Continued)...

Figure	Title	Page
10.	Voltage breakdown, dark and illuminated curves, cell 4-1	21
11.	Dark and illuminated reverse characteristics of cell 10-1	21
12.	Normalized V-I and P_R curves at 100°C	22
13.	Normalized shadowing, 1 × 154 string, at 100°C	24
14.	Normalized open cell and shadowing, 2 × 154 string, at 100°C	25
15.	Normalized open cell, 4 × 154 string, at 100°C	25
16.	Normalized shadowing, 4 × 154 string, at 100°C	26

**THE USE OF THE SOLAR CELL DARK CHARACTERISTIC FOR CHECKOUT
OF LARGE AREA SOLAR ARRAYS**

By W. L. Crabtree

	Page
INTRODUCTION	29
DARK CHARACTERISTIC AND PHOTOVOLTAIC CHARACTERISTIC OF SILICON SOLAR CELLS	29
FEASIBILITY TESTS	31
ATM DARK CHARACTERISTIC TEST SETUP	33
DARK CHARACTERISTIC CHECKOUT OF THE ATM	33
CONCLUSIONS	35

LIST OF ILLUSTRATIONS

Figure	Title	Page
1.	ATM solar cell array	29
2.	Solar cell equivalent circuit	30
3.	Comparison of equivalent circuits for a solar cell under illuminated and nonilluminated conditions	30
4.	Comparison of photovoltaic and dark forward characteristics	31
5.	Temperature versus time at three current levels for ATM solar cell module	31

CONTENTS (Continued) . . .

Figure	Title	Page
6.	Current versus voltage for ATM solar cell module	32
7.	Dark I-V curves at 25° C for an ATM panel with a varying number of modules in parallel	32
8.	Effect of various line resistance values on dark I-V characteristics	33
9.	Effect of various shunt resistance values on dark I-V characteristics	33
10.	Dark I-V checkout system	34

NICKEL-CADMIUM BATTERY AND CELL INVESTIGATION FOR APOLLO TELESCOPE MOUNT (ATM) APPLICATIONS

By L. E. Paschal

		Page
ABSTRACT	37
SUMMARY	37
INTRODUCTION	37
TEST PROGRAM	38
TEST RESULTS	39
CONCLUSIONS	56
RECOMMENDATIONS	58
REFERENCE	58

LIST OF TABLES

Table	Title	Page
1.	Nickel-Cadmium Cell Types	38
2.	Absolute Battery Capacity	53

LIST OF ILLUSTRATIONS

Figure	Title	Page
1.	Initial charge regime — AB09 battery	39
2.	Initial charge regime — cell characteristics, AB09 battery (cycle 247)	40

CONTENTS (Continued) . . .

Figure	Title	Page
3.	Recommended charge regime as a result of initial AB09 tests	40
4.	Battery characteristics — cell matching effectiveness	41
5.	Voltage level as a function of temperature	41
6.	AB12 average cycle efficiencies	42
7.	AB12 cells average cycle efficiency — 30° C, constant current charge only	43
8.	AB12 average charge voltage, state-of-charge characteristics — 0.75C	43
9.	Thermal evaluation test layout	44
10.	Thermal characteristic — 30° C, charge from 30-percent DOD	45
11.	Thermal characteristic — 30° C, open circuit after charge	46
12.	Thermal characteristic — 30° C, discharge 30-percent DOD	46
13.	Thermal characteristic — 30° C, MSFC regime	47
14.	Thermal characteristic — 30° C, MSFC regime, no third electrode	47
15.	ATM test cycle — AB12 battery	48
16.	Recharge characteristics — AB12 battery	49
17.	Third-electrode signal for 24 cells at 20° C — cycles 62 and 63, load resistance 150 Ω (AB12 cells)	49
18.	Third-electrode signals for a single cell at 20° C and varying load resistances (AB12 cell)	49
19.	Equivalent third-electrode circuit	50
20.	Internal resistance characteristics for cell 21 at 20° C (AB12 cell)	51
21.	Internal resistance characteristics for cell 7 at varying temperatures and a particular state-of-charge (AB12 cell)	51
22.	Internal resistance characteristics for three cells at a particular state-of-charge (AB12 cells)	52
23.	Expected performance of ATM Ni-Cd batteries	53
24.	Battery capacity as a function of discharge rates — AB09 battery	54
25.	Battery capacity as a function of temperature — AB12 battery (0, 10, 20, and 30° C)	55

CONTENTS (Continued) . . .

Figure	Title	Page
26.	Battery capacity as a function of temperature — AB12 battery (0 and 20°C)	55
27.	Battery capacity recovery as a result of complete battery discharge — AB12 battery	56
28.	Battery capacity recovery as a result of trickle charge tests	57

LOAD SHARING BETWEEN PARALLEL OPERATING DC POWER MODULES

By Robert Kapustka

		Page
SUMMARY		59
INTRODUCTION		59
PROBLEM DEFINITION		59
TYPICAL SOLUTIONS		59
LOAD SHARING ON THE ATM		60
FUTURE CONSIDERATIONS		61

LIST OF TABLES

Table	Title	Page
1.	Methods of Power Sharing	60
2.	Reduction of Feedback Equation	61

LIST OF ILLUSTRATIONS

Figure	Title	Page
1.	Power unbalance from variation in regulator output characteristics	59
2.	Simplified feedback diagram for remote sensing and programmed impedance	60

MICROWAVE POWER TRANSMISSION CONSIDERATIONS FOR EARTH ORBITAL SPACE MISSIONS

By W. J. Robinson, Jr.

Page
63

CONTENTS (Continued) . . .

LIST OF TABLES

Table	Title	Page
1.	Comparison of Power Output and Efficiency of Microwave Rectifiers	65
2.	Demonstrated and Expected Efficiencies of the Elements of a Microwave Power Transmission System	66

LIST OF ILLUSTRATIONS

Figure	Title	Page
1.	Transfer of electrical power in space	63
2.	Components of a microwave power transmission system	64
3.	Microwave power supply	65
4.	Microwave antenna	66

LARGE-AREA LUNAR SURFACE SOLAR ARRAY

By J. L. Miller

	Title	Page
SUMMARY	67
PROGRAM DEFINITION	67
ARRAY DESIGN CONSIDERATIONS	67
SUBSTRATE TRADEOFFS	69
CELL SPALLING	73
CONCLUSIONS	75
REFERENCES	76

LIST OF TABLES

Table	Title	Page
1.	Comparison of Module Characteristics	72
2.	Allowable Adhesive Properties Versus t	76

CONTENTS (Continued) . . .

LIST OF ILLUSTRATIONS

Figure	Title	Page
1.	Schematic of an electric power system for a lunar base (47.5-kW minimum gross power)	68
2.	Relative effectiveness of various solar array configurations	68
3.	Comparison of solar array configurations for a constant total energy output	69
4.	Stowage and unloading of foldout solar array	69
5.	2.5-kW subarray panel pullout integral mounting structure — concept III	70
6.	Substrate for engineering test model no. I — aluminum box-beam frame with a fiberglass lattice diaphragm	70
7.	Substrate for engineering test model no. II — aluminum honeycomb end plates with intermediate flexible kapton modules	71
8.	Substrate for engineering test model no. III — aluminum honeycomb core with graphite filament/fiberglass epoxy face sheets	72
9.	Engineering test model for phase III matrix evaluation	74
10.	Silicon cell effective stress distribution	75
11.	Maximum effective stress in silicon as a function of RTV adhesive thickness	75
12.	Silicon thermal stress — RTV adhesive thickness, $t = 0.254$ mm at a $4.3\text{-}\mu\text{m}$ stress level	76

THERMOELECTRIC GENERATOR TEST PROGRAMS AT MSFC

By L. E. Young

	Page
SUMMARY	77
INTRODUCTION	77
SNAP-19 GENERATOR TEST PROGRAM	77
TEM-9U TUBULAR MODULE TEST PROGRAM	87
PRESENT STATUS AND FUTURE PLANS	95
REFERENCES	96

CONTENTS (Continued) . . .

LIST OF TABLES

Table	Title	Page
1.	Comparison at Maximum Power	83
2.	Comparison at Equal Voltage of 2.6 V	83
3.	Comparison at Equal Current of 6.0 A	83
4.	Comparison at Equal Load Resistance of 0.5 Ω	83
5.	TEM-9U Data Acquisition and Reduction	89

LIST OF ILLUSTRATIONS

Figure	Title	Page
1.	SNAP-19 radioisotope thermoelectric generator, SN 19	78
2.	SNAP-19 cross section and instrumentation	78
3.	SNAP-19 test chamber and test equipment	79
4.	Thermal test cycle (fin root)	80
5.	SNAP-19 parametric test, ambient, fins uninsulated, December 1967 (5667 hr)	81
6.	SNAP-19 parametric test, vacuum, February 1970 (23 420 hr)	82
7.	SNAP-19 power comparison, December 1967 versus February 1970	82
8.	SNAP-19 voltage comparison, December 1967 versus February 1970	82
9.	Peak power versus time (from parametric tests)	84
10.	Seebeck coefficient and internal resistance versus time	85
11.	SNAP-19 power history	86
12.	SNAP-19 internal pressure and ΔT history	86
13.	Temperature versus test time	87
14.	TEM-9U module assembly, less cooling fins	88
15.	Overall dimensions and thermocouple installation — TEM-9U module	88
16.	TEM-9U test console and electronic load bank	89
17.	Simplified schematic of TEM-9U test arrangement	89

CONTENTS (Continued)...

Figure	Title	Page
18.	Endurance test results — normalized	91
19.	TEM-9U parametric test	91
20.	TEM-9U parametric test at constant hot side temperature	92
21.	TEM-9U parametric test at constant thermal input	92
22.	Module impedance versus frequency	93
23.	Step transient test	93
24.	TEM-9U performance with constant heat input — comparison of test data with computer simulation data	96

INCREASED HYDROX FUEL CELL PERFORMANCE

By John R. Morgan

		Page
INTRODUCTION		97
FUEL CELL MODEL DEVELOPMENT		97
LABORATORY TESTING AND RESULTS		98
CONCLUSIONS AND FUTURE PLANS		101

LIST OF ILLUSTRATIONS

Figure	Title	Page
1.	Simplified fuel cell reactions	97
2.	Typical performance curve	98
3.	Simplified model of a gas diffusion electrode	98
4.	Effect of KOH concentration on cathode polarization	99
5.	Humidification effects at 363° K using gas-diffusion electrodes	99
6.	Humidification effects at 373° K using thin-film electrodes	100
7.	Fuel cell system with external humidifier	100
8.	Fuel cell construction using static moisture removal system	100
9.	Fuel cell construction using integral oxygen humidifier	101

CONTENTS (Concluded) . . .

HIGH FREQUENCY DC-TO-DC CONVERSION

By R. M. Acker

	Page
INTRODUCTION	103
ACCOMPLISHMENTS	103
FUTURE EFFORTS	104
CONCLUSIONS	105

LIST OF ILLUSTRATIONS

Figure	Title	Page
1.	DC-to-DC converter no. 1	103
2.	DC-to-DC converter no. 2	103
3.	Transistor voltage and current waveshapes	104

INTRODUCTION TO ELECTRIC POWER SYSTEMS RESEARCH

By

C. B. Graff

After being taken for granted for many years, electric power has become a critical commodity in almost all sections of our country. The demand for electrical power is doubling every decade, and the capability for power generation has not kept pace with this demand nor has new technology been developed to meet the challenge. The same problems are occurring in relation to space power. Over the past several years the battery has been the workhorse, especially for launch vehicles. Fuel cells are used for the longer time requirements of the Apollo spacecraft. Solar array battery systems have been used on many unmanned satellites and radioisotope thermoelectric generators have been used on others.

During the past few years, the development of the Skylab electrical power system has provided a challenging and interesting program. The system for the Apollo Telescope Mount is being developed at the Marshall Space Flight Center (MSFC) and the systems for the Orbital Workshop and Airlock Module is being developed by the McDonnell-Douglas Corporation under contract to and the technical management of MSFC. The power requirement for the combined systems is in excess of 7 kW with a mission time of 8 months. This greatly exceeds the requirement of any previously designed space power system and has resulted in many unique problems. The first five papers in this Research Achievements Review address some of the more interesting of those problems. The papers present the overall system and outline the operation, unique features, and technology required to develop the system and then present in detail some of the problems and their solutions.

Research has been initiated to develop new and improved concepts for electrical power generation, conversion, and distribution to meet the predicted requirements of projected future programs such as the reusable Space Shuttle, the Space Station, and Lunar Surface Bases. The Shuttle will require relatively high levels of power for relatively short periods of time. The power system will be reusable and

capable of short turnaround times over several missions. The Space Station and the Lunar Base must be designed to operate at high power levels continuously for several years under space environmental conditions. A posture must be maintained in electrical power technology that will support an objective evaluation of all candidate systems for space vehicle development programs. Several projects are included in the MSFC power program concerning different energy sources, energy conversion methods, electrical power conditioning regulation, distribution, and control equipment.

Space does not allow all of the projects to be covered in this review. A brief description of some of the projects not being reported upon follows:

- MSFC is planning and preparing facilities to start development testing of a Brayton engine. This unit will be provided by the Lewis Research Center. The Lewis Center along with the Manned Spacecraft Center will participate in the test program.
- Testing and evaluation of thermionic diodes is presently being conducted and a study is in progress to integrate a reactor thermionic power system into a Space Station. This program is being coordinated with the Atomic Energy Commission.
- Long life rechargeable silver zinc batteries are now under test along with primary zinc oxygen systems.
- A power distribution and control system study has recently been initiated to investigate voltage frequency levels, solid state control, data bus interfacing, etc.
- Several projects are in progress to develop power systems components.

Page intentionally left blank

SKYLAB ELECTRICAL POWER SYSTEM

By

Roy Lanier, Jr.

SUMMARY

The Skylab electrical power system (EPS) will be composed of the parallel combination of the Airlock Module (AM) and the Apollo Telescope Mount (ATM) EPS's. Each of these subsystems is capable of supplying almost 4000 W of continuous conditioned power, making the Skylab EPS the largest EPS ever designed for operation in space. The operation of the two subsystems in parallel, their unique features, and their capabilities are discussed.

INTRODUCTION

Skylab is a manned Space Station designed to perform multiple experiments of a scientific and medical nature. This modular Space Station will consist of the Orbital Workshop (OWS), the Airlock Module, the Multiple Docking Adapter (MDA), and the

Apollo Telescope Mount. The Skylab, shown in Figure 1 with the major features of the electrical power system, will be launched aboard a Saturn V launch vehicle and will be manned by the crew of a Command and Service Module (CSM) spacecraft that will be launched later on a Saturn IB launch vehicle. After rendezvous and docking, the CSM will become a part of the Skylab until the crew departs in it to return to earth. As currently planned, the Skylab will be manned for three different periods of up to 56 days over an 8-month operational life. The ATM and the AM each have an electrical power system consisting of solar array sources, nickel-cadmium batteries, and the necessary charging and conditioning equipment. In addition, there are power sources on the Instrument Unit of the Saturn V launch vehicle and on the CSM. However, these will be used only for short periods at the beginning of the mission and at docking and undocking of the CSM and are not discussed herein. The Skylab EPS has

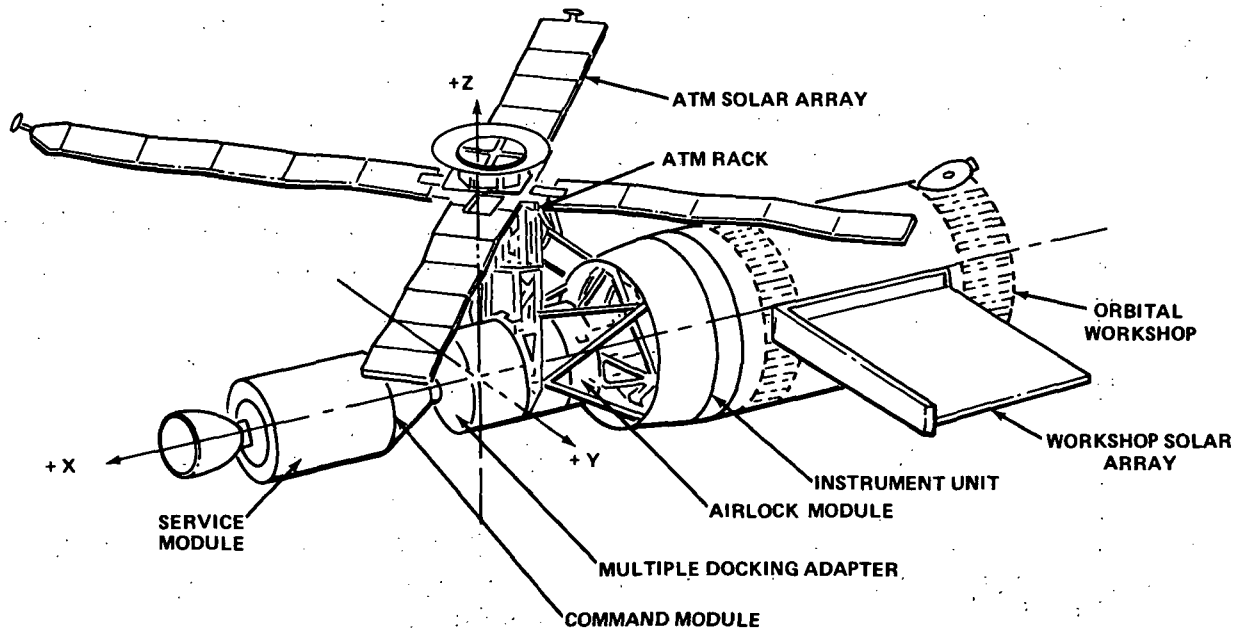


Figure 1. Skylab electrical power subsystems.

evolved from separate developments of the ATM program and the AM-OWS program. As initiated, the two EPS's were developed for different purposes, with different guidelines, and by different NASA centers. However, development and manufacture of both systems are now under the direction of Marshall Space Flight Center (MSFC), and the two operate in parallel. The ATM EPS was originally designed for an 18-month mission. This was later reduced to 2 months, still later increased to 6 months, and finally increased to the current 8-month life requirements. The system was designed to be completely self-dependent during operation, although a man-interface capability was provided. In contrast, the AM EPS was designed for the OWS where man interface was a prime consideration, since one purpose of the OWS experiment was to test the capability of man to operate in space. Furthermore, the AM EPS was designed to operate in parallel and share power with CSM fuel cells. Features designed for this purpose are now used to provide paralleling and sharing between the AM and the ATM EPS's.

MISSION RELATED DESIGN CONSIDERATIONS

The Skylab will operate in a low-earth circular orbit of approximately 385 km with an inclination of 50 deg. Vehicle orientation in a solar inertial mode with all solar arrays directed toward the sun will be the prime mode of operation. During rendezvous and docking maneuvers and during earth resources experiments, however, the vehicle Z-axis will be pointed along the earth local vertical (Z-LV). In the Z-LV mode, the backs of the arrays are directed earthward and the sunlight falls on the arrays at an angle, thus reducing the effective power. The orbit and vehicle orientation impose design considerations on the EPS that affect the sizing and operational restraints of the EPS components. The shadowed portion of the orbit as a function of the beta angle (the angle between the orbit plane and the sun vector) varies from 0 to 36 min. Rechargeable batteries are required for storing energy for use during this eclipse. The orbit time of approximately 94 min means that in the 8-month life of the system, the batteries will experience almost 4000 charge-discharge cycles. Detailed effects of these mission and orbital parameters will be presented in the discussions of particular components.

SKYLAB EPS

Requirements

Basic general requirements for the Skylab EPS have been established at the project level, recognizing the pre-existence of the two subsystems, and are summarized as follows:

1. Configuration — The Skylab EPS shall be comprised of two solar array/battery dc power systems.
2. Power Generation — The Skylab EPS shall have the capability to supply an average of 7530 W to loads while in the solar inertial mode of operation, 6700 W to loads while in the Z-LV earth resources pointing mode of operation, and 1600 W while in the Z-LV rendezvous mode of operation.
3. Power Management — Capability for EPS evaluation and management from the ground station and by the crew shall be provided. Necessary control and display of system functions shall be provided for the astronaut on board.
4. Power Distribution — Power shall be distributed by a two-wire system with no current return through the vehicle structure. A single-point ground reference to structure shall be supplied. Power to mission critical loads shall be distributed through at least two positive isolated buses. All positive polarity lines in the distribution system shall be protected with circuit breakers or fuses.
5. Power Transfer Across Interfaces — Power feeders capable of carrying 2500 W shall be provided between the ATM and AM power distribution subsystems. Power feeders capable of carrying 2000 W shall be provided between the Skylab and the CSM distribution systems.

Implementation

The ATM and AM EPS's are paralleled through the power feeders provided, as shown in Figure 2, and this parallel combination of the two subsystems satisfies the Skylab EPS requirements. Detail characteristics, capabilities, and limitations of the two subsystems are given in the following.

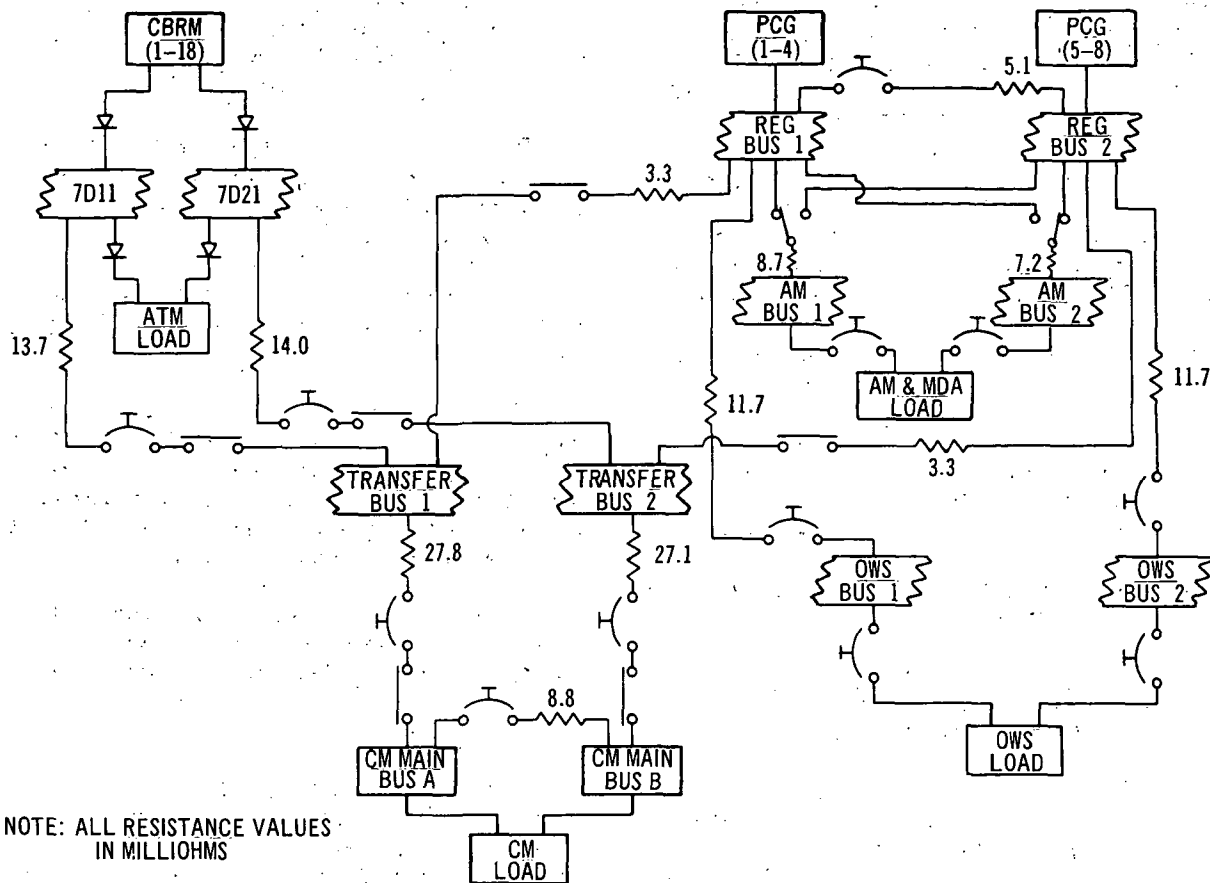


Figure 2. Skylab electrical power subsystems schematic.

AM EPS.

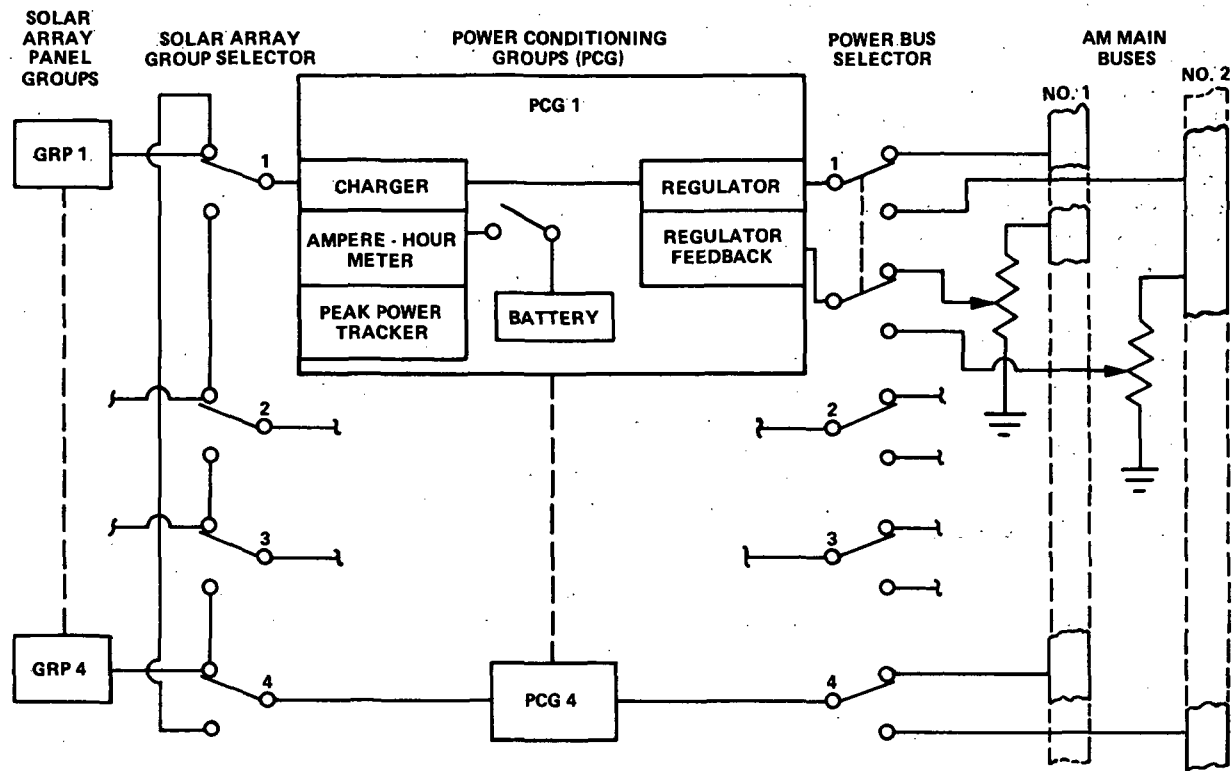
Description

The AM EPS is a modular power system with each module consisting of a solar cell array group that is located on the OWS and a charger, a battery, and a regulator that are located on the AM. The charger, battery, and regulator combination is called a power conditioning group (PCG), and there are eight PCG's with their associated array group source, as shown in Figure 3. The PCG's are located on two PCG modules, each consisting of four PCG's. The PCG modules are mounted on a thermal conditioning plate to provide temperature control. Each PCG regulator feeds, through switches, one of two AM regulator buses.

Power Components

SOLAR ARRAY SYSTEM (SAS)

The SAS for the AM EPS is located on the OWS. It has eight independent power sources, called array groups, mounted on two wings. Each wing contains a half-source for each PCG. Each half-source is composed of 15 modules isolated from each other by diodes. The complete array is rated at 10 496 W in orbit at end of life and at 55°C. Each array group, which feeds 1 of 2 PCG's depending on the position of an array group switch, has 30 solar cell modules connected in parallel. Each module has 616 2- by 4-cm cells with 4 parallel strings of 154 cells each. The solar cell array configuration is shown on the Skylab in Figure 1.



NOTE: GROUPS 1 THROUGH 4 ABOVE TYPICAL FOR
GROUPS 5 THROUGH 8.

Figure 3.. AM electrical power system.

POWER CONDITIONING GROUP

Battery. The AM battery has 30 Eagle Picher Industries, Inc., RSN-36 nickel-cadmium cells connected in series. The cells have individual self-reseating pressure relief valves set to relieve at 14.8×10^5 N/m². The cells are mounted in a magnesium, egg-crate-type case to enable efficient heat removal. The battery case also contains a pressure relief valve set to relieve at 3.4×10^5 N/m². The complete battery has a rated capacity of 33 A-h, but the actual capacity is a function of several variables. One of these variables is the cycle life, and tests are currently in progress to establish capacity versus life cycle curves for the battery. However, the fact that the active cooling is available has led to a charge control scheme for the AM battery that is somewhat different from that used for the ATM battery. The major difference is that it allows a greater recharge fraction, particularly at high temperatures, and a trickle charge is provided after the charge is complete. The charge method chosen is a temperature-dependent constant voltage limit charge to a temperature-dependent overcharge as defined by an

ampere-hour meter in the charger. The battery is designed for a controlled temperature range of 2°C to 38°C with a combination of passive and active cooling provided by the thermal control panel, and for a range of -23°C to 38°C with total passive cooling during unmanned modes of operation. Testing to verify acceptable operation over these temperature ranges is underway.

Charger. The AM charger is designed to handle the entire solar array group power. It uses a buck-type switching circuit to provide power to both the battery and the regulator with the regulator having priority. Excess power above that required by the regulator is supplied to the battery. The charger also contains a redundant peak power tracker for obtaining maximum utilization of the array group power over a wide range of input voltage and current, and two selectable, redundant ampere-hour meters for battery charge control. The peak power tracker reduces the charger output voltage, and thus the battery charging current, when the array group peak power is exceeded. The peak power tracker functions equally well during both solar inertial and Z-LV modes. During periods when array group

power is not sufficient for handling the regulator load, the charger voltage drops to a level at which the battery and array group will share the load. The ampere-hour meter continuously monitors the battery discharge and charge current and requires the charger to return the amount of ampere-hours previously removed from the battery multiplied by a temperature-dependent return factor. The charger switches into a 2-A trickle charge to the battery when the ampere-hour meter signals that the battery has been fully charged.

Regulator. The PCG regulator has a buck-type switching circuit that accepts power from the charger and/or the battery, or directly from the solar array group through a charger bypass switch in a contingency mode. The regulator operates over an input voltage range of 30 to 125 V from these sources. It has a peak output power capability of approximately 1500 W and an output voltage control range of 26 to 30 V no-load, adjustable. Fuses are provided to protect the buses from overvoltage in case of a power transistor short. A shunt load on the bus is electronically switched in when the voltage attempts to go high, thus blowing the fuse and protecting the bus loads from high battery, charger, and solar array voltages. A ganged potentiometer with outputs to all regulators feeding its bus is provided on each of the AM regulator buses. This adjustment feature is used to balance the two buses for sharing of the PCG's and for sharing with the ATM EPS. In addition, a screwdriver adjustment is available to individual regulators for adjustment of their output for sharing with other regulators on the same bus. These manual adjustment features are in contrast to the automatic, fixed voltage power sharing used on the ATM. Each regulator feeds either of the two AM regulator buses, depending on the position of a power selector switch.

Monitoring and Control

As previously noted, the AM was originally designed with plans for a significant astronaut interface from a monitoring and control aspect. This is reflected in the large number of switches and meters provided for astronaut observation and operation. However, except for the voltage adjustment potentiometers previously discussed, these measurements and controls do not interface directly with the PCG's. Instead, they measure the parameters associated with power flow to and from the PCG components and

switch this power to the desired buses. In addition to the onboard measurements, various parameters are telemetered to ground for monitoring and control, if desired, and for postflight scientific analysis.

ATM EPS

Description

The ATM EPS is a modular power system with each module consisting of a solar cell array source and a charger, battery, regulator module (CBRM). There are 18 of these separate modules as shown in Figure 4. Each CBRM contains a battery to supply energy during eclipse portions of the orbit, a charger to condition the solar cell array power and control battery charging, and a regulator to regulate battery and/or cell array voltage and to regulate power drain or sharing between batteries. In addition, the CBRM's contain automatic protection and warning circuits, telemetry and astronaut display circuits for monitoring, a heater control circuit, and control circuits. Each CBRM regulator powers both ATM power buses through diodes as shown in Figure 4.

Power Components

SOLAR ARRAY SYSTEM (SAS)

The ATM SAS has 18 independent solar array power sources mounted on 4 solar wings. Each wing has 4 complete power sources containing 20 solar cell modules and 1 half-power source of 10 solar cell modules. The 4 half-sources are paired in parallel to form 2 solar sources making the total of 18 solar sources for the complete system. The complete array is rated at 10 060 W in orbit at the end of life and at 55°C. Each solar source or solar panel has 20 solar cell modules connected in parallel to supply 1 CBRM. There are two different types of solar cell modules on the ATM. One has 684 2- by 2-cm solar cells with 6 parallel strings of 114 cells each. The other has 228 2- by 6-cm solar cells with 2 parallel strings of 114 cells each. The ATM solar cell array will have half of the solar sources made from 2- by 2-cm cell modules and half of the solar sources made from 2- by 6-cm cell modules. The solar cell array configuration and its output capability are shown on the Skylab in Figure 1.

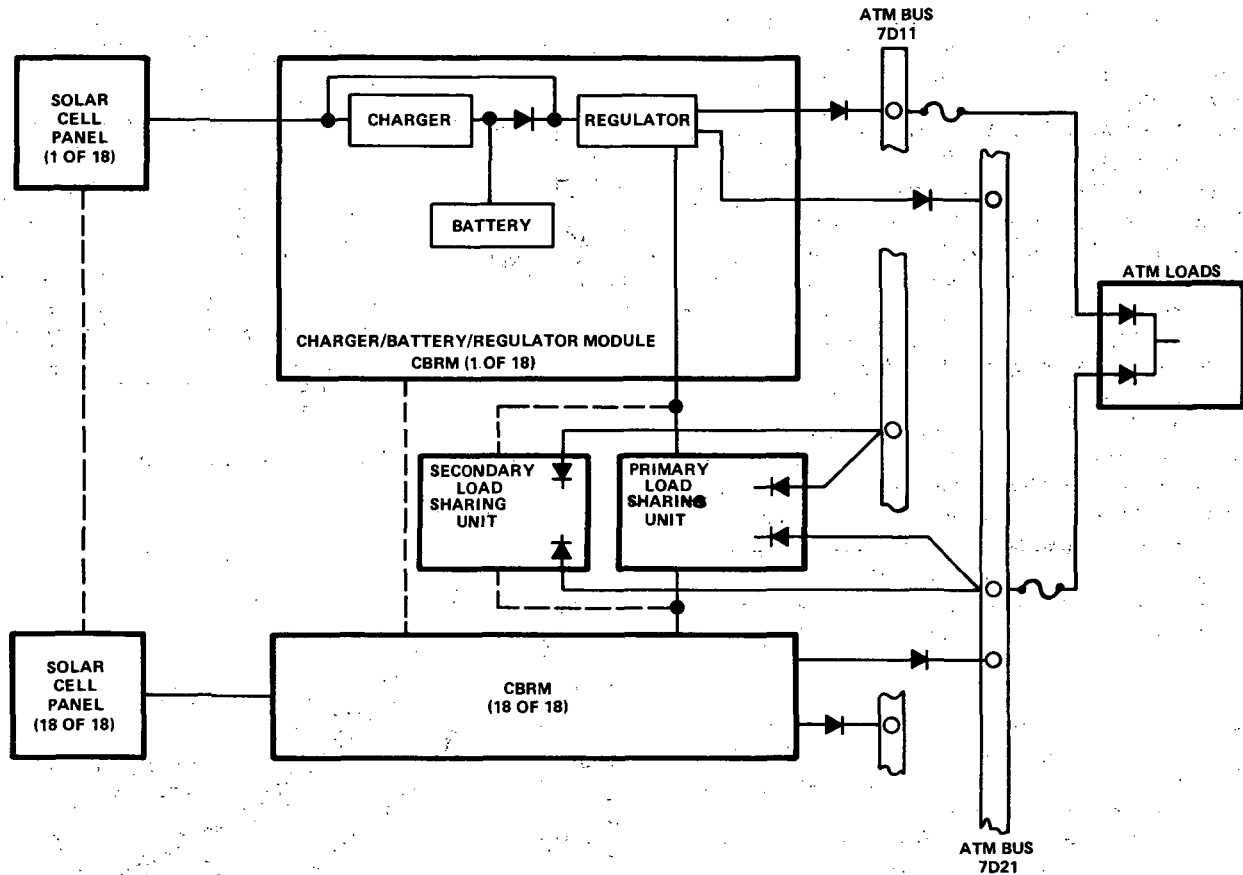


Figure 4. ATM electrical power system.

CHARGER, BATTERY, REGULATOR MODULE

Battery. The ATM battery has 24 General Electric AB-12, nickel-cadmium, 4-electrode, hermetically-sealed cells connected in series. In addition to the normal positive and negative power electrodes, the cells have a third electrode which is used in charge control and a passive fourth electrode which is an oxygen recombination electrode. The battery has a rated capacity of 20 A-h, but the actual capacity at a given time is a function of several variables. The more important of these are temperature, cycle life, and charge control method. The method of charge control is critical to both life and capacity retention, and over 4 years has been spent in testing the AB-12 cell and its predecessors. The charge method chosen is a constant-current charge at 15 A to a temperature-dependent voltage followed by tripback to a constant-voltage charge that is 0.85 V lower. The constant current is usually reduced in actual operation because of the solar

panel power limit. The termination of charge is a result of the third electrode cutoff that occurs when the third electrode voltage reaches 200 mV across a $200-\Omega$ load. The third electrode voltage is a function of oxygen partial pressure in the cell. Oxygen is released when the cell is fully charged and recombination of this oxygen results in the third electrode voltage. Battery charge is terminated rather than being reduced to a trickle charge mode. The ATM battery is totally passively cooled, and the heat associated with excessive overcharge cannot be allowed. Thermal control in the form of a proportional heater is provided to prevent the battery temperature from going below 0°C . The battery temperature operating range is 0°C to 30°C . However, operation at 30°C can cause significant capacity loss, and operation at 20°C or lower is desirable.

Charger. The CBRM charger is a buck-type switching circuit designed to provide proper charge control for the battery while achieving maximum

utilization of solar power. As may be seen in the CBRM block diagram, the solar panel feeds the charger and regulator in parallel. The regulator, which feeds the buses, has priority on the power. Excess power above that required by the regulator is used to charge the battery. The charger senses total solar panel current and reduces battery charging current to keep the solar panel current at less than 14.0 A. This current closely approximates the solar source peak power current over a wide temperature range. However, during the brief periods of penumbra in each orbit and during Z-LV operation, the solar panel peak power current varies widely and the solar panel voltage rather than current is sensed for charge control. The charger then reduces charging current if the solar panel voltage is less than 38 V. During these periods when the solar panel power is not sufficient to supply regulator requirements, the battery and solar panel share the power. In addition to solar panel current and voltage, the charger senses battery current, voltage, temperature, and third electrode voltage to provide proper charge control.

Regulator. The CBRM regulator has a buck-boost-type switching circuit that accepts power from the solar panel and/or battery and supplies regulated voltage to the ATM power buses. The regulator operates over an input range of 25.5 to 80 V. It has a peak output power capability of approximately 450 W. The output is current limited to prevent damage from overload or short circuit. The circuit provides bus load protection from overvoltage by sensing output voltages and turning the regulator off if the output voltage exceeds 31.8 V. Any failure in the regulator power circuit will result in no output voltage. This protects the buses from high battery and solar source voltages.

Analysis and subsequent tests have shown that, although the regulators were designed with a programmed impedance to provide inherent power sharing, voltage and impedance tolerances and line variations cause significant differences in regulator output power between the 18 regulators. The equivalent circuit shown in Figure 5 was used to derive the curves in Figure 6 which show the effect of these variations. This analysis reveals that, although reasonably tight tolerances are imposed on the regulator parameters, a power system degradation of up to 25 percent could exist. The degradation results from the fact that regulator power output is limited to approximately 232 W by solar source capability. In addition, 232 W during eclipse operation represents

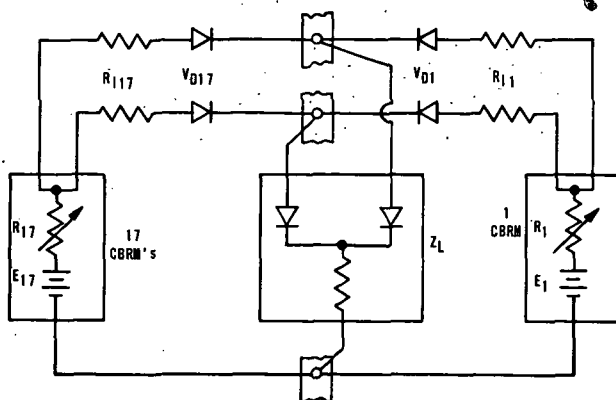


Figure 5. ATM EPS equivalent circuit.

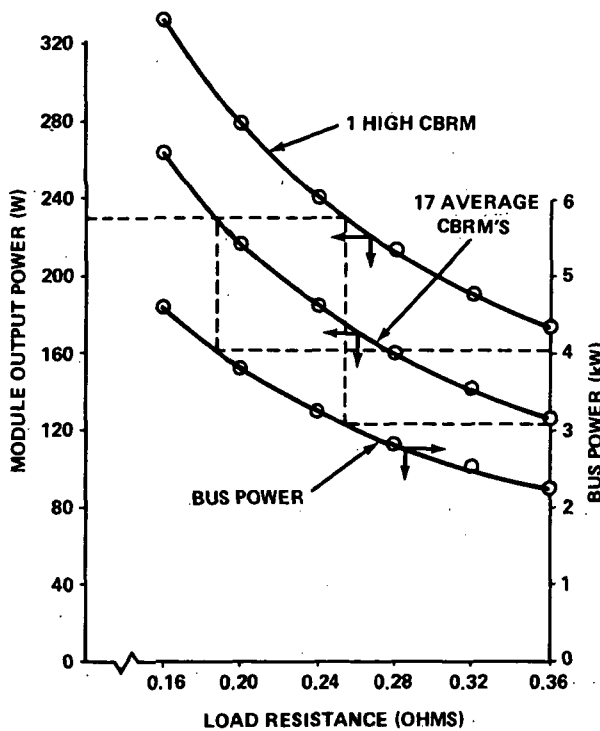


Figure 6. ATM EPS characteristics.

approximately 30 percent depth of discharge (DOD) for the battery. These factors impose a requirement for some means of sharing between regulators to achieve the maximum bus power capability. The power sharing scheme is discussed in another paper in this report.

Auxiliary Circuits.

Alert Circuits. Alert circuits are provided to give an astronaut notice of potential problems or changes of state of a component in the CBRM. The alert signals are displayed as black and white striped flags on the EPS control panel. In addition, a light indication is given in a central alert area on the ATM control and display panel.

Protection Circuits. Automatic protection is provided to turn off part or all of a CBRM in case of situations that could cause potential danger to the astronauts and/or damage to equipment.

Telemetry. Conditioning is provided as required for the telemetry signals. The telemetered parameters are used on the ground to monitor and control the ATM EPS during flight and for postflight scientific analysis.

Metering. In addition to signals telemetered for ground monitoring, several parameters are displayed on meters for the astronauts to monitor on the EPS panel. Switches are provided for selecting the CBRM for which monitoring is desired. The status of the charger, battery, and regulator of each CBRM is displayed on the bank of 54 lights in the upper right of the EPS control panel.

Controls. Control of the CBRM is exercised from the ground by a radio frequency (rf) command through the digital address system (DAS), or by an astronaut manually through the DAS keyboard or directly from the EPS control panel rotary and toggle switches. As a result of limited panel space, 1 charger on-off and 1 regulator on-off switch serve all 18 CBRM's. The CBRM being controlled is selected by a rotary and toggle switch combination. The battery is controlled by logic within the CBRM so that it comes on when the charger is turned on but goes off only if both the charger and the regulator are turned off. The CBRM ON switch simultaneously gives a charger-on and regulator-on command to all 18 CBRM's. In addition, there is an ATM POWER OFF switch in a central location on the ATM control and display panel that sequentially removes all loads from the ATM buses and then gives a charger-off and a regulator-off command to all 18 CBRM's. The status of any component in any CBRM may be ascertained by enabling the CBRM status lights. When the light is on, it indicates that the component is off.

Miscellaneous. In addition to the aforementioned auxiliary circuits, there is an auxiliary power

supply that generates bias and reference voltages for the other circuits and a battery heater controller that senses battery temperature and proportionally controls battery heater power to keep the battery temperature above 0°C.

SKYLAB EPS PERFORMANCE

Predicted Performance

The Skylab EPS is capable of supplying an average of approximately 7900 W at a beta angle of 0 deg to the ATM and AM primary buses at end of life with all modules working. This approximation is obtained from the energy balance equations for the two subsystems. The energy balance condition is defined as that condition for which the battery's charge is completed at the same time the illumination portion of the orbit is completed. The continuous average power capability of the ATM EPS is 3940 W at the end of mission life, and the continuous average power capability of the AM EPS is 3960 W at the end of mission life. This, of course, assumes no failures. Furthermore, analysis of battery DOD's under these conditions reveals that neither the ATM nor the AM batteries are discharged to depths greater than 30 percent. Failure of two CBRM's or one PCG would allow continued operation at the required load. However, load management provisions allow mission completion with as many as four CBRM's and two PCG's failed.

Z-LV Operation

Analysis of the Skylab available power when operating in the Z-LV modes is somewhat more difficult. Computer programs have been developed that take actual charger utilization of predicted solar source power, solar temperature, and other more accurate assumptions, and calculate actual power outputs and battery DOD for small time increments. These programs are also used to refine solar inertial power predictions. During Z-LV operation, the batteries are allowed to go to 50-percent DOD. During rendezvous Z-LV operation, the vehicle is oriented with the backs of the solar cell arrays pointed toward the earth's local vertical for the complete orbit. For earth resources experiments, Z-LV orientation is required only during performance of the experiments and the vehicle is returned to solar inertial orientation for the remainder of the orbit in order to obtain more solar cell array power. The Skylab EPS is

expected to be capable of providing the required power during both of the Z-LV modes of operation.

CONCLUSIONS

The Skylab EPS, as it nears completion, promises to meet or exceed most of the design requirements including those imposed long after the subsystems design was fixed. During solar inertial operation, which is the prime mode of operation, the system has a power output capability of almost 8000 W at the end of the mission. This is the capability at a beta angle of 0 deg, which is the worst dark-light condition. As the beta angle increases, power capability increases substantially in the solar inertial mode. During the Z-LV rendezvous mode of operation, the system has an output power capability greater than 4000 W, as a worst case, which is a substantial margin over the 2600-W requirement. Although the requirement for Z-LV earth resources experiments operation was imposed on the EPS late in the program, the system is expected to meet the requirement. The requirement for parallel operation of the two power subsystems, although imposed late in the program, has been demonstrated at the regulator level. These capabilities promise to provide the Skylab with a modular EPS with maximum flexibility, power utilization, and reliability. The capability of

a modular power subsystem to reliably supply power is depicted in Figure 7. Note that a very high probability of success can be obtained by having the capability for losing several modules. In the Skylab, by using power management, up to four CBRM's and two PCG's may be lost without losing the mission. This gives a high probability of mission success. In addition, data from the Skylab EPS, which will be more than any previously obtained, are expected to significantly advance knowledge of large space power system components and operation.

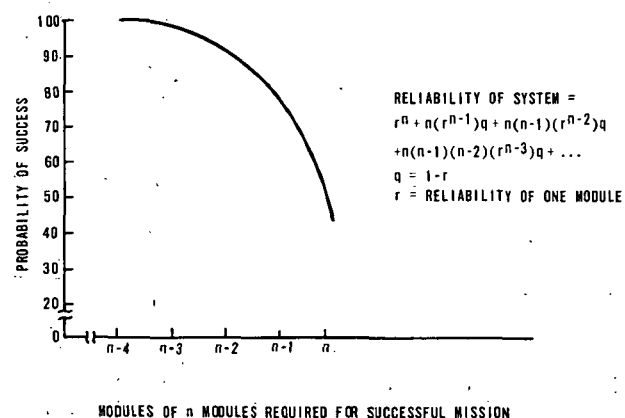


Figure 7. Modular power subsystem reliability.

Page intentionally left blank

ANALYSIS OF EFFECTS OF SHADOWED AND OPEN SOLAR CELLS ON OWS SOLAR CELL ARRAY PERFORMANCE

By

J. L. Miller

ABSTRACT

The effect of "hot spots" and "voltage breakdowns" caused by open or shadowed cells in the Orbital Workshop (OWS) solar cell array is analyzed in this paper. The analysis is performed on three proposed OWS solar cell string configurations of 1, 2, and 4 cells in parallel by 154 cells in series. Under several operating conditions, at least one cell string configuration showed an excessive "hot spot" temperature.

SUMMARY

This report describes the investigation and analysis of shadow-induced failure phenomena associated with silicon solar cell arrays. These phenomena, which can result from an open or shadowed cell, include interconnect failure and cell breakdown caused by excessive reverse voltage biasing.

Proposed Orbital Workshop solar cell module configurations are analyzed to determine the severity of "hot spots" and "voltage breakdowns" caused by open or shadowed cells. Before addressing specific configurations, a method for obtaining the V-I characteristics of solar cell matrices is developed for use in determining the magnitude of the reverse voltage impressed across an element in a series string when the operating point of the string is known. Tests and analyses are conducted to quantify and qualify the V-I characteristics of 2- by 4-cm solar cells as a function of reverse voltage bias, illumination, and temperature.

The derived models and empirical data are then combined to analyze three proposed OWS solar cell

string configurations of 1, 2, and 4 cells in parallel by 154 cells in series.

LIST OF SYMBOLS

<u>Symbol</u>	<u>Definition</u>
A _{MO}	Air mass zero
C. F.	Curve factor
I _M	Composite current of a parallel group of M cells
I _{MAX}	Current at maximum power
I _{SC}	Short-circuit current
P _R	Normalized power dissipated in a reverse biased submodule
T _{VOC}	Temperature coefficient of a cell's V _{OC}
T _{VM}	Temperature coefficient of a cell's V _{MAX}
V _{MAX}	Voltage at maximum power
V _N	Composite voltage of a series string of N cells
V _O	Operating voltage of the array
V _{OC}	Open-circuit voltage
V _{RB}	Reverse bias voltage
V _{RT}	Reverse threshold voltage
V _{SM}	Solar cell module voltage

INTRODUCTION

Large solar arrays are susceptible to "hot spots" in some sections of the array because of abnormalities in the cell string caused by shadowing or a cell failure. The steps necessary to analyze the "hot spot" phenomenon are discussed. In particular, the steps developed for analysis of one of the large arrays of the Skylab program are presented.

First, an analytical method of developing V-I curves for a string of series-parallel elements and isolating submodules containing shadowed or failed cells is described. Since the characteristics of the shadowed or failed cell are important, the tests used for obtaining the reverse characteristics of the cells used in the array are presented. The reverse characteristics, when combined with the temperature rise versus power curves obtained from a thermal analysis, provide the necessary reverse voltage V-I curves for the analysis. Finally, the reverse voltage curves are combined with the forward curve of the remainder of the module for the particular shadowed- or failed-cell configurations, and the reverse voltage and the "hot spot" temperatures are calculated.

The previous work of F. A. Blake and K. L. Hanson of General Electric on "The 'Hot Spot' Failure Mode for Solar Arrays" [1] was the basis for the initial stages of this effort.

ANALYTICAL METHOD

A general model for series-parallel combinations of solar cells is developed for use in determining solar cell matrix characteristics when one or more cells are shadowed. The shadowed cell (or cells) is isolated and the effect on the cell matrix is determined analytically. The general case is then used to predict the effects of shadows on the OWS solar cell array configuration being considered.

Solar Cell Module

A solar cell module, as used herein, is defined as one or more cell strings sharing common positive and negative electrical current bussing points. Each string is a series-connected group of one or more two-terminal submodules, with each submodule consisting of a parallel-connected group of one or

more two-terminal elements. A model of an $M \times N$ string consisting of N submodules of M cells each is shown in Figure 1.

Composite V-I Curve

Since the solar cell string consists of two-terminal electrical elements connected in a series-parallel matrix, the procedure for obtaining the composite V-I characteristic for such a string may be justified as follows.

ELEMENTS IN SERIES

The current through each element in a series string must be the same; therefore, if one element has a characteristic $V_1 = f_1(I)$, the remaining elements will have characteristics $V_2 = f_2(I), \dots, V_n = f_n(I)$, where $f_1(I), f_2(I), \dots, f_n(I)$ are single-valued functions as shown in Figure 2. The composite V-I characteristic for the series string can be obtained by adding the voltages across each element for each current value:

$$V_N = V_1 + V_2 + \dots + V_n = f_1(I) + \dots + f_n(I) . \quad (1)$$

In the event all n elements have identical characteristics, the expression simplifies to

$$V_N|_I = n(V_1|_I) .$$

ELEMENTS IN PARALLEL

The voltage across each element in a parallel group must be the same; therefore, if one element has a characteristic $I_1 = f_1(V)$, the remaining elements will have characteristics $I_2 = f_2(V), \dots, I_m = f_m(V)$, where $f_1(V), f_2(V), \dots, f_m(V)$ are single-valued functions as shown in Figure 3. The composite V-I characteristic for the parallel group can be obtained by adding the currents through each element for each voltage value:

$$I_M = I_1 + I_2 + \dots + I_m = f_1(V) + f_2(V) + \dots + f_m(V) . \quad (2)$$

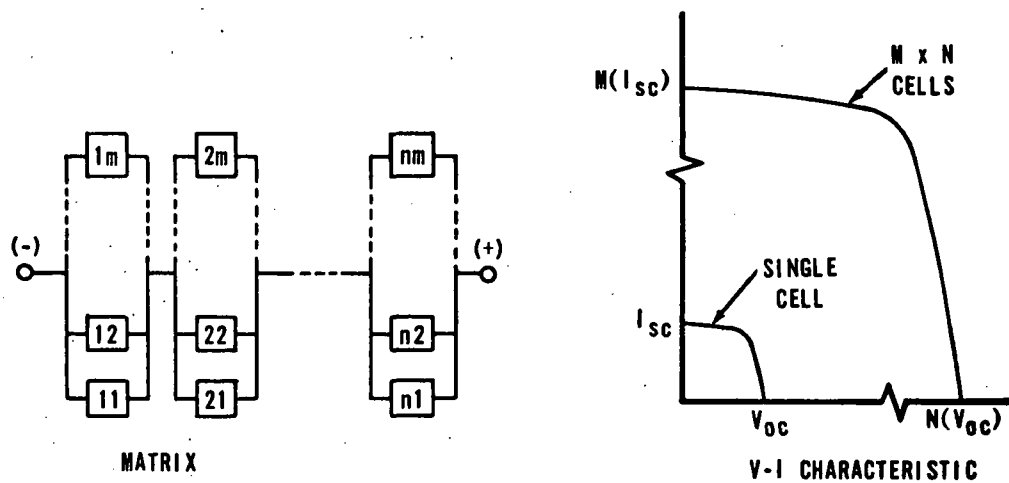
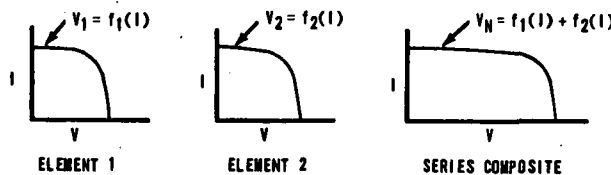
Figure 1. $M \times N$ string matrix and V-I characteristic.

Figure 2. Composite V-I characteristic for series string.

In the event all m elements have identical characteristics, the expression simplifies to

$$I_M \Big|_V = m \left(I_1 \Big|_V \right)$$

Cell Shadowing

The model of a cell string will now be examined to determine when a submodule, which has a shadowed element, becomes reverse-voltage-biased. If all elements in the $M \times N$ matrix are assumed to be identical¹, the V-I characteristic of a submodule will be the characteristic of a single element with the current scaled by M , and the V-I characteristic of the string will be the

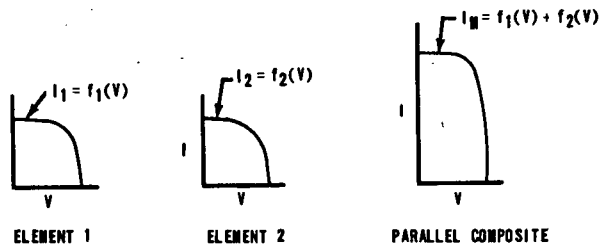


Figure 3. Composite V-I characteristic for parallel group.

characteristic of a submodule with the voltage scaled by N .

Assume that one cell is shadowed. An open cell's reverse characteristics are the same as a fully shadowed cell with zero leakage. Therefore, an open cell and a shadowed cell may be treated the same insofar as their effect on reverse bias is concerned. The string with the shadowed element may then be considered as a series combination of an $M \times (N-1)$ string matrix and an $(M-1) \times 1$ submodule. The V-I characteristic of the $M \times (N-1)$ matrix is the characteristic of a normal $M \times N$ string with the voltage scaled by $(N-1)/N$. The V-I characteristic of the $(M-1) \times 1$ submodule is the characteristic of a single cell with the current scaled by $(M-1)$. The V-I characteristic of the series combination of the $M \times (N-1)$ string and the $(M-1) \times 1$ submodule is shown in Figure 4.

1. If the elements are not identical, equation (2) must be used to establish the V-I characteristic for each submodule and equation (1) must be used for the series string of submodules.

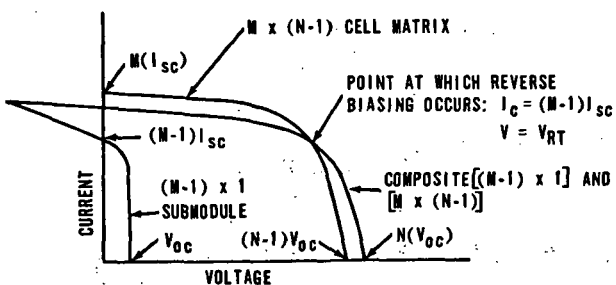


Figure 4. Composite V-I characteristic of an $[M \times (N-1)]$ cell matrix and an $[(M-1) \times 1]$ submodule in series.

Reverse voltage biasing of the $(M-1) \times 1$ submodule will occur whenever

$$I_c > \frac{(M-1)}{M} M(I_{SC})$$

or

$$I_c > (M-1)I_{SC}$$

where I_c is the composite current.

The reverse bias threshold voltage (V_{RT}) at which the $(M-1) \times 1$ submodule will be reverse-biased is the voltage on the $M \times (N-1)$ cell matrix curve corresponding to a current of $(M-1)I_{SC}$.

Since the series combination will be in parallel with several other strings, the submodule with the shadowed cell will be reverse-biased whenever the solar cell module voltage (V_{SM}) is below V_{RT} .

The reverse bias voltage (V_{RB}) will be equal to the actual solar cell module voltage less the reverse bias threshold voltage:

$$V_{RB} = V_{SM} - V_{RT} \text{ (for } V_{SM} \leq V_{RT})$$

The current at which the shadowed submodule will become reverse-biased will be closer to the

short-circuit current when the number of cells in parallel is large. The magnitude of the reverse bias voltage depends on the number of submodules in series, the shape of the V-I characteristics, and the terminal voltage at which the module is operated.

TEST METHOD FOR OBTAINING SINGLE CELL REVERSE BIAS DATA

Tests were performed to determine reverse bias V-I characteristics as a function of temperature for illuminated and dark OWS type 2- by 4-cm silicon solar cells. Steady-state reverse bias characteristics were then derived by combining the empirical data with the temperature versus power dissipation curve generated in the thermal analysis [2].

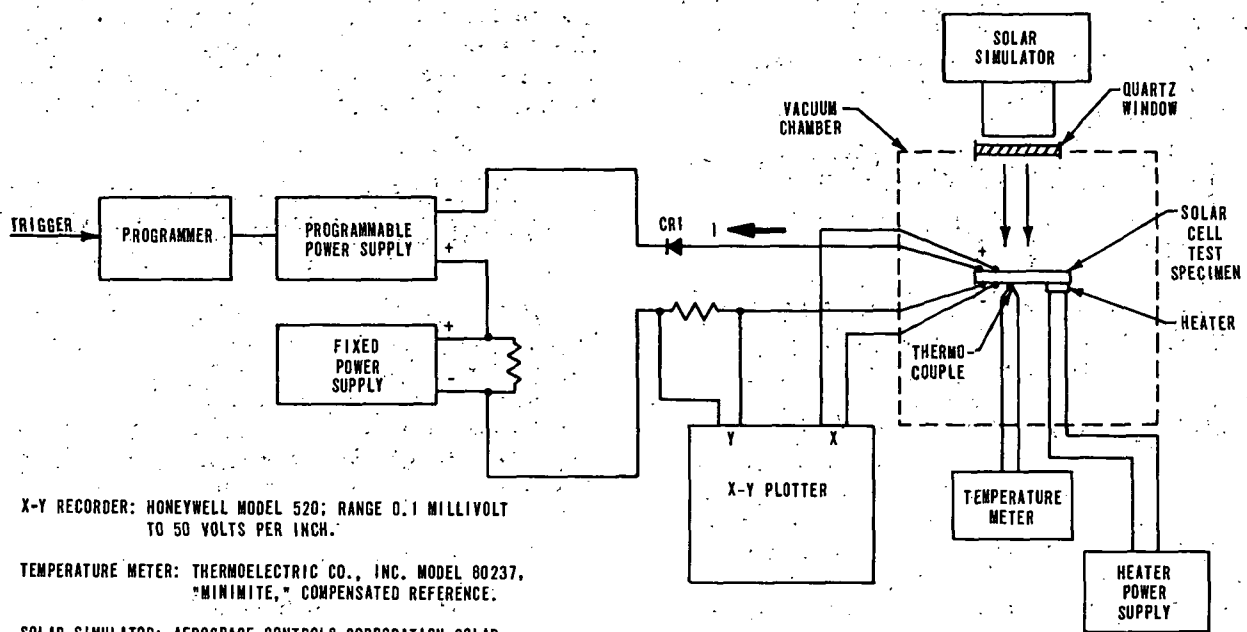
Test Sample and Setup

A total of 34 solar cells were tested in 5 test groups. Test group 1 contained 10 cells and test groups 2 through 5 contained 6 cells each. The solar cells were N on P, $2\Omega\text{-cm}$ base resistivity, 2- by 4-cm, 14-mil thick silicon devices obtained from Centralab.

Each solar cell was secured to an aluminum plate with General Electric RTV-118 silicon adhesive. The thermocouple for temperature monitoring was located directly beneath the solar cell, and a heater was mounted on the back of the aluminum plate. The plates were then secured through thermal insulators to a mounting fixture that was installed in the vacuum chamber. A schematic of the test setup is shown in Figure 5.

Test Operation

The output (approximately 2 V) of the fixed power supply is set slightly positive with respect to the cell open-circuit voltage to obtain the forward characteristic curve (Fig. 5). Diode CR1 prevents current in the negative direction through the test specimen. The programmer generates a voltage ramp with adjustable amplitude and slope



X-Y RECORDER: HONEYWELL MODEL 520; RANGE 0.1 MILLIVOLT TO 50 VOLTS PER INCH.

TEMPERATURE METER: THERMOELECTRIC CO., INC. MODEL 80237, "MINIMITE," COMPENSATED REFERENCE.

SOLAR SIMULATOR: AEROSPACE CONTROLS CORPORATION SOLAR RADIATION SIMULATOR MODEL TYPE 244, MOD. NO. 1.

VACUUM CHAMBER: MT. VERNON RESEARCH COMPANY UHV SPACE CHAMBER MODEL 732.

PROGRAMMABLE AND FIXED POWER SUPPLIES: KEPCO MODEL JQES55-2; 0 TO 55 VOLTS, 0 TO 2 AMPERES, PROGRAMMABLE.

HEATER POWER SUPPLY: SORENSEN OCR80-18A.

PROGRAMMER: MSFC; CAPABLE OF GENERATING A SINGLE RAMP WHEN TRIGGERED.

Figure 5. Test setup schematic for reverse characteristics test.

that returns to zero at the end of the sweep. This ramp causes the output of the programmable power supply to sweep linearly from 0 to -18 V (or higher if testing for breakdown). This negative voltage ramp plus the fixed positive voltage causes the voltage impressed across the cell to sweep from open circuit to approximately -16 V. The X-Y plotter, with the cell current at the Y input and the voltage at the X input, plots the reverse bias V-I characteristic of the test specimen.

Test Data

Prior to testing, the performance of all cells was measured using a Jet Propulsion Laboratory

secondary standard as the reference for calibration. During the illuminated test, the solar simulator's intensity was adjusted to obtain the short-circuit current for each cell equal to that calculated for an intensity of 140 mW/cm^2 . Reverse bias data were obtained with each cell stabilized at 50, 100, and 150°C , and 10 cells were also tested at 200°C . Each solar cell was stabilized at the test temperature and an illuminated characteristic curve was obtained; the light was then blocked and a dark curve was plotted. A high leakage cell and a low leakage cell were chosen from the first 10 cells tested to obtain reverse bias curves to 40 V. On 24 test specimens, the reverse breakdown voltage was measured at 100°C after completion of the reverse bias tests.

REVERSE BIAS TEST RESULTS AND INTEGRATION WITH THERMAL ANALYSIS DATA

Reverse bias V-I characteristics recorded during testing of cells 6-1, 9-1, and 10-1 are shown later in Figures 8, 9, and 10, respectively. The dark leakage data are summarized in Figure 6 to show sample distribution.

Reverse Bias Current Leakage

The reverse biased cell dark leakage currents shown in the distribution graphs of Figure 6 varied

from 1 mA to over 200 mA. As would be expected, an increase in temperature or in reverse bias voltage caused a corresponding increase in leakage currents, but there were also over two orders of magnitude variation between high and low leakage specimens subjected to the same voltage and temperature conditions. The illuminated leakage characteristics may be approximated by adding I_{SC} to the dark V-I curves.

To obtain typical high and low leakage steady-state curves, characteristics data from a high leakage cell (9-1) and a low leakage cell (6-1) were combined with the temperature versus power

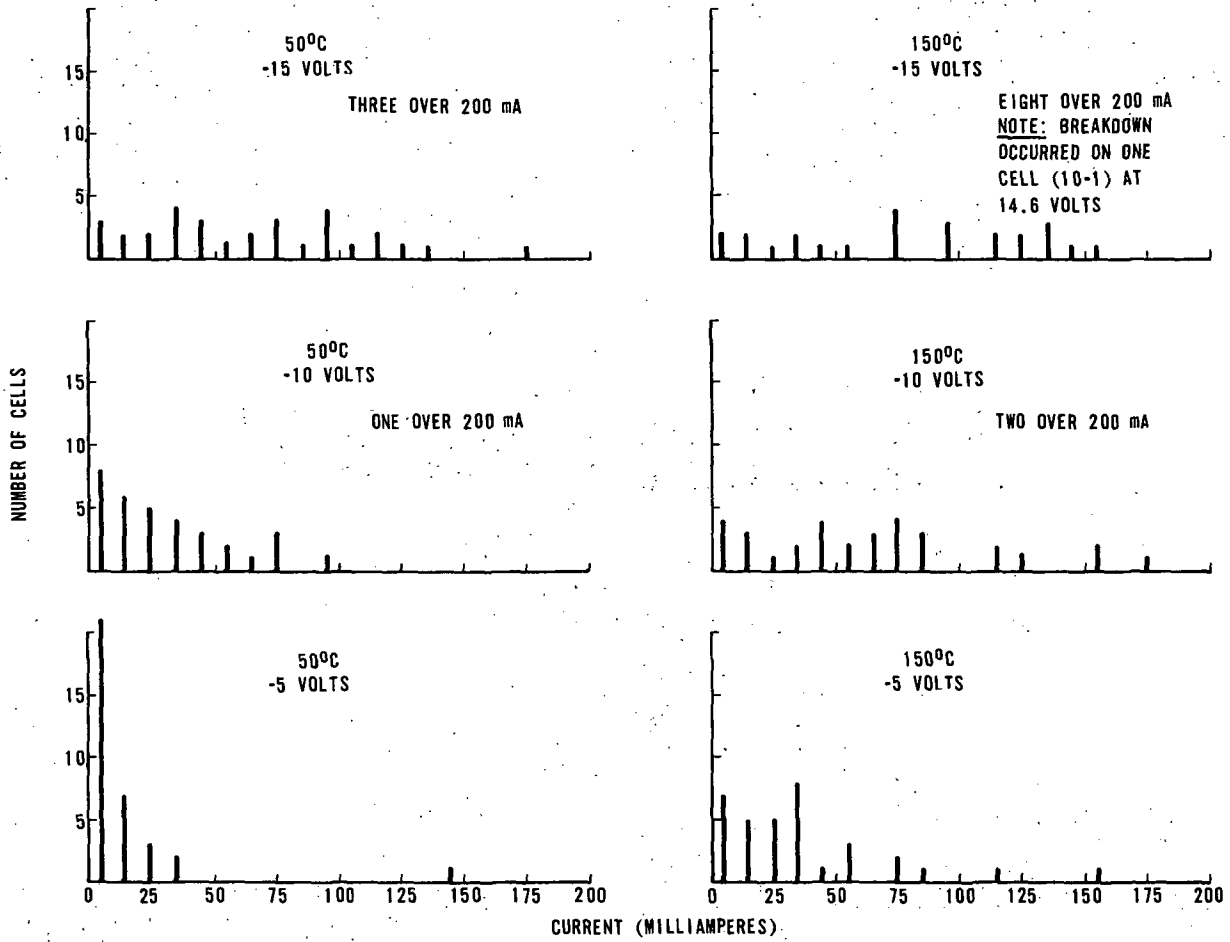


Figure 6. Dark leakage distribution for 34 cells at selected voltages.

dissipated data of Figure 7.² At each temperature on the reverse bias characteristics curves, a point is located such that the VI product (power) equals the power dissipated for the corresponding temperature in Figure 7. The loci of these points are the steady-state reverse curves for the high leakage (9-1) and low leakage (6-1) cells shown in Figures 8 and 9, respectively.

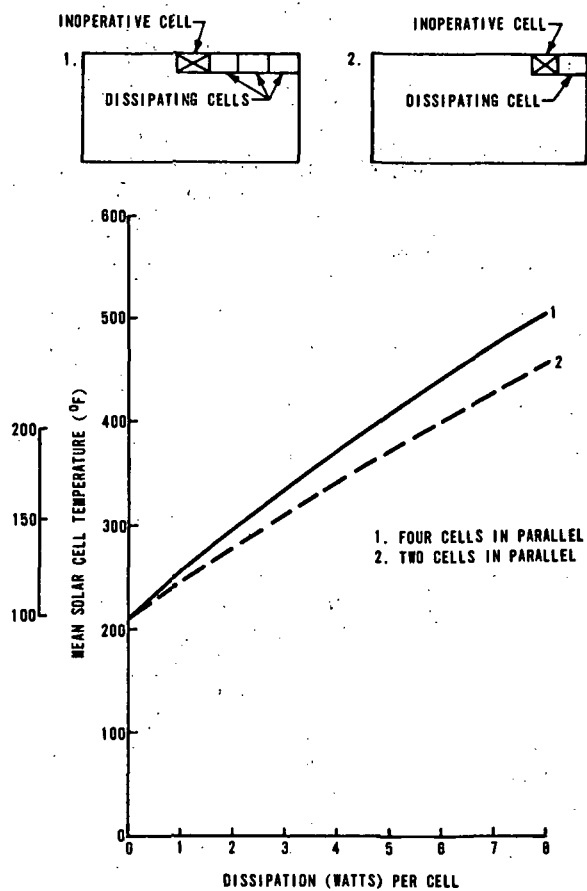


Figure 7. Temperature versus power dissipated curve from thermal analysis [2].

2. A thermal analysis of the OWS solar cell design was conducted to determine the temperature distribution of solar cells located near inoperative cells. A steady-state computer model was employed to determine the temperature of the cells. It was assumed that the cells were located on the hottest panel and that the panel was operating at the highest predicted temperature. Worst-case emissivities were used (0.76 active side, 0.79 passive side). Earth albedo, earth infrared, OWS blockage for view factor, and irradiation because of reflections between the solar panel and the OWS were considered in calculating the cell temperature for cell power dissipation of from 1 to 8 W. Further details are contained in Reference 2.

Reverse Bias Voltage Breakdown

Cell 4-1 (Fig. 10) is typical of the cells in which breakdown occurred. The current follows a normal leakage characteristic until breakdown occurs, which was at 22 V in this case. The cell then enters a negative resistance region where an increase in current causes a decrease in voltage.

This breakdown mode does not permanently affect the cell characteristics in all cases, since a second reverse breakdown test under identical conditions will produce essentially the same results. On some of the last 24 cells tested, however, the breakdown severely changed the forward and reverse characteristics, having an effect equivalent to that of a cell with extremely high reverse leakage. The breakdown mechanism is not clearly understood at this time.

The "voltage breakdown" phenomenon is a function of both temperature and illumination intensity as shown for cell 10-1 in Figure 11, where the dark breakdown voltage decreased from 14.6 to 10 V with a temperature change from 150 to 200°C. Also, at a constant temperature of 150°C, the breakdown voltage changed from 14.6 to 12 V when the illumination intensity was increased from 0 to 140 mW/cm².

ANALYSIS OF THE "HOT SPOT" PHENOMENON

To generate the forward V-I curves for OWS solar array analysis, the following available solar cell data were utilized: maximum power voltage (V_{MAX}) of 475 mV/cell; open-circuit voltage (V_{OC}) of 584 mV/cell at 29°C; and temperature coefficients (T_{VM} and T_{VOC}) of 2.06 mV/°C for V_{MAX} and 2.25 mV/°C for V_{OC} . These

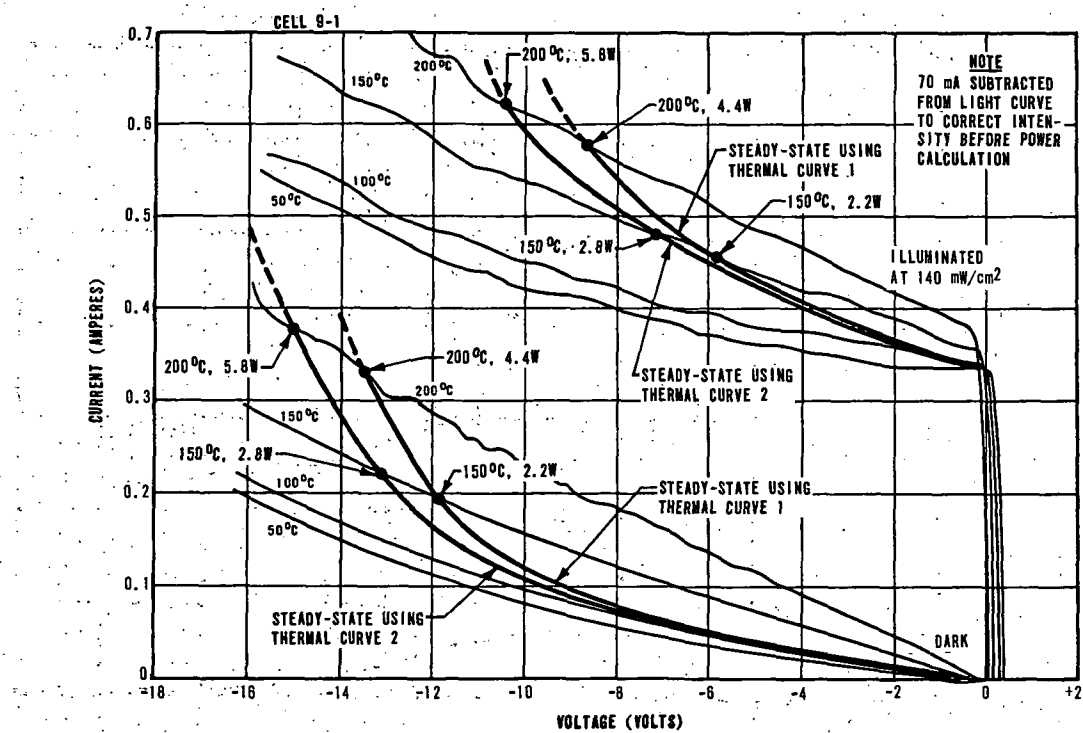


Figure 8. Steady-state reverse voltage curves for high leakage cell 9-1.

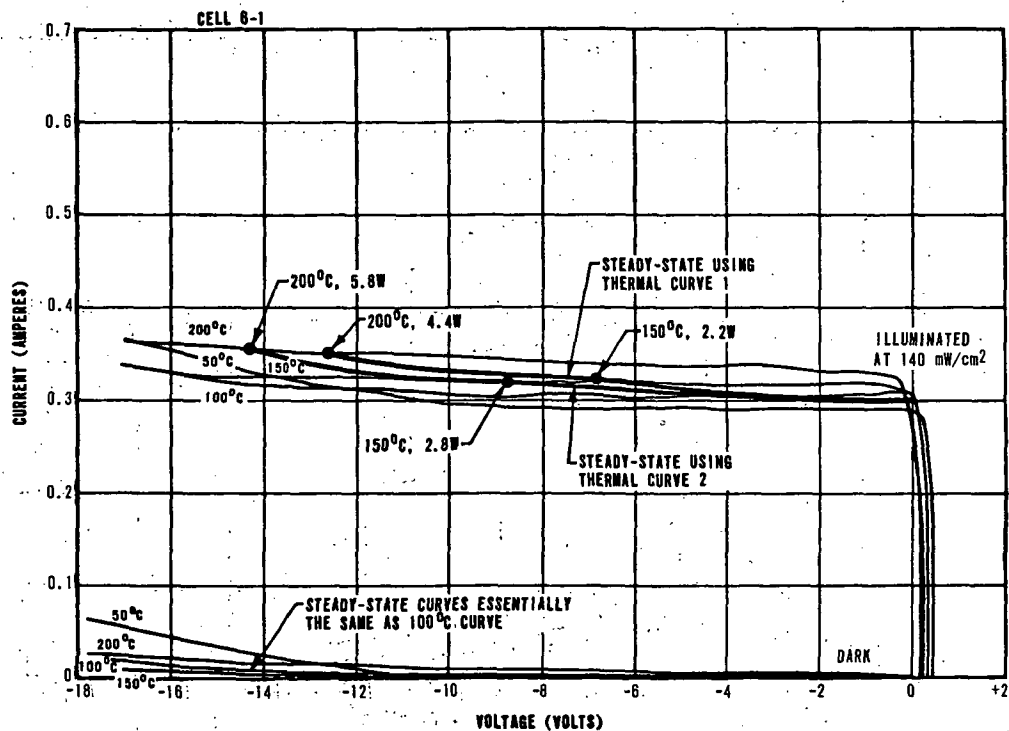


Figure 9. Steady-state reverse voltage curves for low leakage cell 6-1.

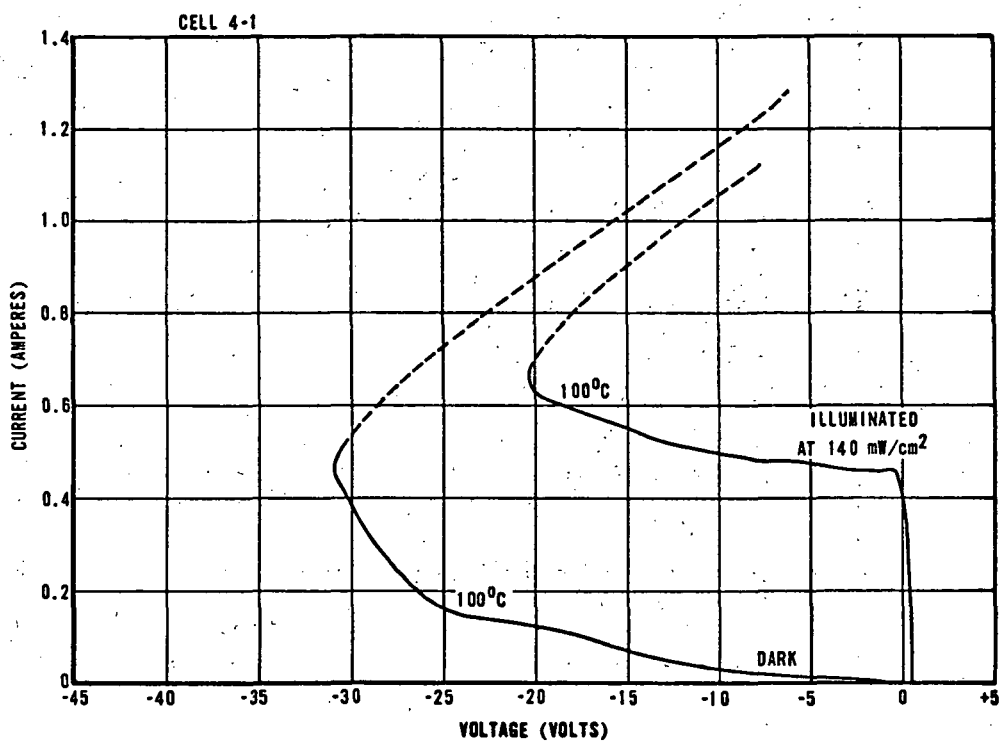


Figure 10. Voltage breakdown, dark and illuminated curves, cell 4-1.

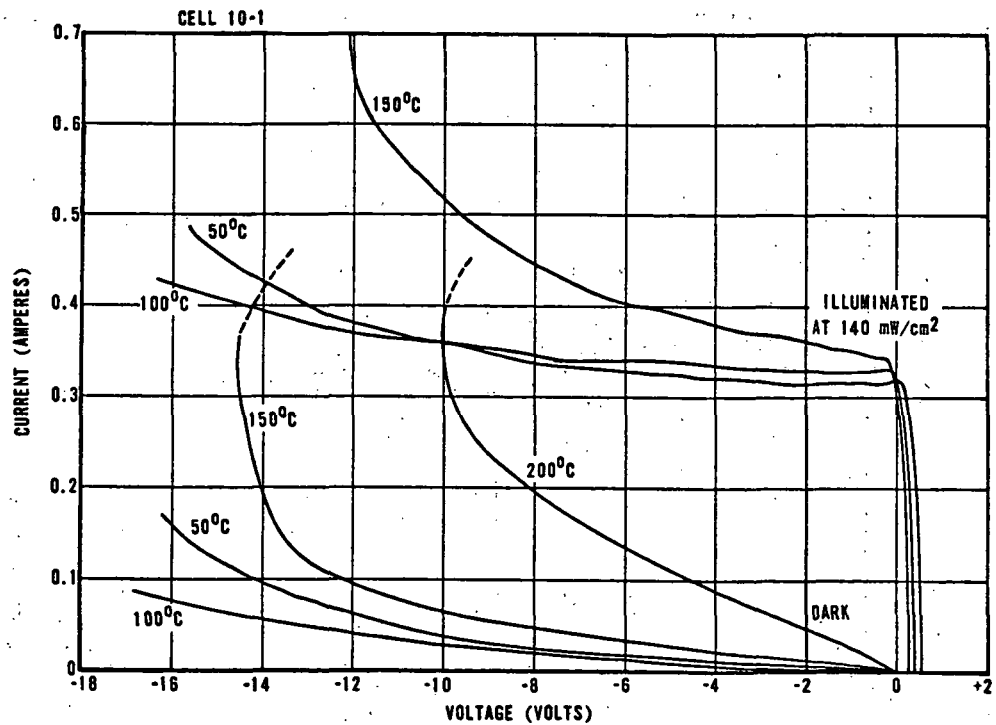


Figure 11. Dark and illuminated reverse characteristics of cell 10-1.

data give a value of V_{MAX}/V_{OC} as follows:

1. At 100°C,

$$\frac{V_{MAX}}{V_{OC}} = \frac{V_{MAX} \text{ at } 29^\circ\text{C} - 2.06 (100-29)}{V_{OC} \text{ at } 29^\circ\text{C} - 2.25 (100-29)} = 0.775.$$

2. At 29°C,

$$\frac{V_{MAX}}{V_{OC}} = \frac{475}{584} = 0.813$$

3. At -85°C,

$$\frac{V_{MAX}}{V_{OC}} = \frac{V_{MAX} \text{ at } 29^\circ\text{C} - 2.06 (-85-29)}{V_{OC} \text{ at } 29^\circ\text{C} - 2.25 (-85-29)} = 0.845.$$

The value of maximum power current/short-circuit current (I_{MAX}/I_{SC}) will be assumed for all temperatures for purposes of this report.

A computer program was used to calculate I_L , I_O , C_1 , and R_S in the normalized Cummerow equation [3],

$$\frac{I}{I_{SC}} = I_L^{-1} I_O \left[e^{C_1 \left(\frac{V}{V_{OC}} + R_S \frac{I}{I_{SC}} \right)} - 1 \right]$$

such that the V_{MAX}/V_{OC} and I_{MAX}/I_{SC} ratios of the curve described by the equation will be sufficiently close to the preceding desired values of 0.775, 0.813, and 0.845 for V_{MAX}/V_{OC} and 0.90 for I_{MAX}/I_{SC} . A program was used to plot the curves for these three cases. The first plot is shown in Figure 12; the curves for V_{MAX}/V_{OC} of 0.813 and 0.845, which are not shown, have a similar shape. The V_{OC} for these colder array temperatures is higher.

The program also plotted

$$10P_R(I) = \frac{(V - V_O) I}{V_{OC} \times I_{SC}} \times 10$$

where

P_R is the normalized power dissipated in the reverse biased submodule,

V is the $M \times (N-1)$ cell matrix voltage,

V_O is the operating voltage of the array,

I is the current at V ,

and

10 is used as a scale factor.

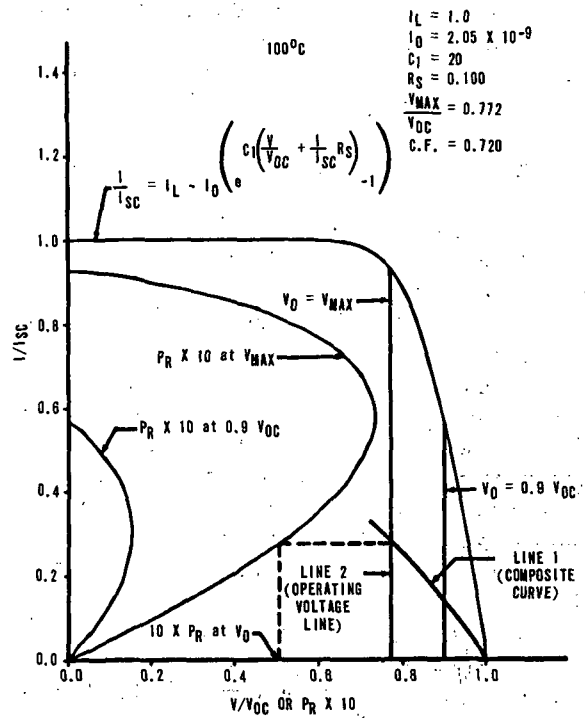


Figure 12. Normalized V-I and P_R curves at 100°C .

Two curves were plotted; one for $V_O = V_{MAX}$, and another for $V_O = 0.9 V_{OC}$ (Fig. 12). The usefulness of the P_R curve is in determining the amount of power that will be dissipated in the shadowed submodule. The normalized power dissipated in the shadowed submodule is read from the P_R curve at the current corresponding to where the composite curve (line 1, Fig. 12) crosses the operating voltage line (line 2, Fig. 12). At this point, $V - V_O$ equals the reverse bias voltage, and I is the corresponding current. The curves, or portions of the curves, of Figure 12 are used in the analysis of the proposed cell string configurations discussed in later paragraphs.

The fact that shadows have a penumbra, and that part of a cell may be shadowed, can be taken into account by considering each cell to be illuminated with a constant intensity equal to the integral of the actual intensity over the cell divided by the cell area. A cell was tested to check the validity of this assumption.

The strings considered in the analysis were assumed to operate at or above their maximum power voltage. Since a string may be in parallel with others to make a module, the operating point will actually be at the maximum power point of the module. If there is no temperature gradient across the module, the maximum power voltage of the module and each string will be equal. If a temperature gradient exists, the maximum power voltage of the module and some of its strings may not be equal. For example, if all strings are hotter than the one being considered, the cold string will operate lower than its maximum power voltage when the module is at its maximum power point.

In the following analysis of the 1, 2, and 4×154 strings, it should be noted that if one-half of a cell in a 1×154 string is shadowed, that cell dissipates less power than a cell in a 2×154 string when the cell in parallel with it is shadowed. If two cells in a 4×154 string are shadowed, the power dissipated per cell in the remaining two cells is approximately the same as in the 2×154 case; however, the temperature will be higher because adjacent cells are dissipating equal power.

Analysis of 1×154 String

OPEN CELL CASE

For single cell strings, an open cell constitutes failure of the entire string.

SHADOWING

There are many different shadow conditions that must be considered. Some of the worst-case shadows will be discussed here. If a single cell is shadowed, or partially shadowed, the curve of the unaffected portion of the string will be that of a $1 \times (154 - 1)$ matrix, and the cell curve will be that of a cell partially or totally shadowed. If "K" cells are shadowed, the normal string will be a $1 \times (154 - K)$ matrix. Each of the "K" cells will have a V-I curve with the I_{SC} for that cell being proportional to the integral of the light intensity over the cell. The abnormal portion will be the series combination of these "K" cells. The current in each cell is the current at which the composite curve crosses the operating voltage line. Each cell operates at a voltage corresponding to this current on its V-I curve.

The case where a single cell is totally or partially shadowed is now considered. Figure 13 shows portions of Figure 12 with single cell curves superimposed. Line 1 of Figure 13 shows the composite curve of a totally shadowed low leakage cell (6-1). In this case, the maximum reverse voltage (14 V) occurs at low current, and low power is developed. Maximum power is dissipated in the cell whenever the composite curves cross the lowest operating voltage (V_{MAX}) line at point 1.

This power is 1.31 W/cell, corresponding to a temperature of $\approx 127^\circ C$ (Fig. 7). This condition can be reached by considering a dark high leakage cell (9-1, Fig. 8) as shown by line 2, or a low leakage cell with an average intensity of 0.575 AMO as shown by line 3. This shows that any cell, given the proper amount of illumination, can reach the worst-case condition.

The following results for the same shadowing condition at $29^\circ C$ and $85^\circ C$ were similarly obtained from the curves for V_{MAX}/V_{OC} of 0.813 and 0.845.

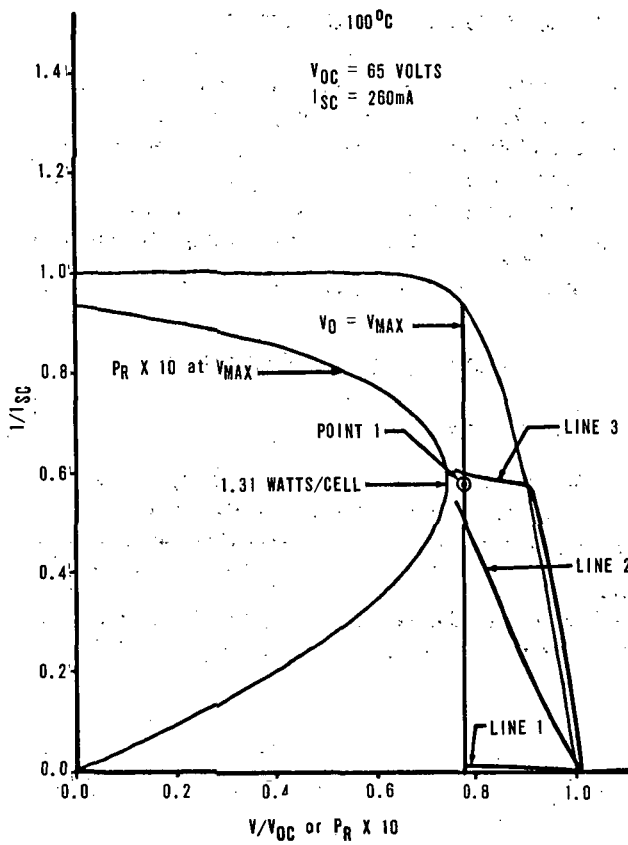


Figure 13. Normalized shadowing, 1×154 string, at 100°C .

At 29°C , the maximum reverse voltage is 16.7 V and the maximum power is 1.7 W/cell. At -85°C , the maximum reverse voltage is 20.1 V and the maximum power is 2.38 W. At 29°C , the maximum temperature rise is 36°C for a final temperature of 65°C . At -85°C , the temperature rise is 61.2°C for a final temperature of -23.9°C . Having one cell shadowed in a single-cell string is worse than having more than one cell shadowed, as far as reverse voltage and power dissipation are concerned, since the reverse bias voltage is concentrated across that one cell rather than being distributed across a number of shadowed cells.

CONCLUSIONS FOR 1×154 STRING

The power that can be dissipated by a single cell under the worst partially shadowed condition cannot raise the cell temperature higher than $\approx 127^\circ\text{C}$ if the string is not allowed to operate

below the peak power voltage. In arriving at a temperature of 127°C , it is assumed that the adjacent cell is in another string and is also shadowed. Operating the array below the peak power will cause the amount of reverse bias across the partially shadowed cell to be increased. The increase of the reverse bias will result in more power being dissipated, and thus a higher cell temperature will be reached. The increase in reverse voltage can cause a breakdown that would not occur if the voltage were kept above the maximum power voltage.

Since no cell can be reverse-biased over 20.1 V under the condition that the string operates at the peak power voltage or above, breakdown will not occur if no cell breaks down below 20.1 V. Screening the cells to 25 V would thus prevent breakdown.

The effect of a "hot spot" temperature of 127°C on the panel performance and reliability must be investigated. The analysis of the 1×154 string does not consider the effect of the temperature gradient across the panel, or the hazard of meteoroid damage or solder joint and/or interconnect fatigue.

Analysis of 2×154 String

OPEN CELL CASE

When one cell in the 2×154 matrix opens, the remaining cell will have a V-I curve that crosses the 2×153 cell curve at one-half the I_{SC} of the 2×154 cell curve. A low leakage cell will cross the V_{MAX} line below the maximum power dissipation point (point 1) of Figure 14. A high leakage cell will also cross the 2×153 curve at one-half of the I_{SC} of the module, but will have a higher slope as shown by line 1 (Fig. 14) and will thereby cross the V_{MAX} line above point 1. The maximum power that can be dissipated in a reverse biased submodule will be generated by a cell with a moderate leakage such that its superimposed curve (line 3) passes through point 1. The power dissipated (P_1) in this cell will be 2.62 W. From the P_R curve it is seen that both a low leakage cell, line 2, and a high leakage cell, line 1, dissipate almost as much power (P_2 and P_3)

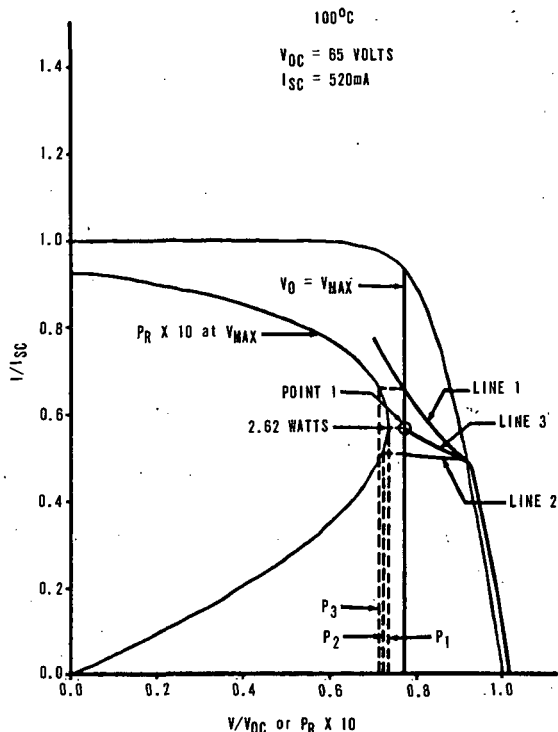
CONCLUSIONS FOR 2×154 STRING

Figure 14. Normalized open cell and shadowing, 2×154 string, at 100°C .

as the worst-case cell, line 3. Since this is an isolated open cell, thermal analysis curve 2 of Figure 7 will be used giving a cell temperature of $\approx 146^\circ\text{C}$. The final temperature, at an array temperature of 29°C and -85°C , can be obtained likewise, but the temperature would be lower than 146°C .

SHADOWING

Of all the possible shadows, the worst case would be a shadowed single cell in the 2×154 string. This would give an analysis similar to the open-cell case except that possibly a cell of another 2×154 string, near the shadowed cell, might also be shadowed. Then, a curve somewhere between thermal analysis curves 1 and 2 of Figure 7 should be used to find the temperature and would result in a temperature between $\approx 146^\circ\text{C}$ and 157°C .

For the open-cell condition, the temperature can go as high as 146°C using thermal analysis curve 2 of Figure 7. The worst shadow condition will give a temperature of $\approx 157^\circ\text{C}$. This analysis also assumes that the array will not operate at below V_{MAX} and that there are negligible temperature gradients across a given solar panel.

Analysis of 4×154 String

OPEN-CELL CASE

When one cell in the 4×154 string opens, the remaining three cells will have a V-I curve that crosses the $M(N-1)$ line at three-fourths of the I_{SC} of the 4×154 string. If all cells are high leakage cells, the curve will be line 2 of Figure 15, which is Figure 12 with curves added. If all the

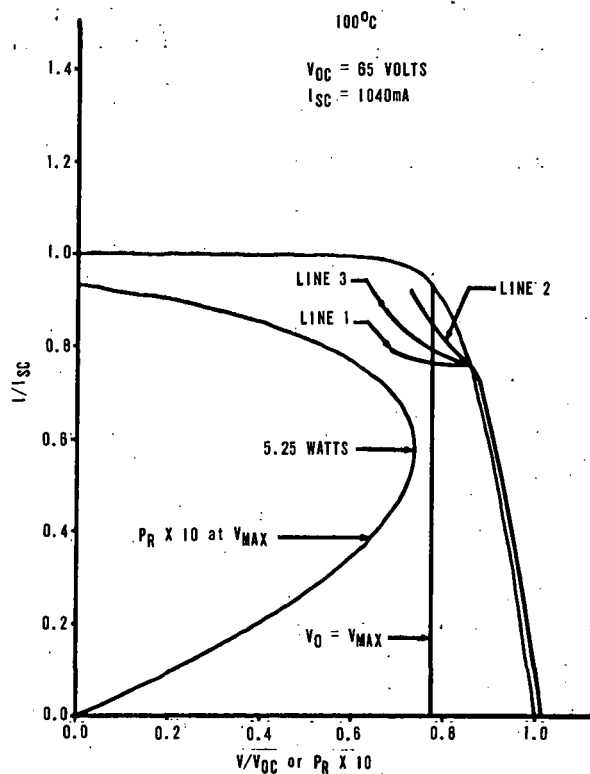


Figure 15. Normalized open cell, 4×154 string, at 100°C .

cells are low leakage, line 1 of Figure 15 will apply. Line 3 applies for one high leakage cell and two low leakage cells in parallel. The low leakage cells of line 1 dissipate 1.37 W each; the three high leakage cells of line 2 dissipate 0.95 W each; and the two low leakage cells and the high leakage cell of line 3 dissipate 1.17, 1.17, and 1.56 W, respectively. Even though the power and temperature rise higher, the final cell temperature for the 29°C and -85°C cases is lower and will not be shown.

The maximum temperature corresponding to 1.56 W/cell from thermal analysis curve 1 of Figure 7 is 132°C. Again, even though the power and temperature rise higher, the final cell temperature for the 29°C and -85°C cases are lower than 132°C and will not be shown.

SHADOWING

The case where one, two, or three cells are shadowed at 100°C is shown in Figure 16. In this figure, line 1 is the composite curve for one cell shadowed, line 2 is for two cells shadowed, and line 3 is for three cells shadowed. The leakage on the unshadowed cells is assumed to be the worst case as far as the power dissipated is concerned; i.e., the value needed to cause the composite to cross at a current nearest that corresponding to point 1. The power is distributed over the remaining cells. In the case where only one cell is left, the power dissipated in the cell is very high; approximately 4.55 W at 100°C, 6.8 W at 29°C, and 9.52 W at -85°C. At 100°C, 4.55 W correspond to a temperature of $\approx 182^\circ\text{C}$. In the 29°C and -85°C case, the final temperature is lower. Because of the large amount of power to be dissipated in the event that three out of four cells are shadowed, the 4×154 string is not recommended.

CONCLUSIONS FOR 4×154 STRING

In the open cell case, the 4×154 string reaches a lower temperature than the 2×154 string (132°C to 146°C) since only one of four cells is open instead of one of two. However, some shadowing conditions (e.g., three of four cells shadowed) can cause a temperature as high as 182°C.

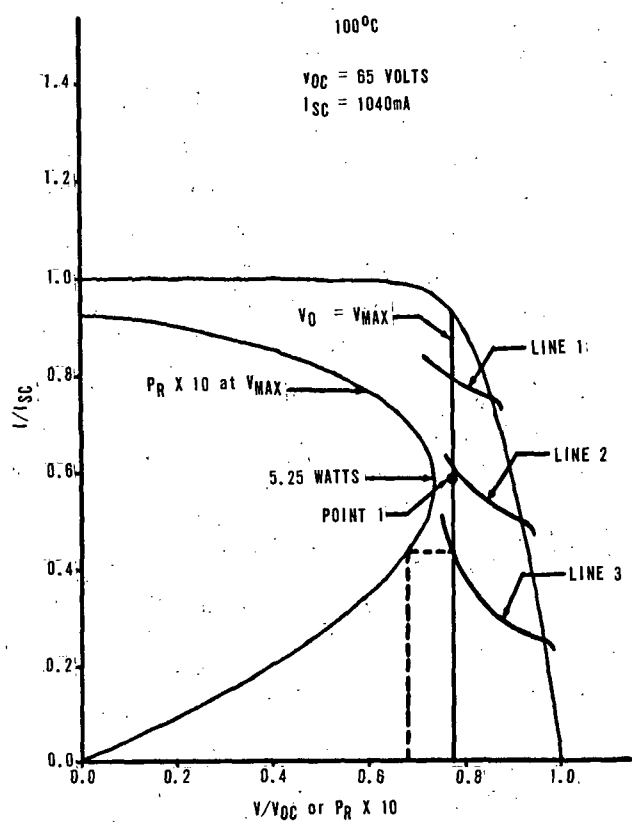


Figure 16. Normalized shadowing, 4×154 string, at 100°C.

CONCLUSIONS AND RECOMMENDATIONS

The three major conditions analyzed in this report are the effect of an open cell, the effect of shadows, and the possible occurrence of breakdown.

For an open cell failure, an open cell in the 1×154 string results in the loss of all 154 cells; in the 2×154 string, the hot cell can reach 146°C and the string operates at approximately one-half of the power at the V_{MAX} of the array. An open cell in another submodule of the 2×154 string would not substantially reduce its power generating

capability. In the 4×154 string, an open cell can cause a "hot spot" temperature of 132°C and a loss of as much as one-fourth of the power of the string at V_{MAX} of the array. As for the 2×154 string, the 4×154 string will not lose much more power if another cell opens in another submodule.

Considering the worst possible shadowing condition, the 1×154 string may reach a temperature of approximately 127°C . The 2×154 string will reach a temperature of approximately 157°C under its worst shadow; the 4×154 string will reach a temperature of approximately 182°C , which is above the solder melting temperature. Also, in the 4×154 string the power dissipated in the unshadowed cell is excessive at lower temperature (three of four cells shadowed).

The strings considered in the analysis will be free from breakdown if the cells are screened to have a breakdown voltage greater than 20.1 V. A reasonable voltage would be 25 V.

These conclusions are based on the latest thermal analysis and OWS solar cell and solar panel data. The analysis also assumes that the array operates at its maximum power voltage or above, and that the thermal gradient is such that each string operates at its maximum power voltage or higher.

If operation under all possible shadowing conditions is desired, it is recommended that the 1×154 string be used. This string results in a lower "hot spot" temperature under the worst conditions than the other strings studied. If open cell failures were the only consideration and no shadows could occur, the 4×154 string would be recommended since there is a reasonable temperature rise and a failure in any other submodule of the 4×154 string would not reduce power significantly.

The reduction of reliability because of open cells caused by meteoroids, solder interconnect failures, or other causes was not considered in this analysis. In addition, the obvious solution of paralleling several submodules in series, with diodes to limit reverse bias, was not addressed in this analysis.

FUTURE EFFORTS

The Skylab contains another large array for the Apollo Telescope Mount (ATM) for which a similar study on "hot spots" and "voltage breakdowns" will be performed. The ATM array uses 2- by 2-cm and 2- by 6-cm cells, arranged in 6×114 and 2×114 cell strings, respectively.

REFERENCES

1. Blake, F. A.; and Hanson, K. L.: The "Hot Spot" Failure Mode for Solar Arrays. Report No. 699070, General Electric Space Systems Organization, Valley Forge Space Center, Philadelphia, Pennsylvania.
2. Paul, H. G.: Orbital Workshop Solar Cell Hot Spot Phenomena Thermal Analysis. Technical letter S&E-ASTN-PL-70-M-252, Propulsion and Thermodynamics Division, George C. Marshall Space Flight Center, Huntsville, Alabama.
3. Sutton, G. W.: Direct Energy Conversion. McGraw-Hill Book Co., Inc., New York, N. Y., 1966, p. 14.

Page Intentionally Left Blank

THE USE OF THE SOLAR CELL DARK CHARACTERISTIC FOR CHECKOUT OF LARGE AREA SOLAR ARRAYS

By

W. L. Crabtree

INTRODUCTION

The silicon solar cell "dark characteristic" is the forward diode characteristic of the cell in the absence of illumination. It is obtained by applying voltage to the cell in the forward diode direction.

The dark characteristic and its similarity to the cell's illuminated characteristic have been known for almost as long as the cell has been in existence. However, little use has been made of this characteristic in the checkout of assembled solar arrays.

Solar arrays have generally been of relatively small size and thus were deployed easily in a 1-g environment. For this reason, checkout usually has been accomplished by deploying the array and illuminating its active surface with a light. However, with the present trend toward much larger solar arrays, the deployment of a large array designed for operation in a zero-g environment becomes difficult and expensive in a 1-g environment. The problems of deployment and electrical checkout of large area arrays are evident in the 10.5-kW Skylab cluster currently being assembled. The problems inherent to the deployment and electrical checkout of arrays as large as 100 kW, as proposed for the 1978 Space Station, become even more apparent.

The Apollo Telescope Mount (ATM) array of the Skylab cluster illustrates the problem. Prohibitive costs necessitated the deletion of a deployment capability at Kennedy Space Center; thus, a primary mode of checkout was required that did not necessitate deployment. The dark characteristic method of checkout was chosen. This paper describes the checkout method, presents a portion of the feasibility tests conducted, and defines the utilization in the ATM program.

The ATM solar array is composed of four wings arranged in a cruciform as shown in Figure 1. Each wing is approximately 17.24 m long (50 ft) and contains 4 panels and a half-panel with each panel consisting of 20 modules electrically in parallel. Each of the panels is electrically isolated from the others and supplies raw power to one power-conditioning module. The 4 inboard panels have only 10 modules each and therefore are connected in pairs to provide the required power.

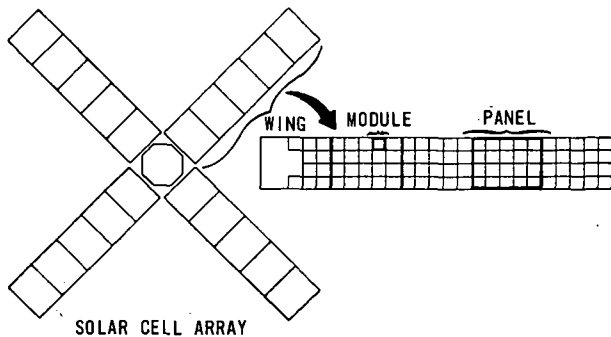
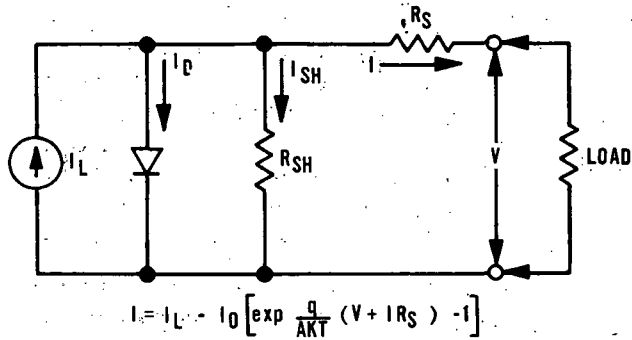


Figure 1. ATM solar cell array.

DARK CHARACTERISTIC AND PHOTOVOLTAIC CHARACTERISTIC OF SILICON SOLAR CELLS

To understand the dark characteristic method of testing, it is necessary to first examine the equivalent circuit of the silicon solar cell. Figure 2 shows the simplified lumped parameter model of the silicon solar cell that has customarily been used in solar cell work involving near-earth applications. It consists of a constant current generator under a fixed illumination, a junction diode, a series resistance, and a shunt resistance.



WHERE: I_L = LIGHT GENERATED CURRENT

I_{L0} = DARK OR SATURATION CURRENT

q = ELECTRON CHARGE, 1.602×10^{-19} COULOMBS

A = CURVE FITTING CONSTANT, DIMENSIONLESS

K = BOLTZMAN CONSTANT, 1.38×10^{-23} JOULES/K

T = ABSOLUTE TEMPERATURE

R_S = LUMPED SERIES RESISTANCE

R_{SH} = LUMPED SHUNT RESISTANCE

V = TERMINAL VOLTAGE

Figure 2. Solar cell equivalent circuit.

The shunt resistance is normally extremely large and has little effect upon the shape of the characteristic curve. Therefore, it may be ignored for purposes of this report.

Figure 3 shows a comparison of the equivalent circuit of a solar cell under both the illuminated and nonilluminated conditions. In the equivalent circuit for the illuminated condition, light is impinging upon the cell and a resistive load is varied in order to plot the illuminated or photo-voltaic characteristic of the cell. This circuit differs from the one shown in Figure 2 in that I_L

is replaced with I_{SC} since the two are approximately equal at one-sun intensity and normal operating temperatures.

The circuit of Figure 3 for the nonilluminated condition differs from the illuminated circuit in that $I_{SC} = 0$ and the load is replaced by a dc power supply that is capable of supplying a varying voltage to the cell in the forward diode direction. When the loop equations for the two circuits in Figure 3 are solved simultaneously to determine the difference between the illuminated and nonilluminated situations,

the result is:

$$\Delta V = R_S (I_D + I_L) \quad (1)$$

However, in the absence of illumination, the same current flows through both the diode and the series resistance. This is expressed by

$$I_D = I_{J2} \quad (2)$$

Also, by Kirchoff's law one has

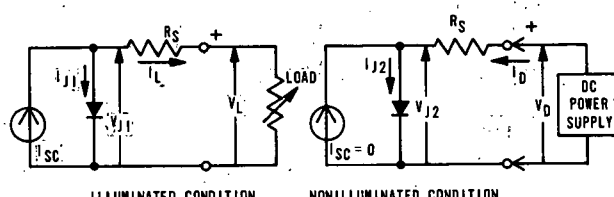
$$I_L = I_{SC} - I_{J1} \quad (3)$$

By expressing the equal diode voltage drops as

$$V_{J1} = V_{J2} \quad (4)$$

for the illuminated and nonilluminated conditions, it may be concluded that

$$I_{J1} = I_{J2} \quad (5)$$



LOOP EQUATIONS: $V_L - V_{J1} + I_L R_S = 0$ (ILLUMINATED)

$V_D - V_{J2} - I_D R_S = 0$ (NONILLUMINATED)

THEREFORE: $\Delta V = V_D - V_L = R_S (I_D + I_L)$

SINCE $I_D = I_{J2}$

$I_L = I_{SC} - I_{J1}$

$V_{J1} = V_{J2}$

$I_{J1} = I_{J2}$

RESULT: $\Delta V = I_{SC} R_S$

Figure 3. Comparison of equivalent circuits for a solar cell under illuminated and nonilluminated conditions.

Therefore,

$$\Delta V = I_{SC} R_S \quad (6)$$

which states that the difference between voltages at each current level for the illuminated and non-illuminated conditions is equal to the product of the short circuit current and the series resistance. The solar cell characteristic curves obtained by the illuminated and nonilluminated methods are shown in Figures 4 (a) and (b). The comparison of the dark and photovoltaic curve is shown in Figure 4 (c).

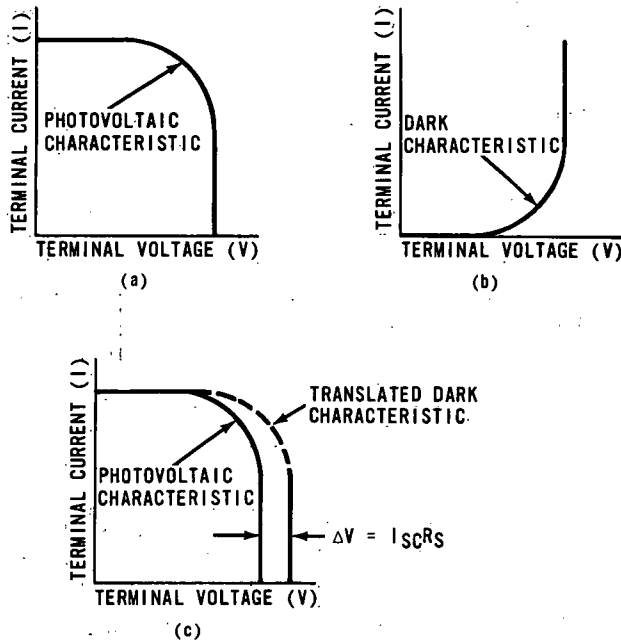


Figure 4. Comparison of photovoltaic and dark forward characteristics.

FEASIBILITY TESTS

Overheating Considerations

One of the concerns in performing the dark characteristic test was the possibility of damage that might result because of overheating caused by

injecting current into the array. Therefore, tests were performed to determine if this was a problem. Figure 5 shows temperature versus time curves for three applied currents for one ATM solar cell module. For a current of 2 A through one module, the temperature increased 20°C in 10 min. A 2-A current is about two and one-half times the Air Mass Zero (AMO) I_{SC} and will not be encountered under normal operating conditions. An extremely high current of 16 A was applied to the module, and in this case the temperature increased about 25°C in 30 s. This is the condition that will exist if the total panel AMO I_{SC} is flowing through one module.

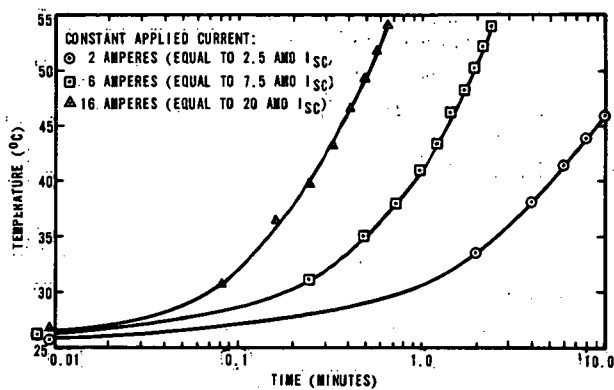


Figure 5. Temperature versus time at three current levels for ATM solar cell module.

As a result of this testing, it was decided that sufficient conservatism would result from limiting the power application of one I_{SC} maximum to approximately 4 s. This would ensure operation in the relatively flat portion of the three curves shown in Figure 5.

Temperature Considerations

Figure 6 shows dark characteristic curves for an ATM solar cell module for temperatures from 0°C to 100°C in temperature increments of 10°C. These curves were obtained by applying a varying voltage to an ATM module in a temperature-controlled test chamber. The curves were obtained to establish temperature coefficients for the modules. By arbitrarily selecting a value on the current axis

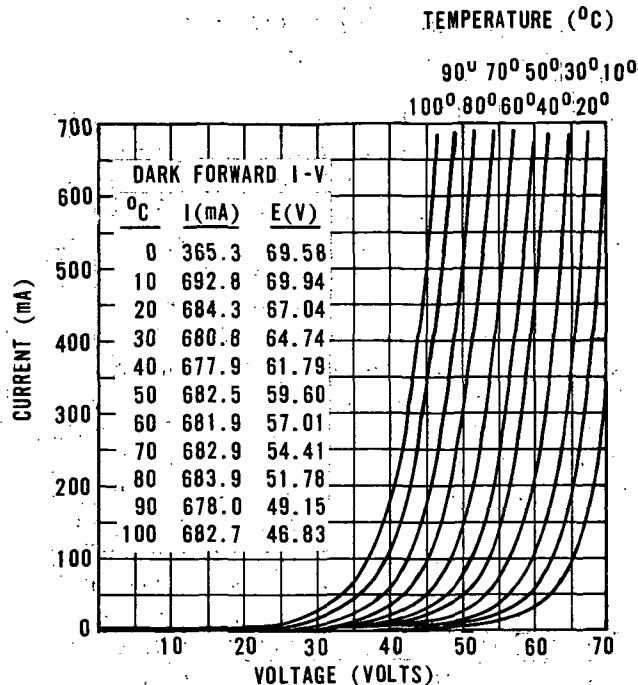


Figure 6. Current versus voltage for ATM solar cell module.

and examining the voltages on each of the curves corresponding to that current value, it can be seen that as the temperature decreases, the voltage increases. Also, by arbitrarily selecting a value on the voltage axis and examining the corresponding currents on each of the curves, the current is seen to increase as the temperature increases, though at a slower rate. These relationships are a result of the fact that for a silicon solar cell, voltage varies inversely with temperature while current varies directly with temperature.

A knowledge of the temperature at which the dark characteristic test is performed is very important to accurately interpret the results, as can be seen from an examination of Figure 7. This figure shows the effect on the panel dark characteristic curve of a varying number of modules being disconnected from the panel electrical harness. Since the modules are connected in parallel on the panel, disconnecting modules results in a decrease in current drawn for the same amount of voltage with a resulting shift of the curve to the right. However, temperature changes also shift the curve (to the right for a decrease and to the left for an

increase in temperature) while maintaining the shape of the curve essentially the same as the shape resulting from various numbers of modules being in parallel. Therefore, unless the temperature is known accurately, it is difficult to determine if a curve shift is a result of an "open" module or merely a change in temperature.

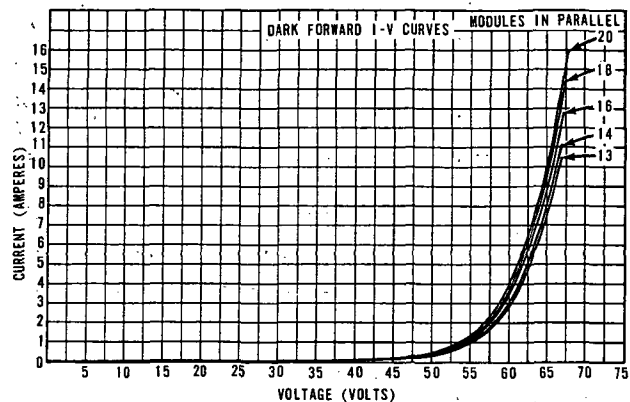


Figure 7. Dark I-V curves at 25°C for an ATM panel with a varying number of modules in parallel.

Since flight temperature channels on the ATM are at a premium, only three of the four and one-half panels on each wing have sensors. These sensors must be used to determine array temperature during checkout. The temperature of panels without sensors must be obtained by interpolation. Therefore, the accuracy and validity of the dark characteristic test results are dependent upon the temperature stability and uniformity of the stowed wing.

Effect of Series and Parallel Resistances

The effect of various resistances in series with an ATM solar cell panel on the panel's dark characteristic curve is shown in Figure 8. This resistance is composed of wiring, connector, and contact resistances. As shown in the figure, an increase in this resistance shifts the upper portion of the curve to the right. This resistance should be kept to a minimum and must be known to minimize its contribution to the error band. The effect of

series resistance in the test setup is minimized by utilizing the same test equipment and cabling at each test location.

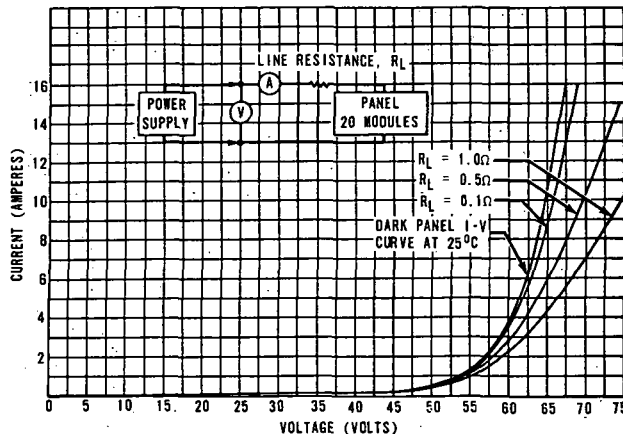


Figure 8. Effect of various line resistance values on dark I-V characteristics.

The effect of resistance in parallel with the solar cell modules can be seen in Figure 9. It is possible for a low R_{SH} condition to occur through a low impedance shunting path at the connector or a leakage path that may develop between the positive and negative leads. As shown, an increase in shunt resistance shifts the curve downward and to the right, appreciably changing the shape of the curve.

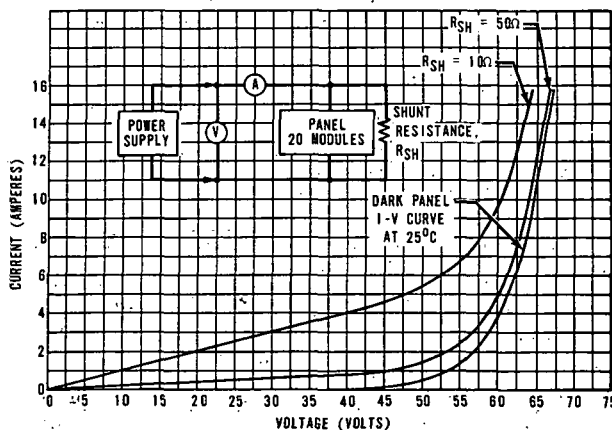


Figure 9. Effect of various shunt resistance values on dark I-V characteristics.

ATM DARK CHARACTERISTIC TEST SETUP

The test setup for obtaining the dark characteristic curves for the ATM program is shown in Figure 10. Power is provided by three voltage-programmable power supplies in series (designed to supply 90 V, 16 A), which provide a programmed voltage sweep of approximately 4-s duration. Simultaneous sensing is provided by two digital voltmeters, one to read current and the other to read voltage during the sweep. Control and data reduction are provided by use of a computer capable of being programmed in BASIC, FORTRAN, or ASSEMBLER language and containing an 8000-word memory and various input-output and data storage devices. Data are acquired for each of the panels individually, and switching is accomplished by means of relays to allow expedient checkout of an entire wing. In addition to the equipment shown, a plotter will be available for plotting the dark characteristic curves. The system shown is programmed to record the voltage and current for 40 fixed current values. Each time the test is performed, voltages at the same 40 current points will be recorded for comparison with previously acquired data. The computer is programmed to correct raw data for temperature effects and with additional programs for data reduction. In addition, safety features such as voltage, current, and time cutoffs are incorporated into the system to protect the solar array in the event of malfunctions.

DARK CHARACTERISTIC CHECKOUT OF THE ATM

The dark characteristic checkout for the ATM solar array will be performed in the following test phases:

- Post-Assembly Checkout (All Wings — Flight and Prototype)
- Post-Vibration Testing (All Wings — Flight)
- Post-Thermal-Vacuum Testing (One Wing — Prototype Only)
- Prelaunch Testing (All Wings — Flight)

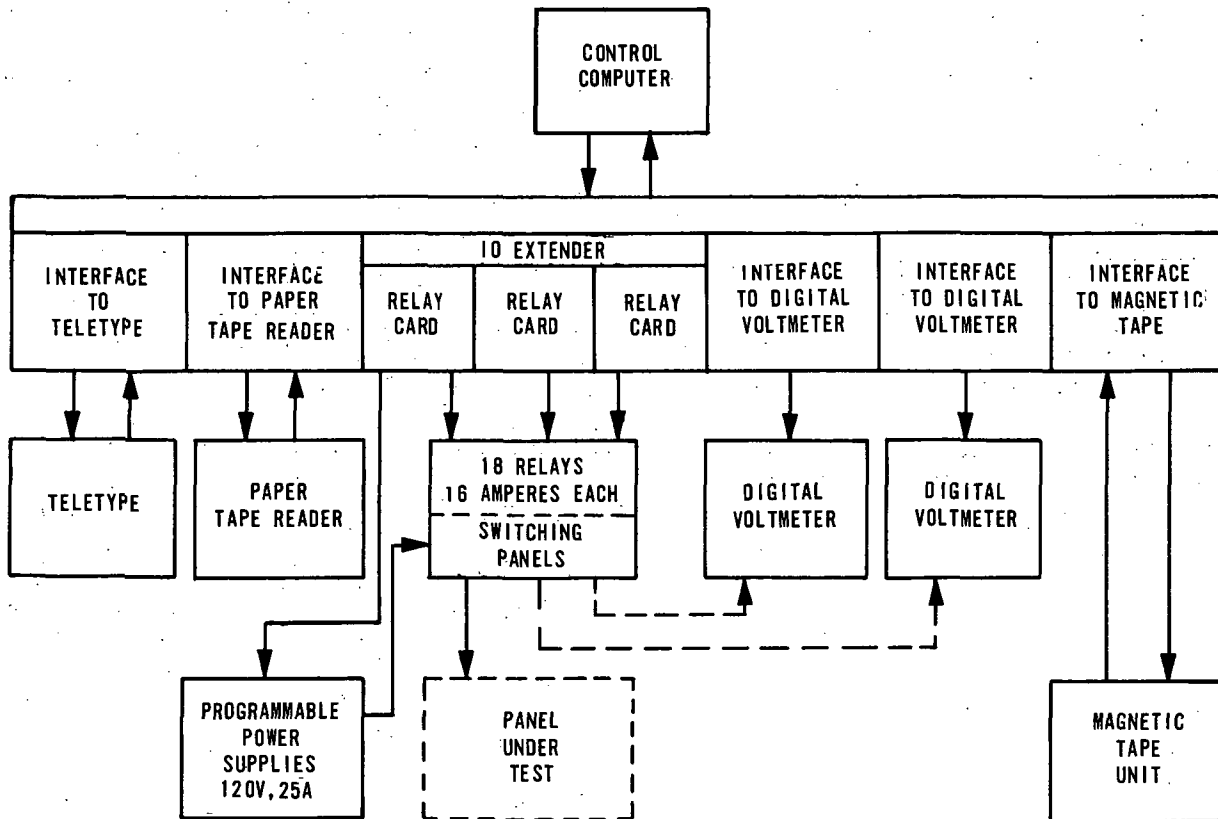


Figure 10. Dark I-V checkout system.

Testing will be performed for two test configurations as follows:

- Configuration I is the complete ATM wing assembly including all wiring and cabling, in a folded and cinched mode, not attached to the ATM vehicle.
- Configuration II is the complete ATM wing assembly including all wiring and cabling, folded and cinched, mounted on the ATM vehicle and electrically mated to the ATM Charger/Battery/Regulator Module (CBRM's). All four wings will be mounted on the ATM vehicle and connected to the CBRM's for this test. This is necessary to check out the half-panels.

Dark characteristic testing will be performed initially during post-assembly checkout of the array. At this time, three curves will be taken and compared to establish a "fingerprint" band. Three curves then will be taken at each of the other test phases, a band will be established, and a comparison will be made to the original "fingerprint."

Verification testing in support of the MSFC dark characteristic checkout for the ATM solar array was performed by Martin-Marietta in Denver, Colorado. As a result of this testing, it was determined that it is very important to consider dark characteristic checkout during the initial design of the array to ensure compatibility between the array and the checkout equipment. In particular the following points should be considered:

1. Design of the array should provide for electrical access for the dark characteristic test at the electrical module level.
2. Access should be provided on the array side of any blocking diodes used.
3. Provision should be made for obtaining the array temperature accurately during checkout.
4. Test system cable lengths should be minimized, and the same cable lengths should be used at each test location.
5. Checkout equipment should be designed to obtain the dark characteristic data in as short a time as possible to prevent array temperature rise.

CONCLUSIONS

The use of the dark characteristic for checkout of large area solar arrays is desirable because of the expense and difficulty of deployment in a 1-g environment. Faults that can be detected by the dark characteristic method are:

1. Modules disconnected from a panel.
2. Abnormally high leakage.
3. Large line impedances.

Damage to solar arrays during dark characteristic checkout can occur from overheating; however, this can be prevented by limiting the total time of voltage application.

Page intentionally left blank

NICKEL-CADMIUM BATTERY AND CELL INVESTIGATION FOR APOLLO TELESCOPE MOUNT (ATM) APPLICATIONS*

By

L. E. Paschal

ABSTRACT

An investigation of the nickel-cadmium (Ni-Cd) battery was conducted to determine optimum and acceptable battery performance within the ATM mission requirements. Battery performance characteristics were determined through a test program that investigated both charge control regimes and energy storage and thermal characteristics.

SUMMARY

This report presents the results of a test program conducted on Ni-Cd batteries at both battery and cell levels. At both levels 20-A-h cells of the type used on the ATM, containing control and recombination electrodes, were investigated.

Battery-level tests were performed to evaluate the characteristics and performance of 24- to 20-A-h Ni-Cd batteries when operated as a unit. The test specimens were subjected to simulated ATM orbital conditions, and the operational effect of charge control regimes and charge termination methods was observed. All voltage characteristics and energy storage capabilities were measured under various conditions.

Tests at the cell level were conducted and Ni-Cd characteristics such as charge efficiencies as a function of charge rate, temperature, and state-of-charge were determined. In addition, instantaneous

heat generation was measured under various cyclic and steady-state conditions.

The results of both types of tests were incorporated into a recommended Ni-Cd battery charge/discharge control regime that will meet the requirements of the ATM mission.

By-products of this test program are the state-of-the-art testing techniques, experience, and test facilities that have been developed. This capability can be used effectively to maintain and expand vital information on storage devices needed for future program requirements.

INTRODUCTION

This report summarizes the operational testing and evaluation program conducted by MSFC on Ni-Cd batteries for use on the ATM. The test program was initiated in 1967 to determine if the batteries could meet ATM mission requirements and to determine operating characteristics and methods. The ATM system power and Ni-Cd secondary battery charging power is provided by a solar array during the 58-min daylight portion of the orbit; during the 36-min night portion of the orbit, system power is supplied by the Ni-Cd batteries.

Ni-Cd battery requirements considered in the investigation include the following:

- Capability of cyclic operation for 8 months or 5000 cycles.

* The ATM Ni-Cd battery evaluation program was conducted by the Space Power Sources Section, Space Support Division, Sperry Rand Corporation under contract NAS8-20055 at the George C. Marshall Space Flight Center. The ATM single cell testing program was conducted by the Denver Division, Martin-Marietta Aerospace Group.

L. E. PASCHAL

- Capability of supplying a nominal load equivalent to 25-percent depth-of-discharge (DOD).
- Capability of operating within temperature limits from 0° to 30°C.

The test results herein reflect battery operating characteristics and parameters relative to simulated ATM orbital test conditions. Maximum voltage, charge requirement, capacity, thermal, and cyclic (charge/discharge) characteristics are presented.

Of all the recommended charging regimes and techniques, a constant current/constant voltage technique was considered most applicable for ATM applications [1].

The important cell and battery control parameters, based on the preceding charge regime, are as follows:

1. Typical maximum voltage levels were limited between 1.47 and 1.55 V during charge to prevent hydrogen evolution.

2. Charge current was limited by hydrogen evolution possibilities on the high side and by inefficient charge acceptance on the low side.

3. Recommended charge termination control was via a third-electrode signal; however, no specific load values or control limits were available.

TEST PROGRAM

The primary procedure followed throughout the test program was to conduct operational tests under simulated ATM orbital conditions, evaluate the battery parameters and performance, and perform specific tests for investigation of specific characteristics or parameters. The ATM orbital conditions were as follows: (1) charge time, 58 min; (2) discharge time, 36 min; and (3) temperature, -20°C to 40°C.

The test specimens were General Electric 24-cell, 20-A-h Ni-Cd batteries. The three types of cells used are shown in Table 1.

Each 24-cell battery was mounted in a restrainer designed by the battery manufacturer. Thermal control of the cells was maintained by airflow over heat sinks located on the large face of each cell and extending beyond the bottom of each cell. The ambient battery temperature was maintained within ±1°C with a temperature chamber.

TABLE 1. NICKEL-CADMIUM CELL TYPES

Leading Particulars	Type AB09	Type AB10	Type AB12
Capacity, A-h			
Rated	20	20	20
Average	25	25	25
Third Electrode	None	Type B, C	Type C
Recombination Electrode	No	No	Yes
Precharged Cd Plate	No	No	Yes
Electrolyte Volume (34% KOH)	68 cm ³	68 cm ³	72 cm ³
Weight, kg (lb)	0.889 (1.96)	0.889 (1.96)	0.889 (1.96)
Dimensions, cm (in.)			
Height	18.176 ± 0.038 (7.156 ± 0.015)	18.176 ± 0.038 (7.156 ± 0.015)	18.176 ± 0.038 (7.156 ± 0.015)
Width	7.61 (2.995)	7.61 (2.995)	7.61 (2.995)
Thickness	2.29 (0.903)	2.29 (0.903)	2.29 (0.903)

During the battery level tests, the cells were electrically connected in series. The battery was controlled by a programmable ATM-orbit-simulating electronic control package. A 700-W power supply simulated the ATM solar array output. The ATM electrical load was simulated with an electronically controlled load bank. Cyclic timing was performed with two tandem controlled clocks.

TEST RESULTS

Maximum Voltage Characteristics

The original battery charge regime was a combination of a constant current and constant voltage charge and is shown in Figure 1. The charge, which was 58 min in length, was initially at 10-A constant current. This charge level was maintained until the total battery voltage reached a pre-set level determined by the maximum allowable individual cell voltage of 1.47 V at 25°C. When the voltage of any cell reached 1.47 V during the first charge cycle, the charger was adjusted to convert the charge from constant current to constant voltage. During the remaining charge time, the battery voltage remained constant. During the 36-min discharge time, the battery load was

maintained at 200 W. The initial tests were performed with AB09 cells. Figure 2 depicts the relationship between the charge current and several individual cell voltages. Of particular importance is the individual cell voltage divergence after 100 percent of the previous discharge has been delivered to the cells. Note the consistent performance of the cells; i.e., cell 10 will remain the high cell and cell 8 will remain the low cell as long as the battery is subjected to continuous cyclic operation.

Cell voltage divergence is caused by a difference in the capacity of the individual cells of a battery. The capacity difference may be caused by an initial cell capacity mismatch during battery assembly or as a result of a "memory" phenomenon. Memory is an unexplained loss of usable capacity and is a function of temperature and cyclic history.

One method used to reduce the effects of the voltage divergence shown in Figure 2 is to reduce the constant voltage charge by at least 0.6 V below the maximum voltage to which the battery is charged. This method is shown graphically in Figure 3. A second method used to reduce the divergence was to match all the cells in a battery on an ampere-hour-in and ampere-hour-out basis. This could ensure that each cell in a battery would achieve a full charge

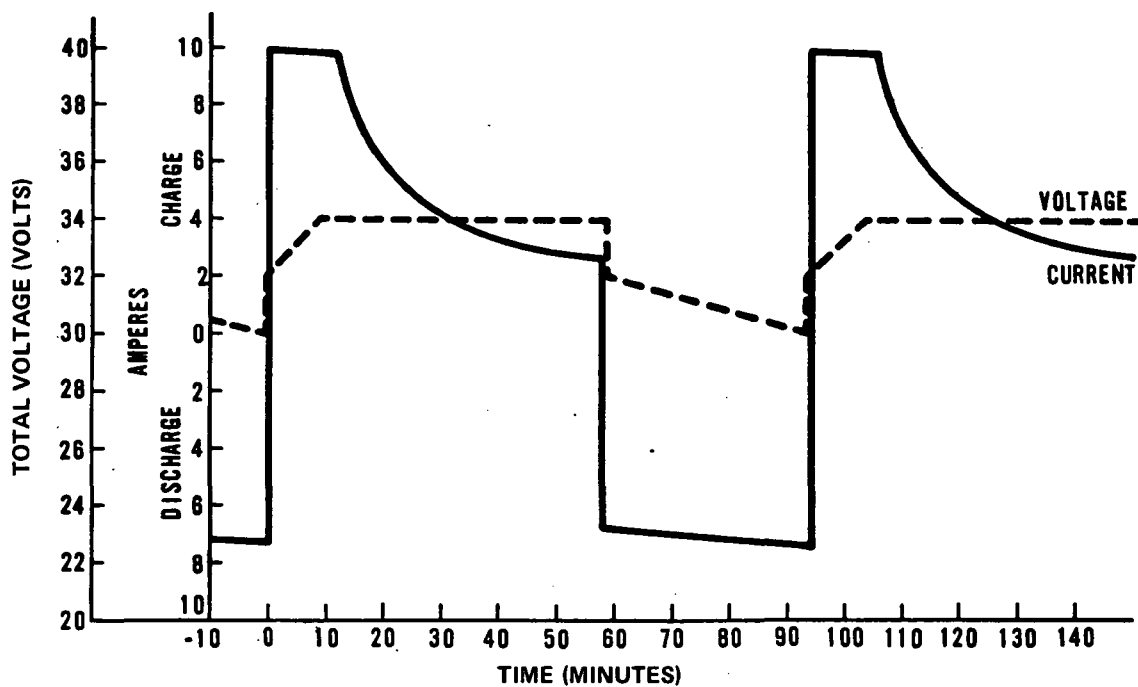


Figure 1. Initial charge regime — AB09 battery.

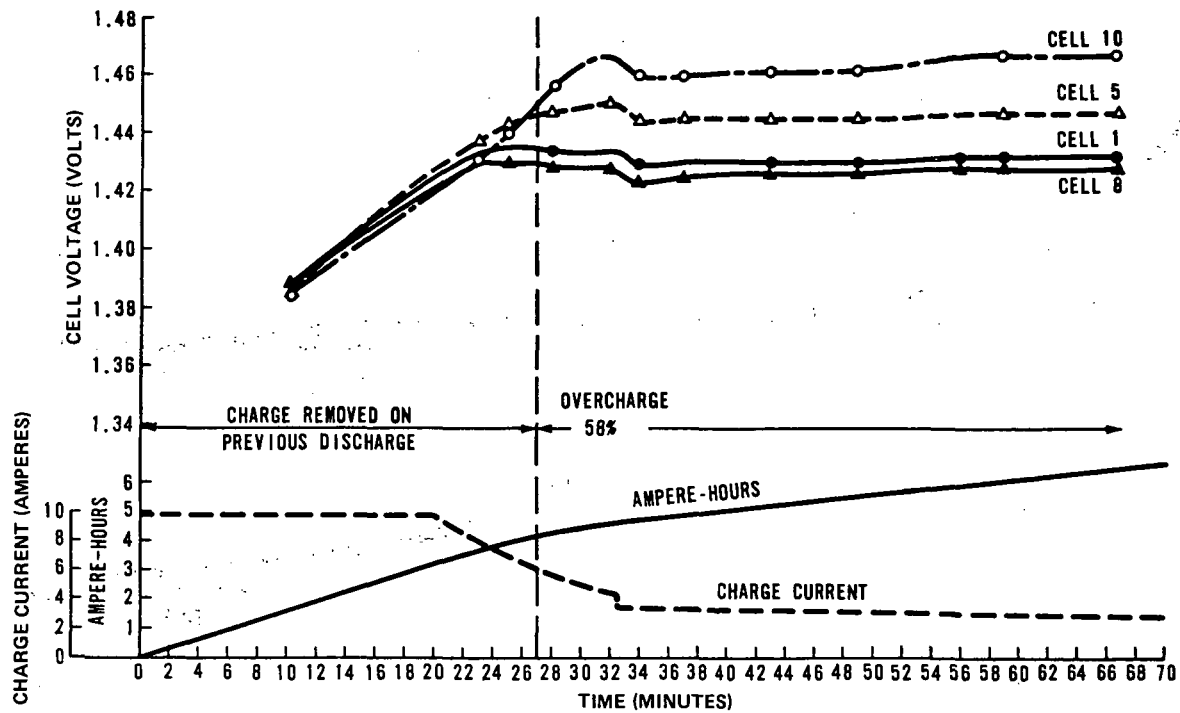


Figure 2. Initial charge regime — cell characteristics, AB09 battery (cycle 247).

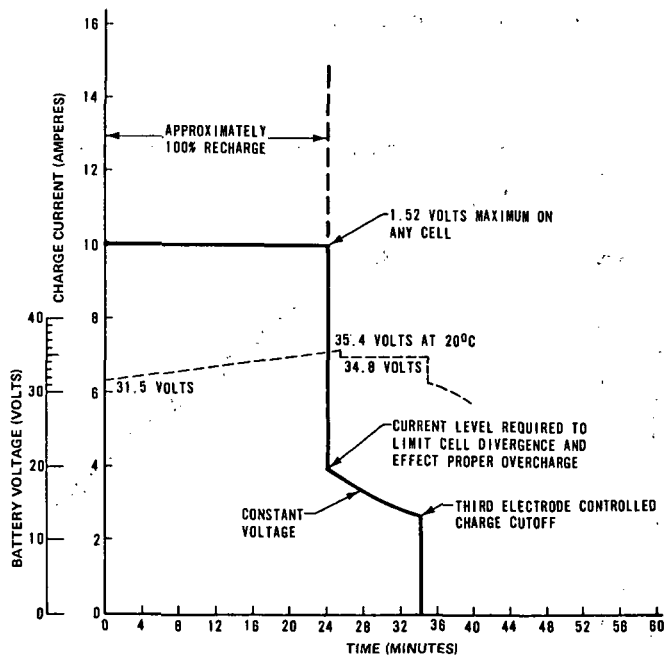


Figure 3. Recommended charge regime as a result of initial AB09 tests.

at the same time; therefore all cells would have similar voltage characteristics.

Cells with similar cell voltage characteristics also allow a higher maximum battery voltage to be used before the voltage of any cell exceeds the theoretical hydrogen evolution potential at some value between 1.47 and 1.55 V.

The improvement in cell performance as a result of the change in charge regimes is shown in Figure 4, which compares test data of a battery using matched AB10, third-electrode cells with a battery using unmatched AB09 cells. Both batteries are the same electrically. At 20°C the maximum allowable charger voltage on the AB10 battery was 35.4 V and on the AB09 battery it was 34.8 V. These voltages were determined by the maximum allowable cell voltage. The increased capacity of the AB10 battery is attributed to the higher charge voltage obtained through the use of matched cells in the AB10 battery.

The maximum voltage to which the battery can be charged is temperature dependent. This

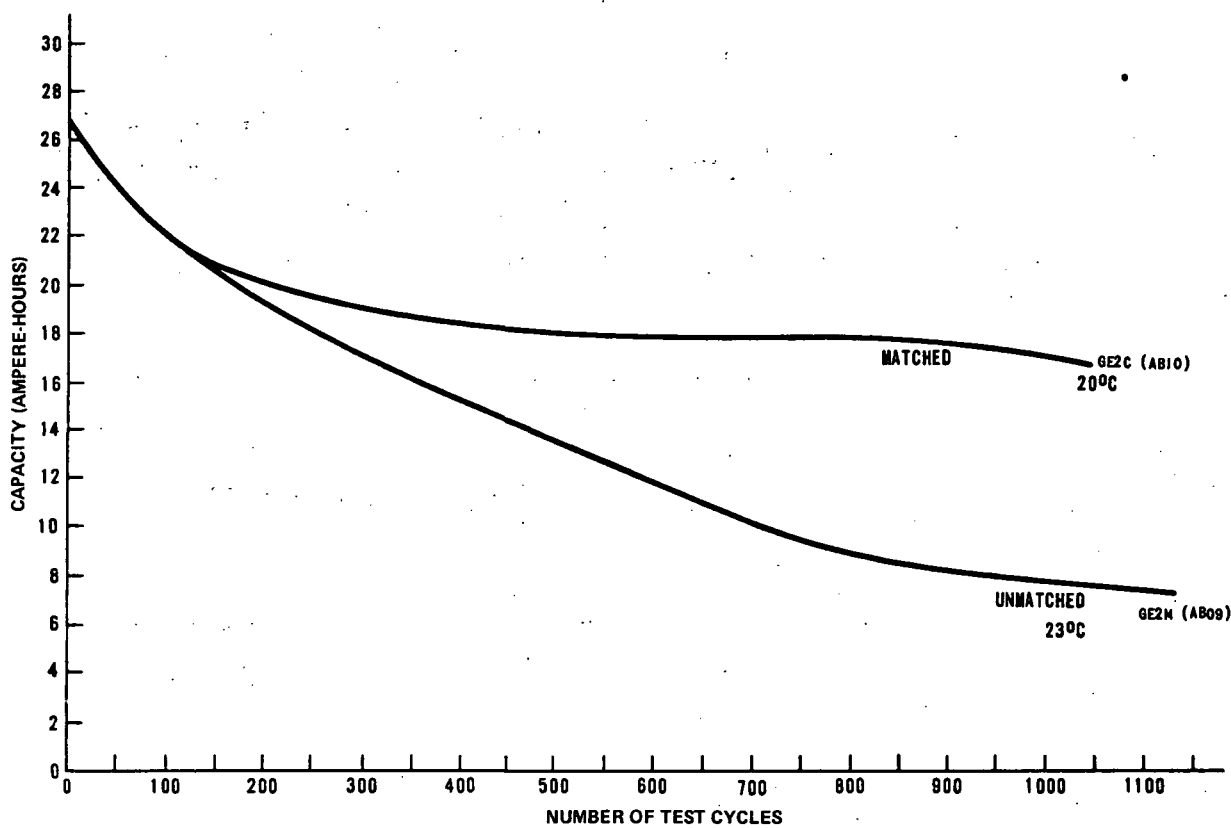


Figure 4. Battery characteristics — cell matching effectiveness.

temperature dependence is caused by the negative temperature coefficient of the cell voltage, which is reported to be $2.5 \text{ mV}/^{\circ}\text{C}/\text{cell}$. This value reflects changes in overvoltage, equilibrium potential, and potential drops across the electrolyte and electronic impedances. On a 24-cell basis, the battery voltage values as a result of the temperature coefficient are shown in Figure 5. The values in the figures were empirically determined.

As a result of the cell performance noted in these tests, several factors have become apparent:

1. The effect of cell voltage divergence during charge can be reduced by limiting charge time during which the battery is subjected to a maximum voltage.
2. The effects of memory over long periods of continuous cycling can be reduced by initially charging the battery to its full capacity prior to cycling, and by adjustments of the maximum battery voltage and the constant voltage charge rate at cycle 1 to their maximum allowable safe operating levels. This procedure causes the effective capacity to remain above useful levels for longer periods of cycling.

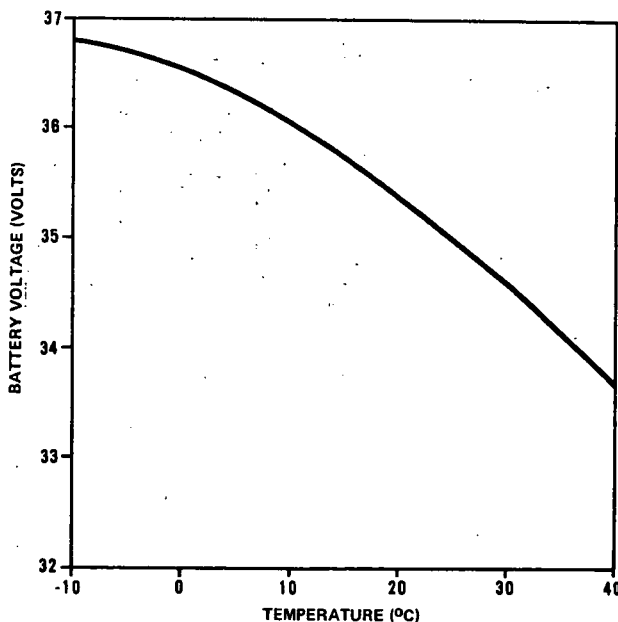


Figure 5. Voltage level as a function of temperature.

Charge Rate

Investigation of the effect of charge rate on Ni-Cd battery performance was conducted on individual cells. Results of the charge rate investigation are shown in Figure 6, which depicts the cycle efficiency as a function of temperature and charge rate.

Figure 7 shows typical data for one temperature at various charge rates for the constant current charge phase. It shows clearly the reduced charge acceptance or lower cycle efficiency caused by decreasing charge rate. Obviously, increasing temperature also decreases efficiency. The cycle efficiency shown indicates the effectiveness of the cycle regime during the constant current charge

only. Since the constant voltage phase of the charge regime is not included, the indicated capacity does not reflect actual cyclic capacity.

As a result of solar array limitations and hydrogen generation at low temperatures internal to the cell, the maximum charge rate for the ATM batteries was limited to 15 A or 0.75C. Figure 8 illustrates the cell voltage characteristics for various temperatures with a 15-A charge rate. The dashed line represents the constant current (15 A) charge cutoff point of the ATM battery charge regime. Note that a 100-percent state-of-charge is available only at temperatures close to 30°C, when the charge is limited to a 15-A, constant current charge. A fully charged state is available in the ATM charge regime by augmenting the

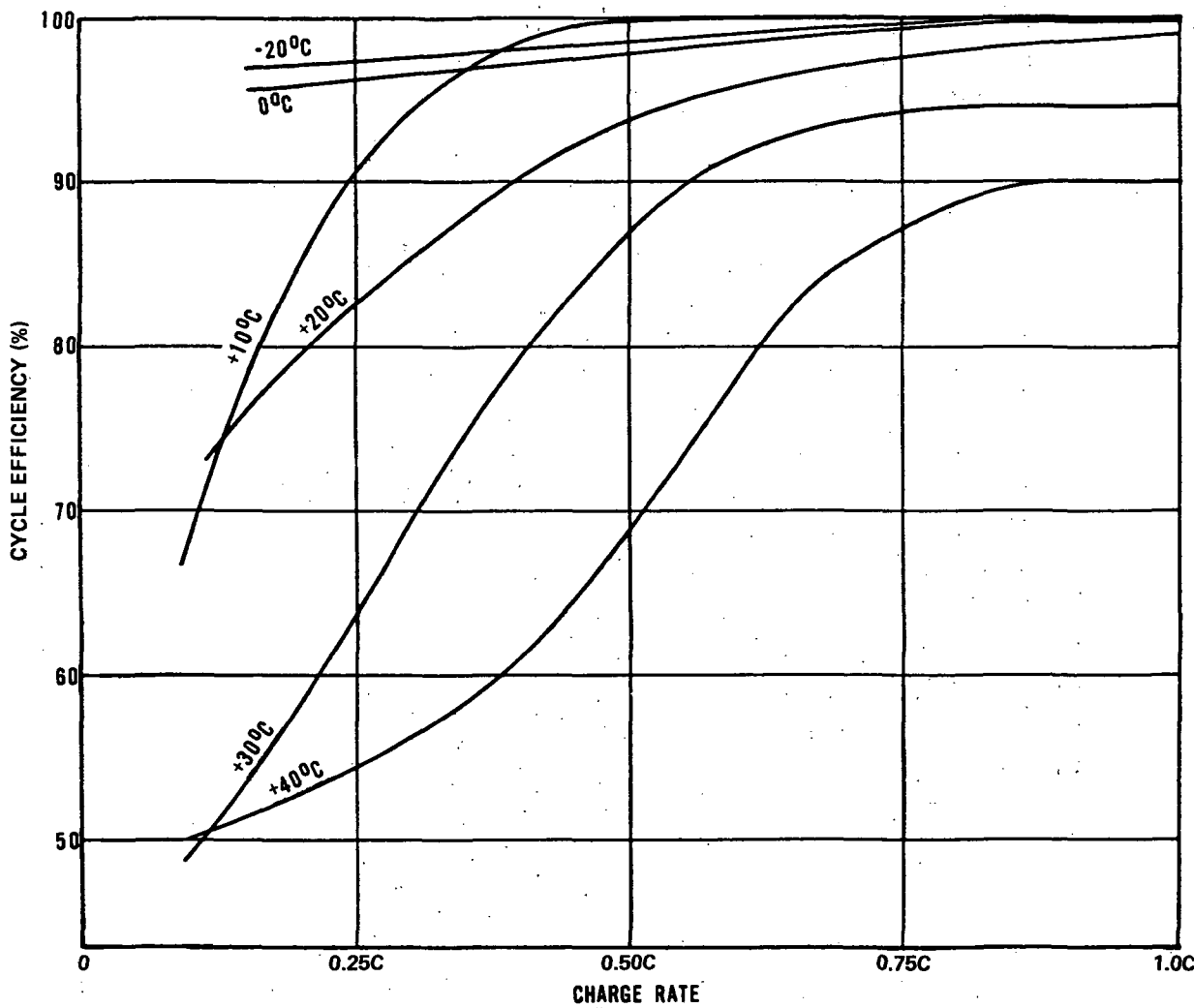


Figure 6. AB12 average cycle efficiencies.

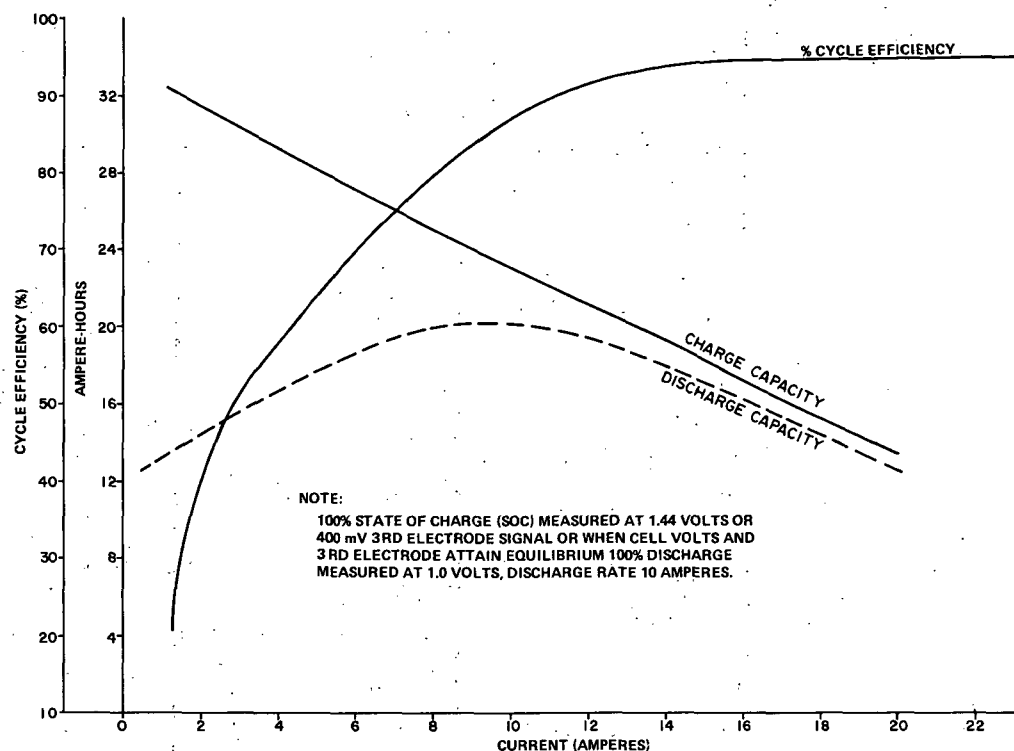


Figure 7. AB12 cells average cycle efficiency — 30° C, constant current charge only.

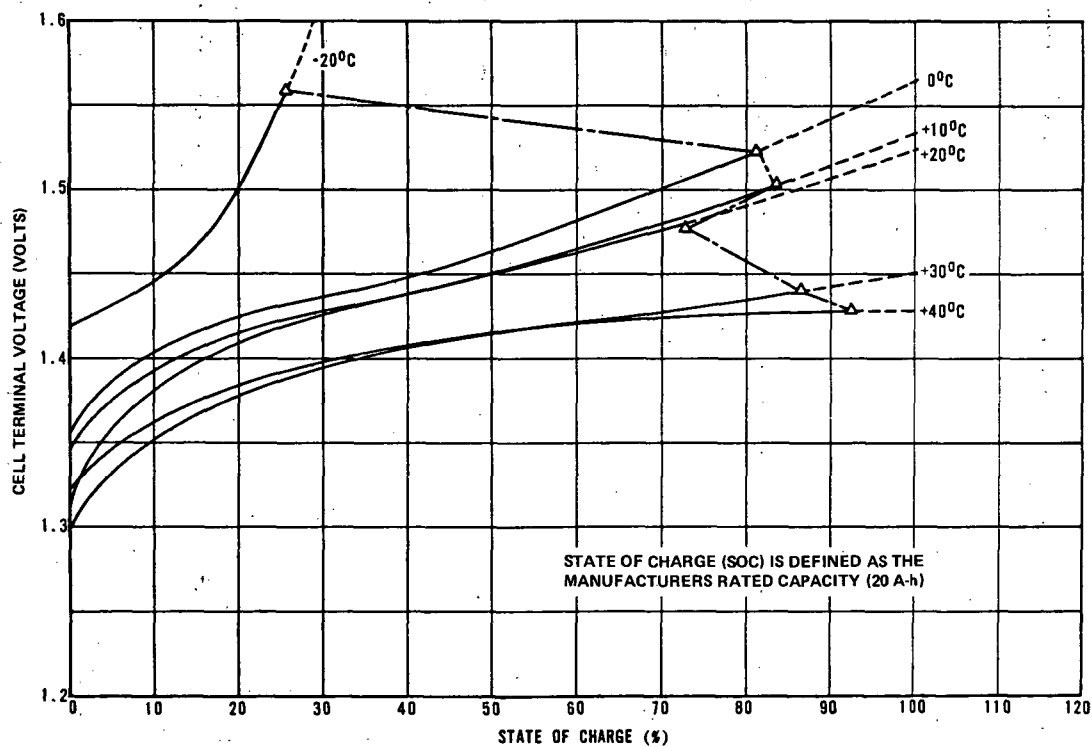


Figure 8. AB12 average charge voltage, state-of-charge characteristics — 0.75C.

constant current charge with a constant voltage charge as noted in the recommended charge regime (Fig. 3).

Ni-Cd Cell Thermal Characteristics

A simple but effective means of determining instantaneous thermal output from cells under various cycle regimes and temperatures has been developed using a thermal vacuum chamber.

The general arrangement of the inner chamber schematic is shown in Figure 9. The cell, with a calibrated heater attached to its upper face, is mounted on heat flux sensors that permit exothermic or endothermic heat flux to flow between the cell and cold sink.

Unmeasured heat loss because of radiation is minimized by two radiation shields, and conduction is limited to the cell electrical terminations and the

support column. An operating vacuum of $8.67 \times 10^{-5} \text{ N/m}^2$ ($6.5 \times 10^{-7} \text{ T}$) ensures that convection is minimal. The total thermal control ensures a heat balance having less than 4-percent error.

Cell temperature is maintained within 0.2°C by using an electronic master/submaster controller that changes the cold sink temperature when a slight temperature swing occurs at the cell. The corresponding heat flow through the flux sensors maintains a constant cell temperature.

Figure 10 shows the charge phase of the recommended MSFC charge regime at 30°C when the cell and system is isothermal. It can be seen that the thermal output is endothermic for the first 17 min and then rises to 84 W. This curve represents an instantaneous thermal output during the charge but does not indicate the charge acceptance. It can be seen that the third electrode closely tracks the thermal output and implies that a direct relationship exists between oxygen evolution

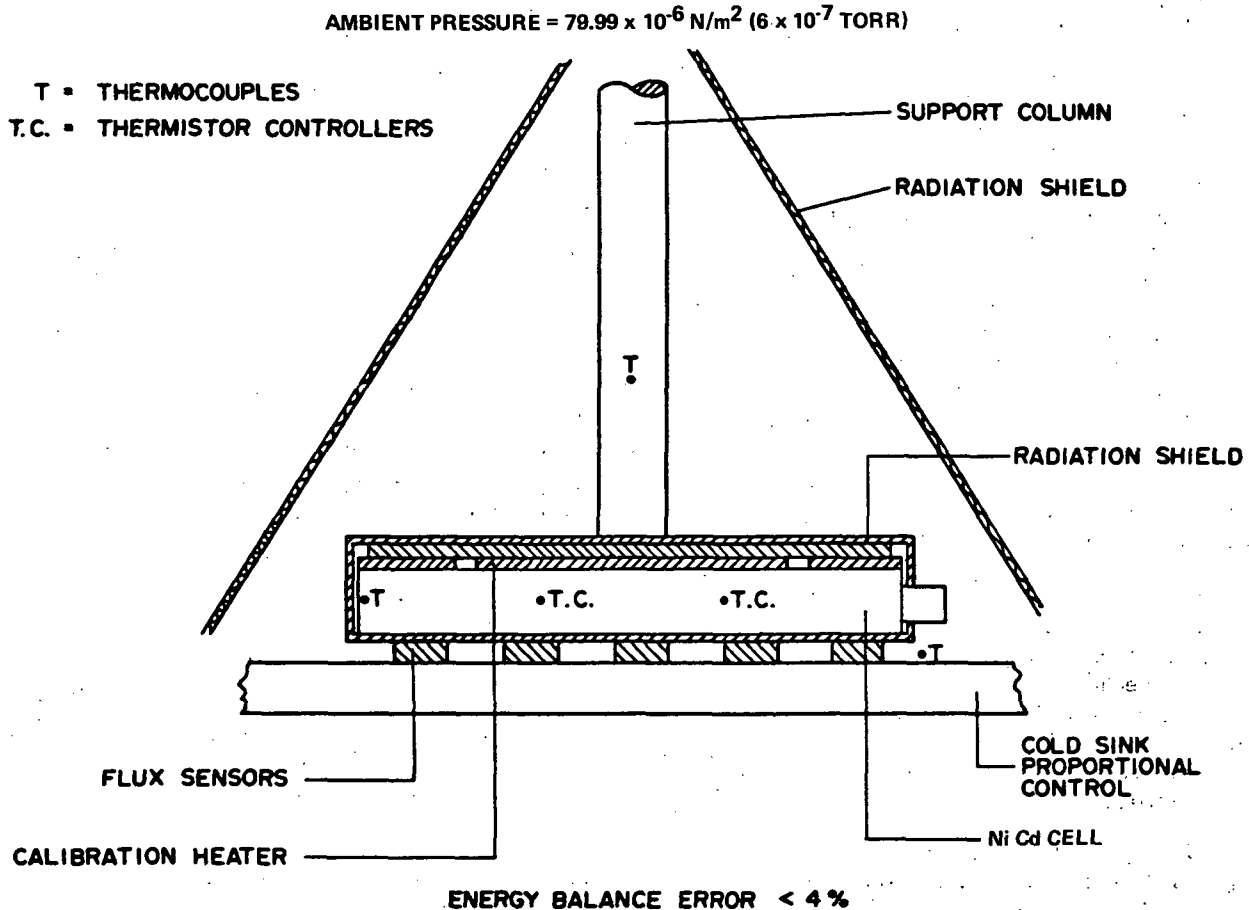


Figure 9. Thermal evaluation test layout.

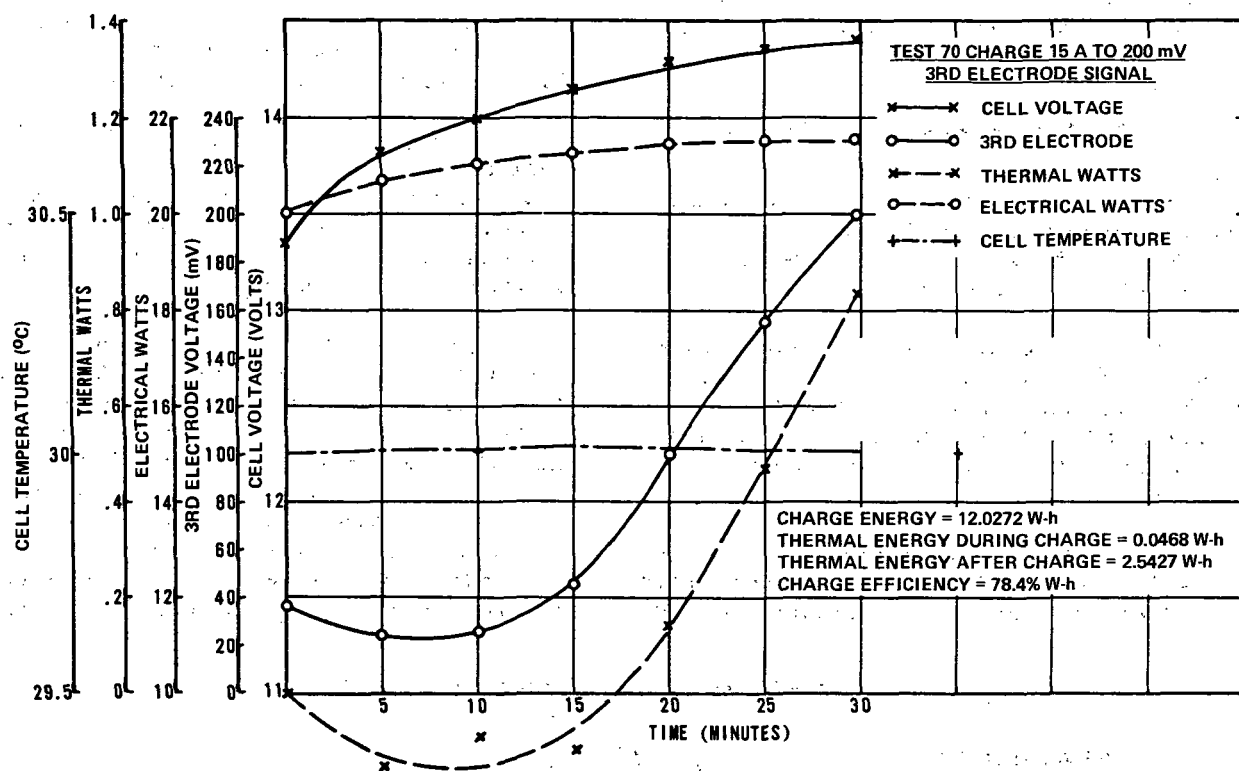


Figure 10. Thermal characteristic — 30° C, charge from 30-percent DOD.

and thermal output. This relationship continues after the charge is terminated, when oxygen recombines causing a reduction in third-electrode signal and thermal output, as shown in Figure 11. During discharge from an isothermal state (Fig. 12), oxygen recombination does not occur and the instantaneous thermal output is again seen. Since there is no way to maintain the whole cell at the same temperature, there is a tendency for the center of the cell to lag thermally, resulting in the thermal overflow seen after discharge termination. Since heat absorption by the cell will occur quicker at the beginning of charge, the overflow can be added inversely to the thermal increase during discharge. The result of this is an instantaneous discharge efficiency that is constant. The discharge watt-hour efficiency within the limited bounds of the nominal ATM discharge is therefore always within the range of 85 percent, irrespective of temperature, state-of-charge, depth-of-discharge, and discharge rate.

Since the variation of the third-electrode signal repeats the cycle phase, the instantaneous thermal variation is also subject to the cycle phase. This response is depicted in Figure 13, which shows cyclic response after numerous stabilization cycles.

Thermal output is at a maximum when the charge begins. The endothermic reaction during charge rapidly reduces the thermal output, until the oxygen evolution and accompanying heat generation exceed the endothermic reaction. At this point, thermal output increases until charge termination occurs. Thermal output then continues to overflow during the open circuit time. An increase in thermal output again occurs during discharge. Figure 13 shows the thermal cyclic response when the charge cycle does not contain a constant voltage charge. Figure 14 shows what occurs when the constant voltage charge is included in the charge cycle. A significant increase in thermal output is the result of increased charge inefficiency at low current rates during the constant voltage charge.

Recharge Requirements

The cyclic operation of an Ni-Cd battery requires that more electrical energy be replaced during charge than is removed during discharge. This is evident from the cycle efficiency data. A measure of this is the recharge fraction (RF).

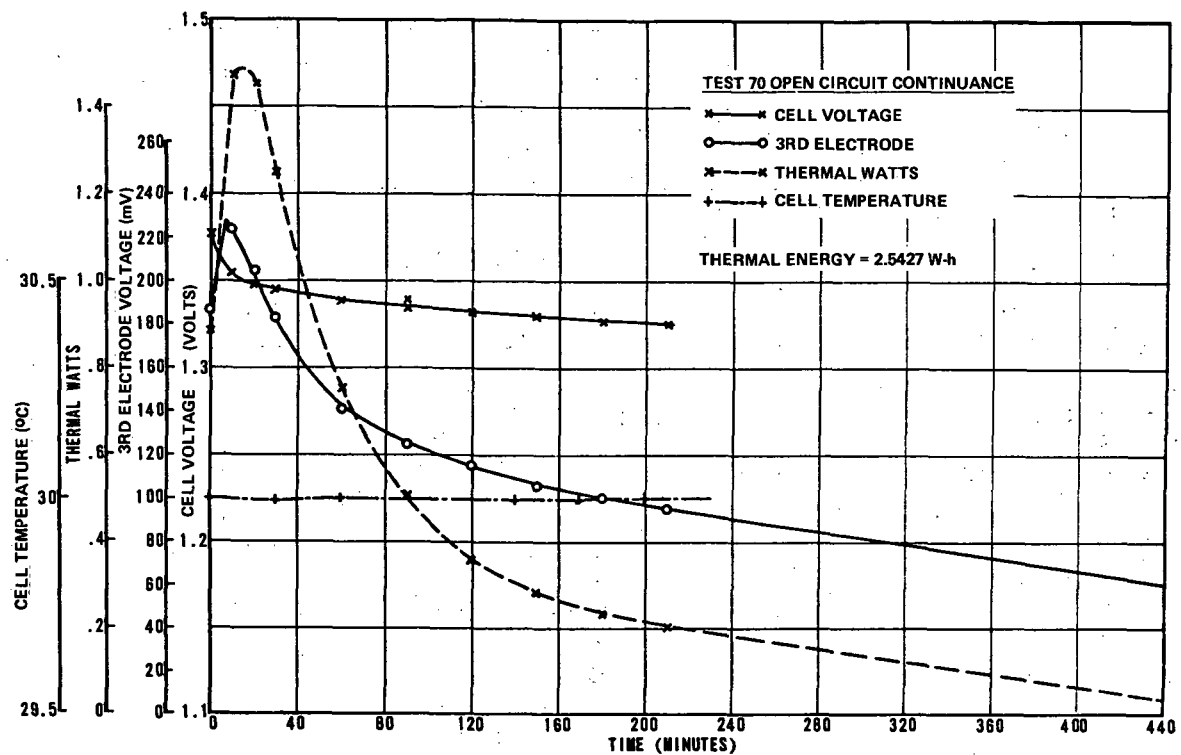


Figure 11. Thermal characteristic — 30° C, open circuit after charge.

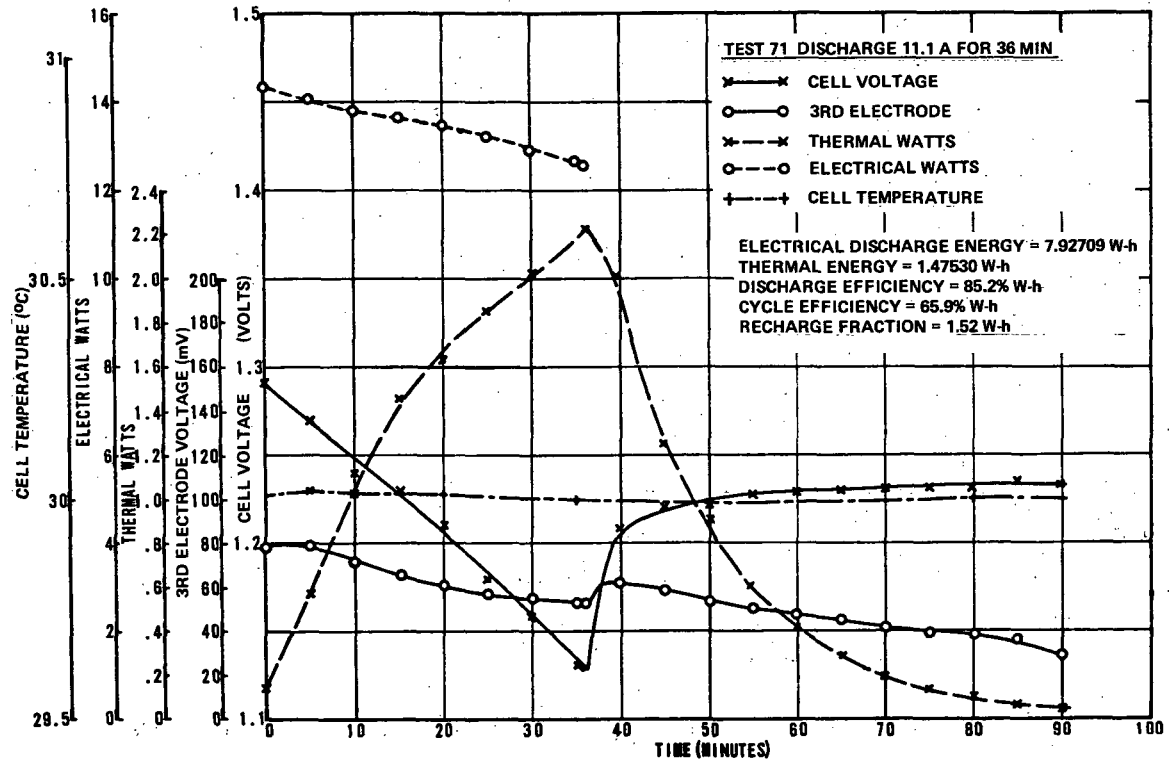


Figure 12. Thermal characteristic — 30° C, discharge 30-percent DOD.

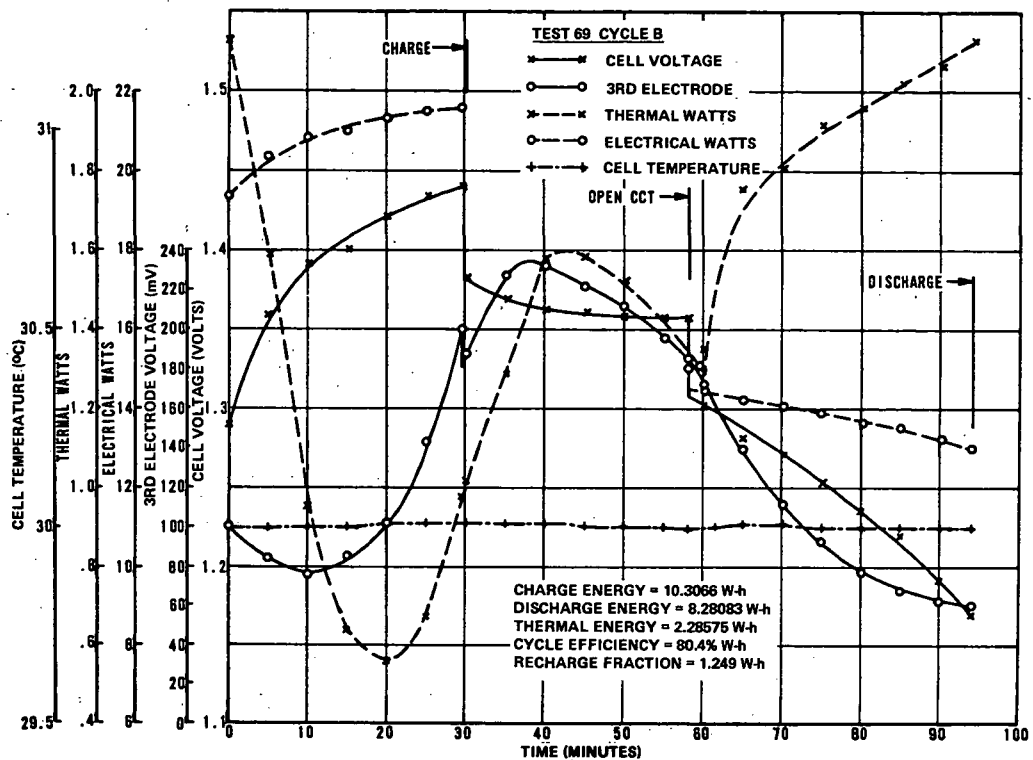


Figure 13. Thermal characteristic — 30° C, MSFC regime.

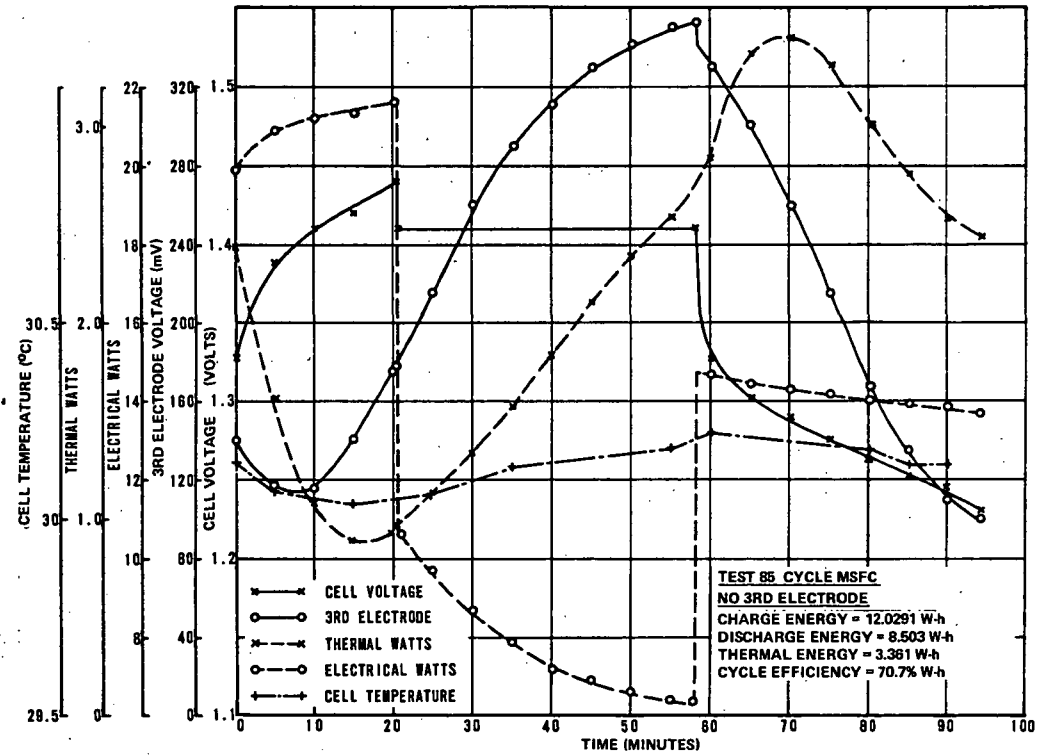


Figure 14. Thermal characteristic — 30° C, MSFC regime, no third electrode.

A recharge fraction is defined as the ratio of ampere-hours-in to ampere-hours-out. State-of-the-art Ni-Cd battery information at the initiation of the ATM program in 1966 indicated a minimum recharge fraction requirement of 120 percent at 20° C operating temperature. This recharge fraction will result in approximately 28 W of excess heat being generated by a 24-cell, 20-A·h Ni-Cd battery. The allowable ATM heat dissipation is limited to approximately 20 W per battery.

Tests were conducted to establish lower recharge fraction values suitable for operation of the battery within the ATM electrical and thermal specifications. Figure 15 depicts a typical simulated ATM orbital cycle.

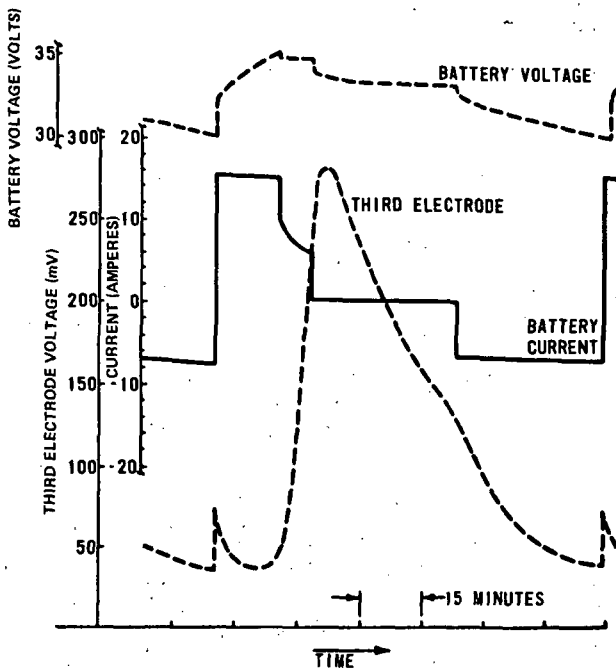


Figure 15. ATM test cycle — AB12 battery.

The test specimen was subjected to 2000 simulated ATM orbital cycles prior to recording the recharge fraction data. The results of the pretest cycles are noted later in Figure 26, cycles 0 to 2000. Although the indicated cycles were recorded primarily at 0° C, several data points reflect 20° C and 30° C cyclic performance. Since the measured capacity at cycle 2000 was above the rated battery capacity, it was assumed that the battery was being sufficiently recharged. This assumption was based on the capacity degradation from cycle 0 to 2000 being less than anticipated, based on all previous battery test data.

The results of the recharge fraction tests are shown in Figure 16. As shown, the required recharge varies as a function of load and temperature. The variation is the result of battery response to external conditions such as load and temperature.

An Ni-Cd battery has the highest charge efficiency when the state-of-charge is 80 percent or less. Conversely, the charge efficiency decreases when the state-of-charge increases above 80 percent. This factor accounts for the increase in the measured recharge fraction as the load is decreased.

Charge efficiency is also a function of temperature. As the temperature increases, the charging efficiency decreases. This factor causes the rise in recharge fraction as the battery temperature is increased.

The results of the recharge fraction test, together with the 2000 pretest cycles at 0° C and the 1500 post-test cycles (Figure 26, cycles 3000 to 4500) at 20° C, has indicated acceptable battery operation with an associated recharge fraction that reduces total battery heat to acceptable ATM levels.

Charge Termination Control — AB12 Tests

Tests were performed on a battery with AB12 type cells to determine a method whereby three redundant charge-termination control third electrodes could be chosen in a flight battery.

Typical signal data from the battery third electrodes are shown in Figure 17. The figure depicts 24 individual third-electrode signals recorded during cycle 62 and cycle 63 under steady-state cyclic conditions at 20° C and a 150- Ω load resistance. The most significant factor in Figure 17 is the difference in the third-electrode signal among 24 cells when all cells are subjected to identical cyclic conditions.

Figure 18 illustrates the performance of the third electrode in cell 21 under steady-state cyclic conditions at 20° C, with third-electrode load resistors having values between 75 and 1000 Ω .

Consider the third electrode as the composite circuit depicted in Figure 19. Assuming the internal generator to be a constant voltage source, the internal resistance appears as a variable resistor whose value may be determined by measurement of the voltage across the external load resistance.

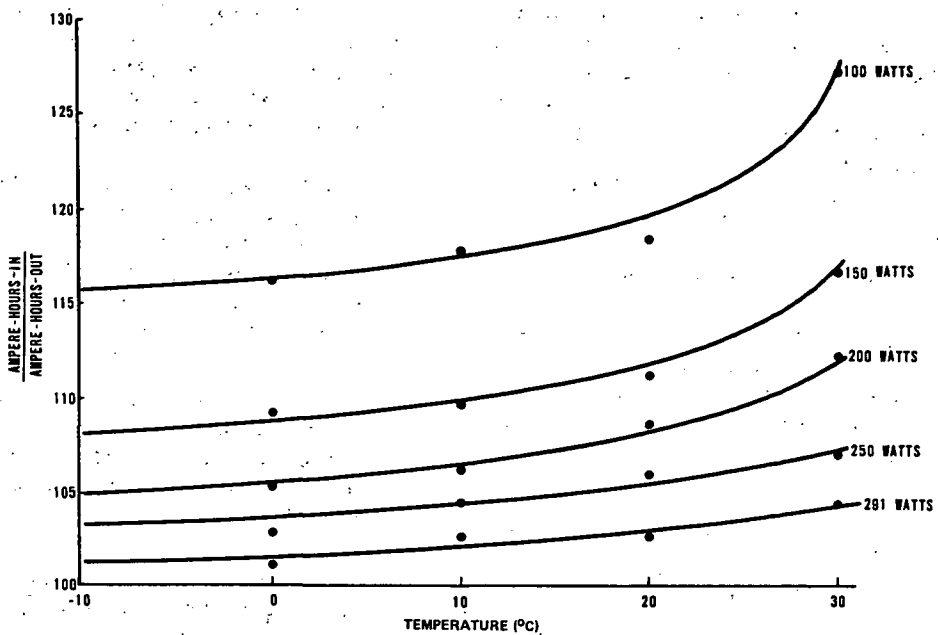


Figure 16. Recharge characteristics — AB12 battery.

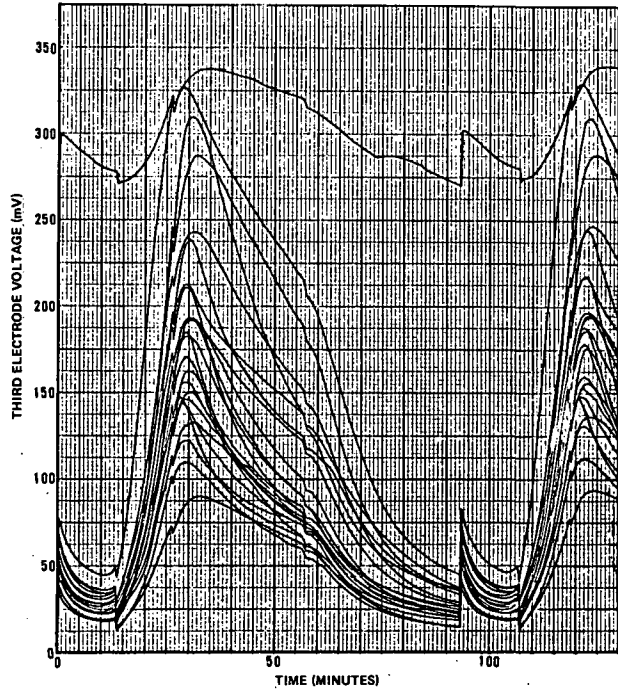


Figure 17. Third-electrode signal for 24 cells at 20°C — cycles 62 and 63, load resistance $150\ \Omega$ (AB12 cells).

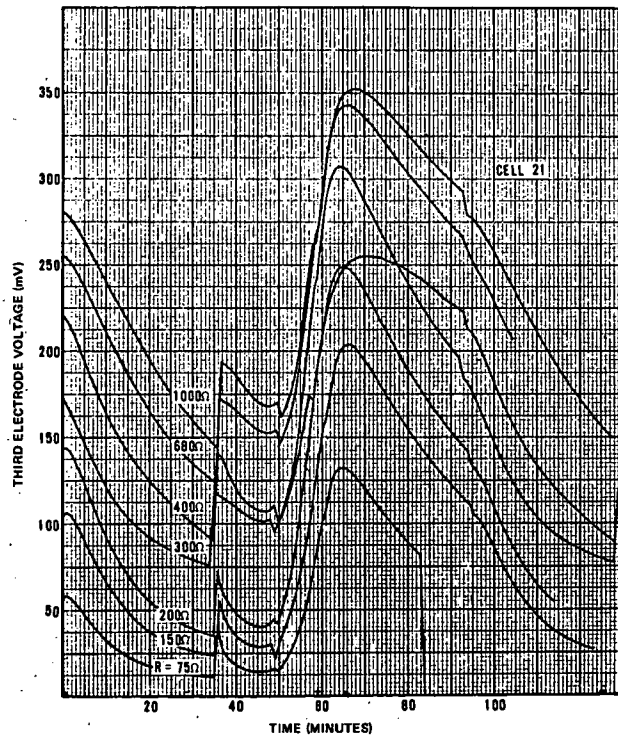
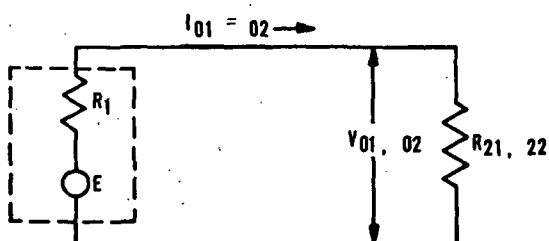


Figure 18. Third-electrode signals for a single cell at 20°C and varying load resistances (AB12 cell).



where:

E = internal generator

R_1 = internal resistance

R_{21} = a particular load resistance

R_{22} = a load resistance not equal to R_{21}

I_{01} = load current associated with the resistance R_{21}

V_{01} = potential measurement across the resistance R_{21}

V_{02} = potential measurement across the resistance R_{22}

Figure 19. Equivalent third-electrode circuit.

Then,

$$E = R_1 I_{01} + R_{21} I_{01} \text{ and } E = R_1 I_{02} + R_{22} I_{02}$$

thus,

$$R_1 I_{01} + R_{21} I_{01} = R_1 I_{02} + R_{22} I_{02}$$

Since,

$$V_{01} = R_{21} I_{01} \text{ and } V_{02} = R_{22} I_{02}$$

$$R_1 I_{01} + V_{01} = R_1 I_{02} + V_{02}$$

Therefore,

$$R_1 = \frac{V_{01} - V_{02}}{I_{02} - I_{01}} = \frac{\Delta V_0}{\Delta I_0} = \frac{\frac{V_{01} - V_{02}}{V_{02} - V_{01}}}{R_{22} / R_{21}}$$

The internal resistance characteristics of cell 21 were determined by using Figure 18 and the above derivation. The results of this analysis are shown in Figure 20. The figure is a family of curves that illustrate the internal electrode resistance characteristics during the control portion of the

charge cycle. Time as shown on Figure 20 can be correlated with the time axis in Figure 18.

When the third electrode is considered as a black box and the internal generator as a constant voltage source, the internal resistance appears as a variable resistor whose value is determined by the value of the external electrical load. As shown in Figures 20, 21, and 22, the internal resistance changes from positive values through negative values with the maximum resistance occurring between 150 and 200 Ω external load. Although all cells tested indicated maximum internal third-electrode resistance between 150 and 300 Ω external load, the signal values of each third electrode were not equal. Nonuniformity of the signal values must be eliminated in the flight battery which requires three redundant third-electrode charge-termination control signals. To achieve signal uniformity, the external load resistors will be chosen so that at charge termination all three signals will be of equal value. The mean value of the external load will be 200 Ω since this is the constant current point that facilitates calculation.

Several important third-electrode operating characteristics were determined during testing; one of these is the internal resistance of the third electrode, another is the temperature response, and a third is the nonuniformity of cell response when cells are subjected to identical cyclic conditions. These characteristics have determined the methods to be used to optimize the choice of charge-termination control third electrode.

Capacity Degradation Characteristics

The most important phase of the Ni-Cd battery investigation was to establish the useful battery capacity as a function of temperature and cyclic history.

Absolute battery capacity as a function of temperature was determined by subjecting a 20-A-h battery to a 30-A-h charge and, immediately thereafter, conducting a complete discharge at a 10-A rate until the voltage of any cell decreased to 1.0 V. These tests were performed within a temperature range of 0° C to 40° C in 5° C steps. The results are shown in Table 2.

Capacity degradation tests were performed at various temperatures on batteries containing type AB12 cells. These tests were intended to demonstrate the useful battery capacity characteristics.

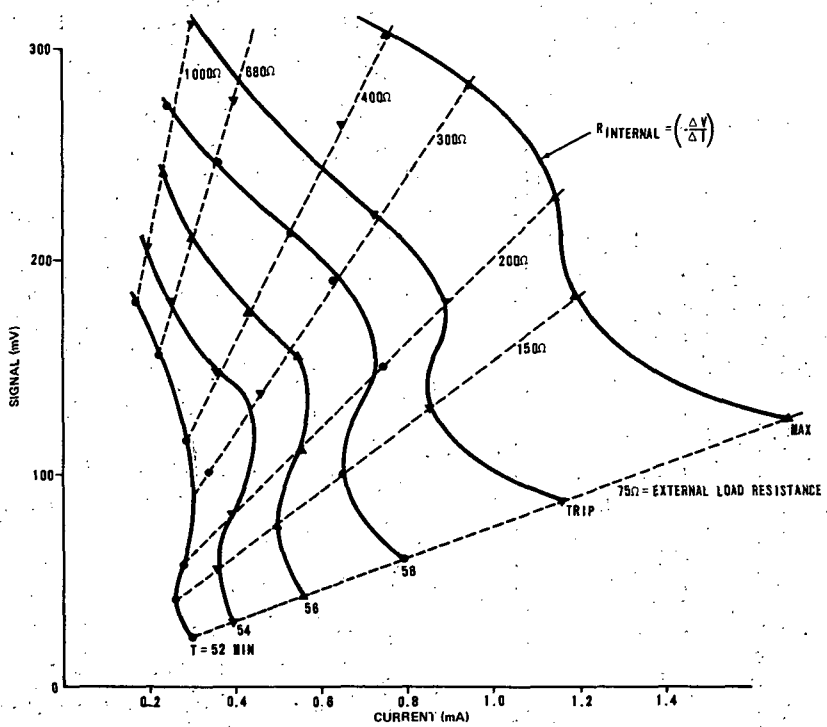


Figure 20. Internal resistance characteristics for cell 21 at 20° C (AB12 cell).

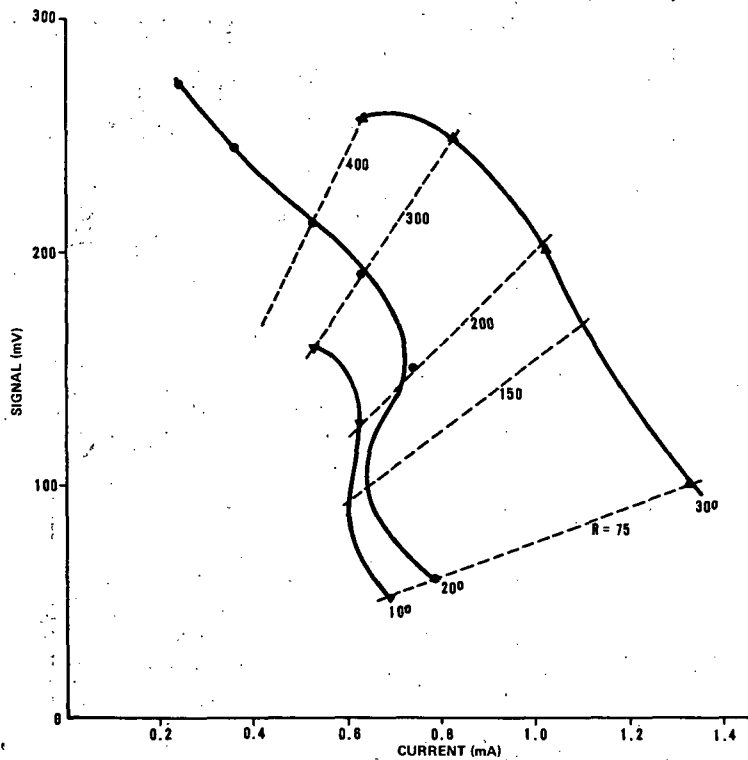


Figure 21. Internal resistance characteristics for cell 7 at varying temperatures and a particular state-of-charge (AB12 cell).

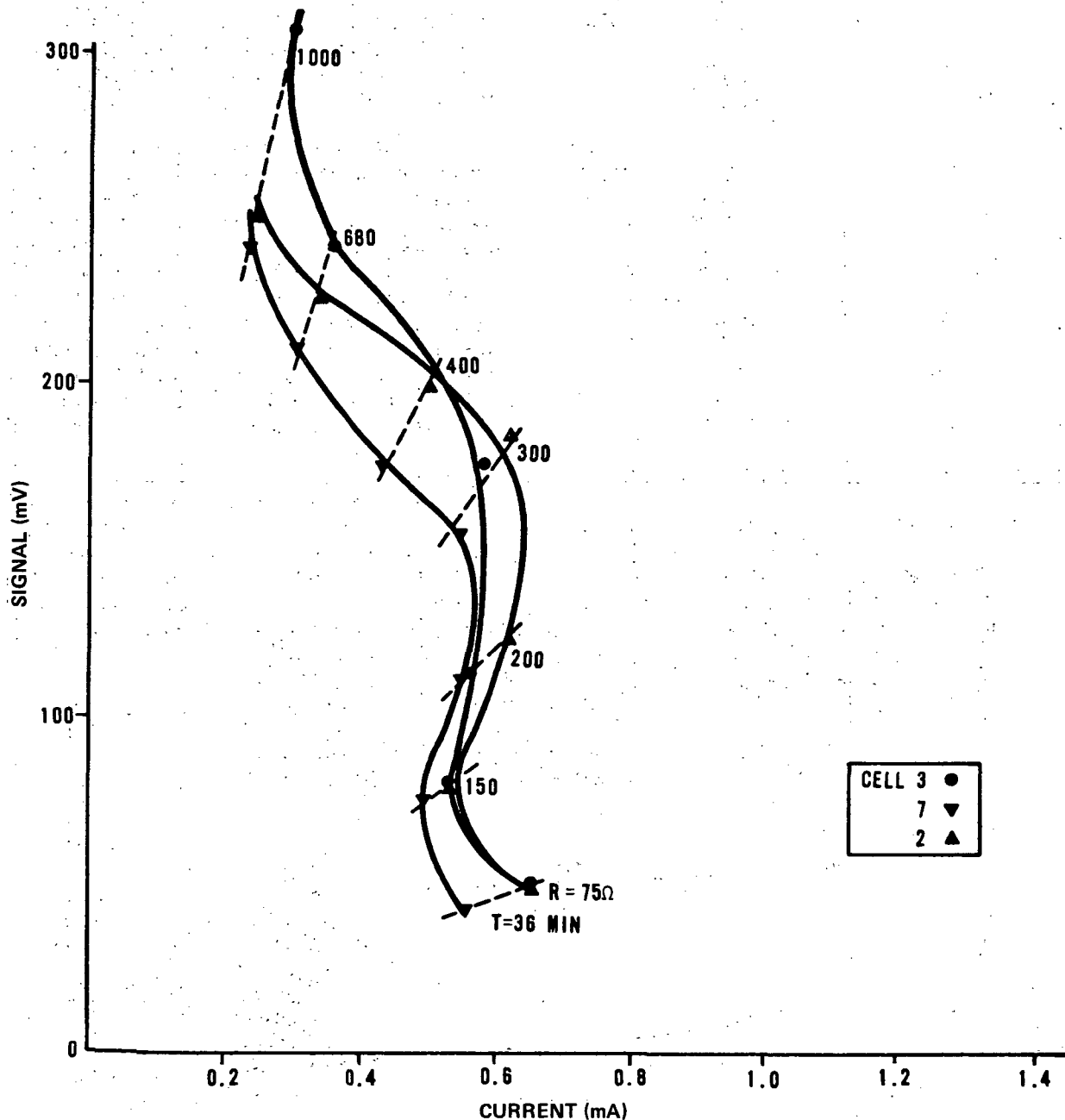


Figure 22. Internal resistance characteristics for three cells at a particular state-of-charge (AB12 cells).

The ATM test cycle used was previously shown in Figure 15.

In general, battery capacity characteristics were determined by two considerations, the response to temperature under long term cycling and the possible capacity recovery techniques once degradation has occurred.

Cyclic capacity characteristics at various temperature conditions of the three ATM flight-type test batteries (AB12 cells) are shown in Figure 23. The 20° C and 30° C curves depict the expected performance of a battery that is subjected to continuous cycling at the indicated temperature. In this respect, the curves reflect worst-case battery performance at the respective temperature.

TABLE 2. ABSOLUTE BATTERY CAPACITY

Cycle	Temperature, ° C	Capacity
1	20	26
2	0	25
3	40	24
4	10	25
5	30	25
6	15	27
7	35	28
8	25	27
9	5	25

Although the 0° C curve reflects primarily 0° C data, the curve also reflects battery performance when the battery is subjected to temperature ranging between 0° C and 40° C. The test sequence consisted of 4 days cycling at 0° C followed by 4 days cycling at a high temperature, which was followed

by at least another 4 days of 0° C cycling. As shown in Figure 23, the average capacity degradation was not greatly affected by the high temperature runs.

The capacity degradation of a battery imposes limitations on mission objectives. Capacity degradation can be defined as the loss of battery capacity within usable voltage limits. The total battery design capacity is always available, but after the onset of memory much of it is below usable voltage levels. Part of the capacity degradation test program was to determine if a capacity recovery technique could be devised that would effectively recover any or all of the available battery capacity below usable voltage levels. For test purposes, the usable voltage was 1 V or above on the first cell.

It has been theorized that the useful battery capacity is a function of the battery discharge rate. The theory was tested by subjecting a rated 20-A-h AB09 battery, which had a useful capacity of 14.4-A-h, to a series of sequential capacity tests. Each capacity test was preceded by 50 simulated ATM cycles and was conducted at different discharge rates. The

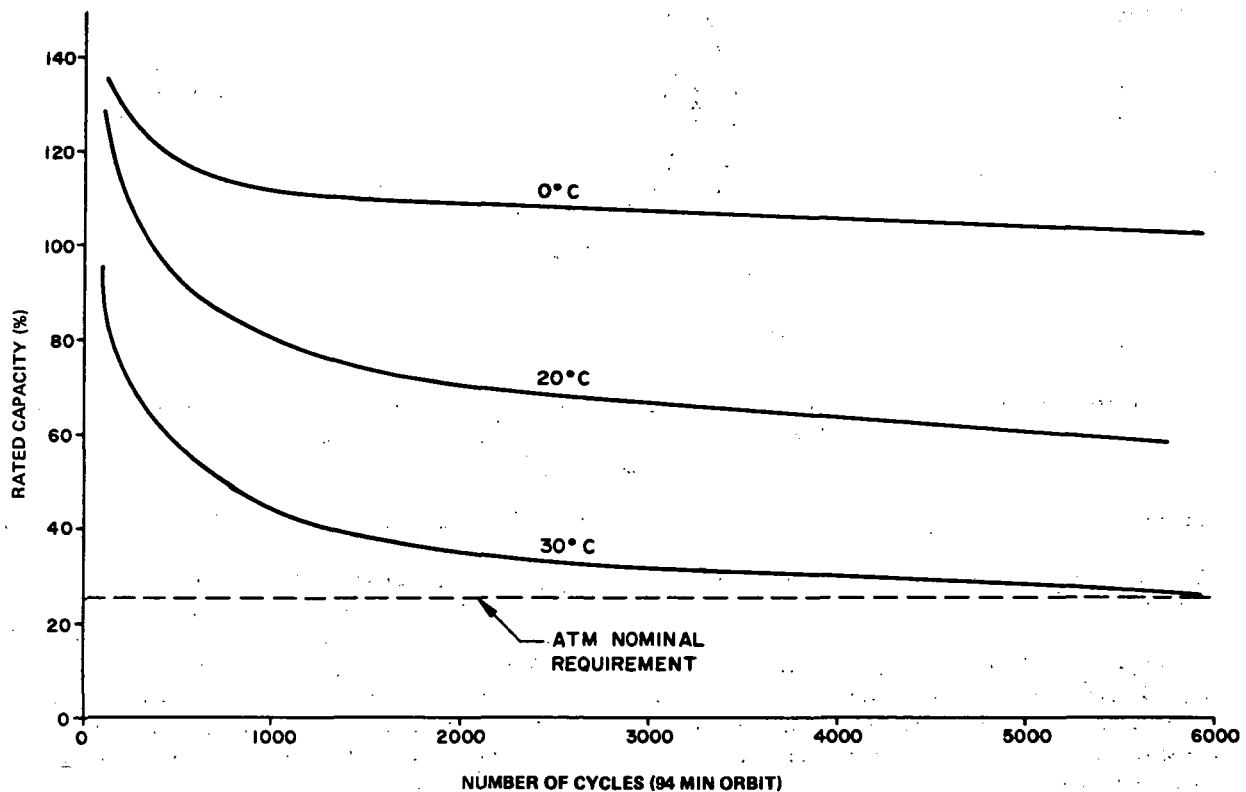


Figure 23. Expected performance of ATM Ni-Cd batteries.

results of this test illustrated in Figure 24 did not validate the aforementioned theory. The 2-A-h difference shown in the figure is attributed to instrumentation error.

A technique that can be used effectively to partially recover useful battery capacity is a decrease in cyclic operating temperature to 0° C or less. This technique is demonstrated in Figures 25 and 26. Figure 25 depicts a partial useful capacity recovery at cycle 1400 and cycle 2550; Figure 26 depicts a partial useful capacity recovery at cycle 4400. In all three situations, recovery was achieved in approximately 400 continuous simulated ATM cycles at 0° C, and the amount of recovery was approximately 7 A-h.

Another recovery technique that has achieved success is a complete battery discharge such as shown in Figure 27. The indicated strapout for the

battery was approximately 2 months. However, a 72-h strapout is sufficient to achieve a similar recovery. What the strapout essentially does is to make available capacity that is below usable voltage levels. The limitation of this recovery technique is that individual cell short circuits are required because of cell inequalities. The inequalities would cause a cell voltage reversal and possible cell failure if a battery short circuit were used instead of an individual cell short circuit.

A capacity recovery technique that could be applied easily in space but that has limited effectiveness is the trickle charge. Figure 28 shows the test results of two trickle charge tests. The first test was conducted at cycle 1000 at a 2-A rate, and the second test was performed at cycle 1310 at a 1.5-A rate. The increase in useful battery capacity for both tests was approximately 1.0 A-h.

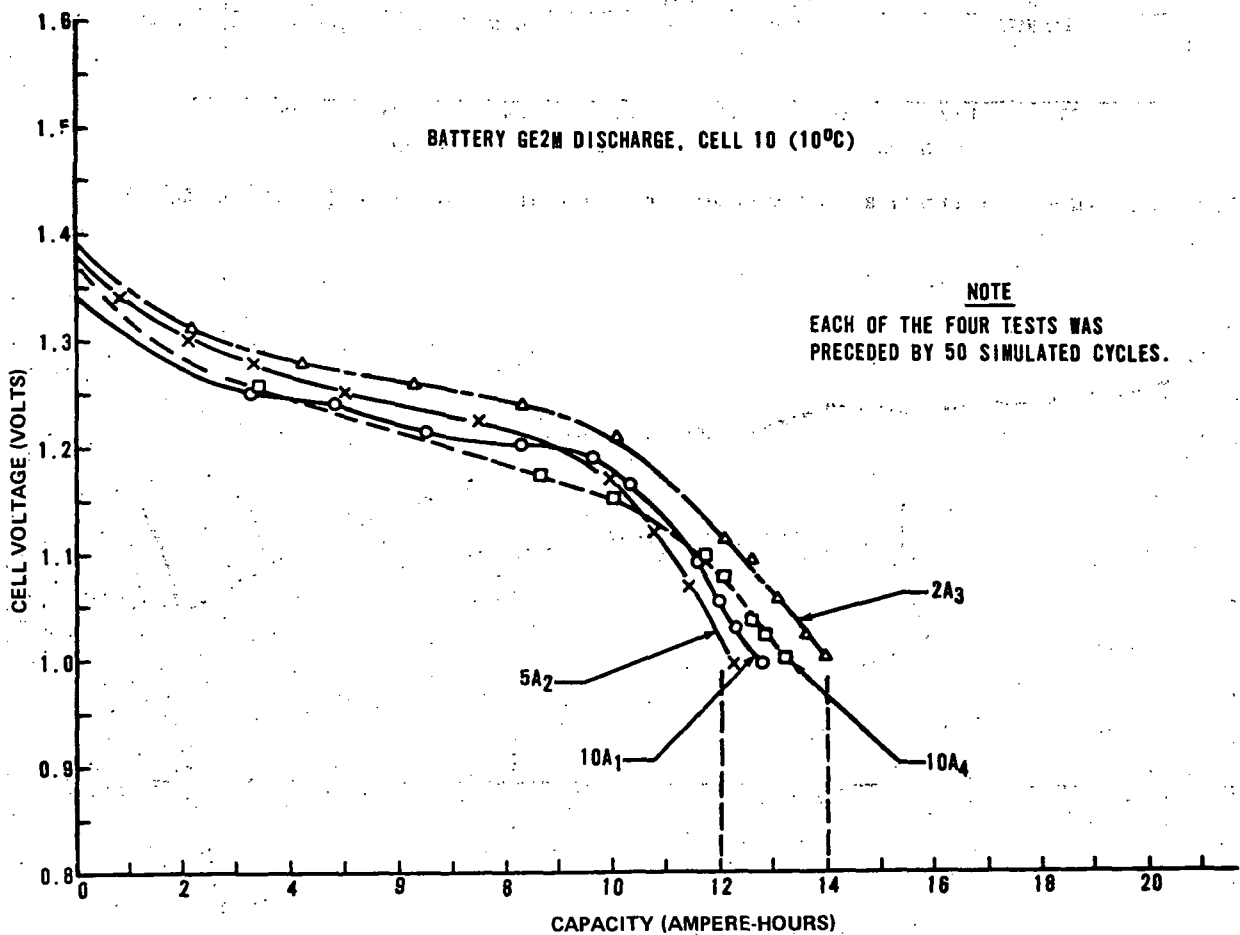


Figure 24. Battery capacity as a function of discharge rates — AB09 battery.

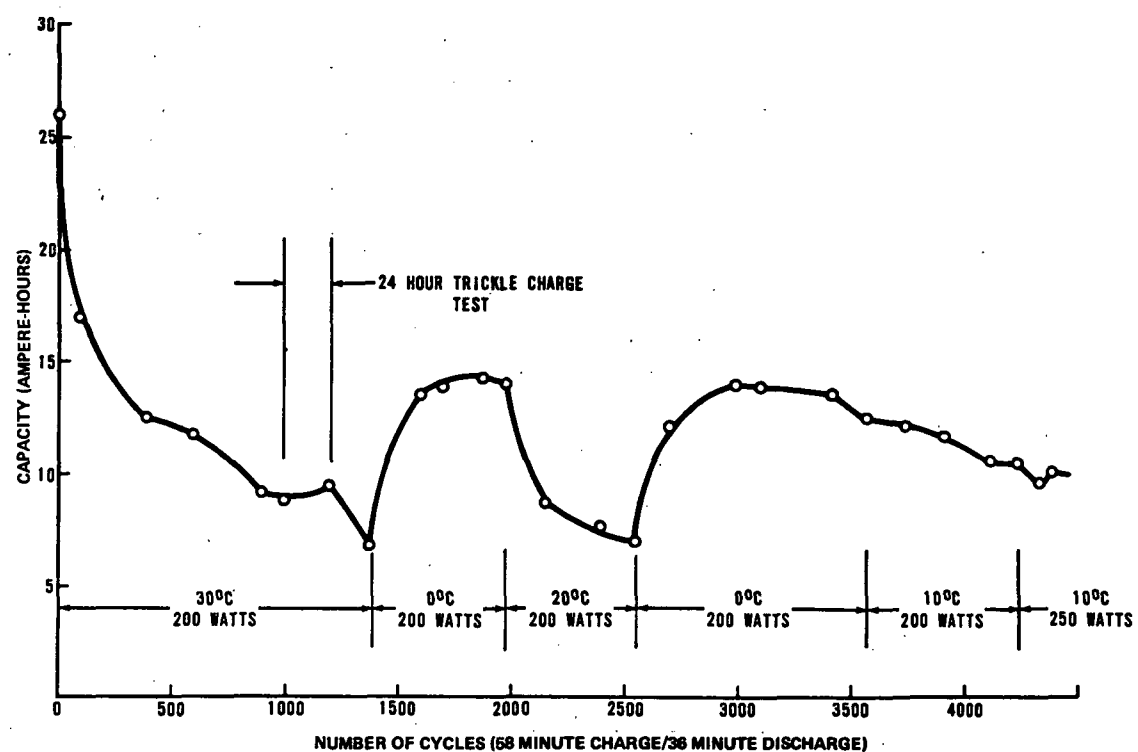


Figure 25. Battery capacity as a function of temperature — AB12 battery (0, 10, 20, and 30° C).

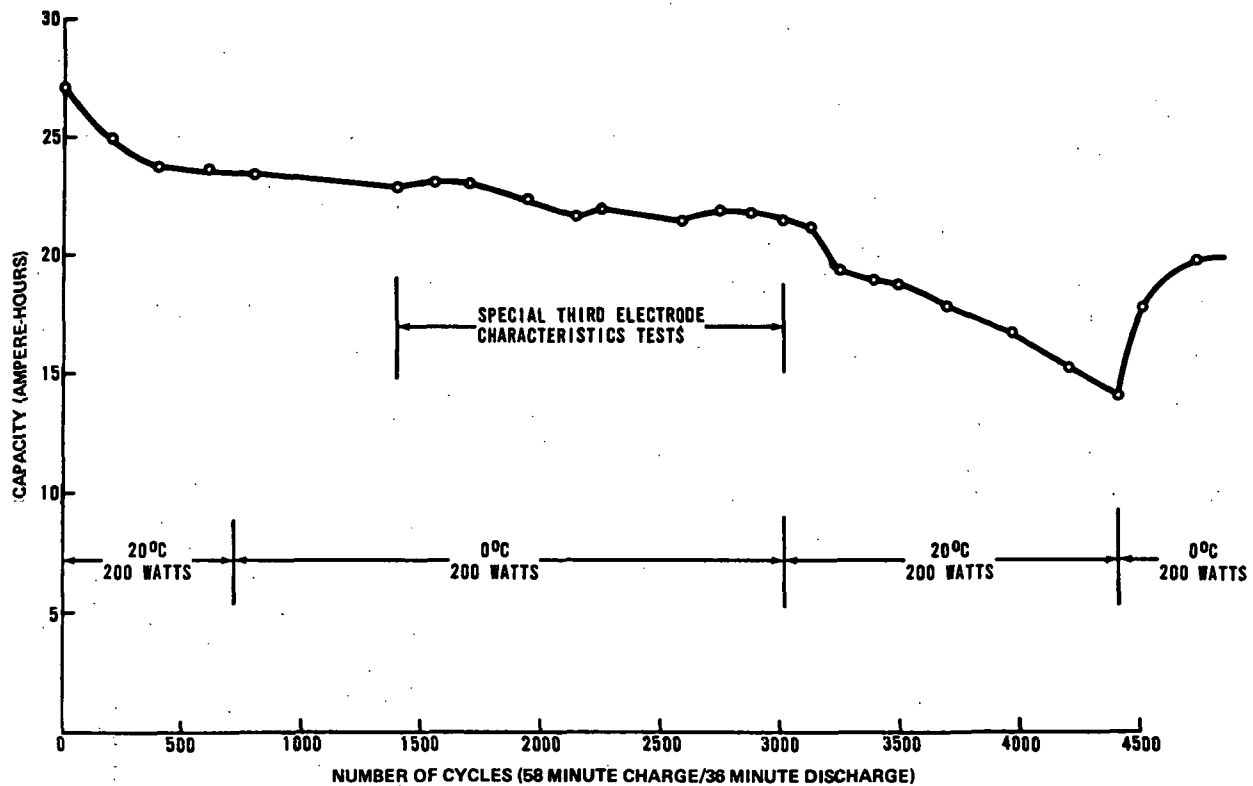


Figure 26. Battery capacity as a function of temperature — AB12 battery (0 and 20° C).

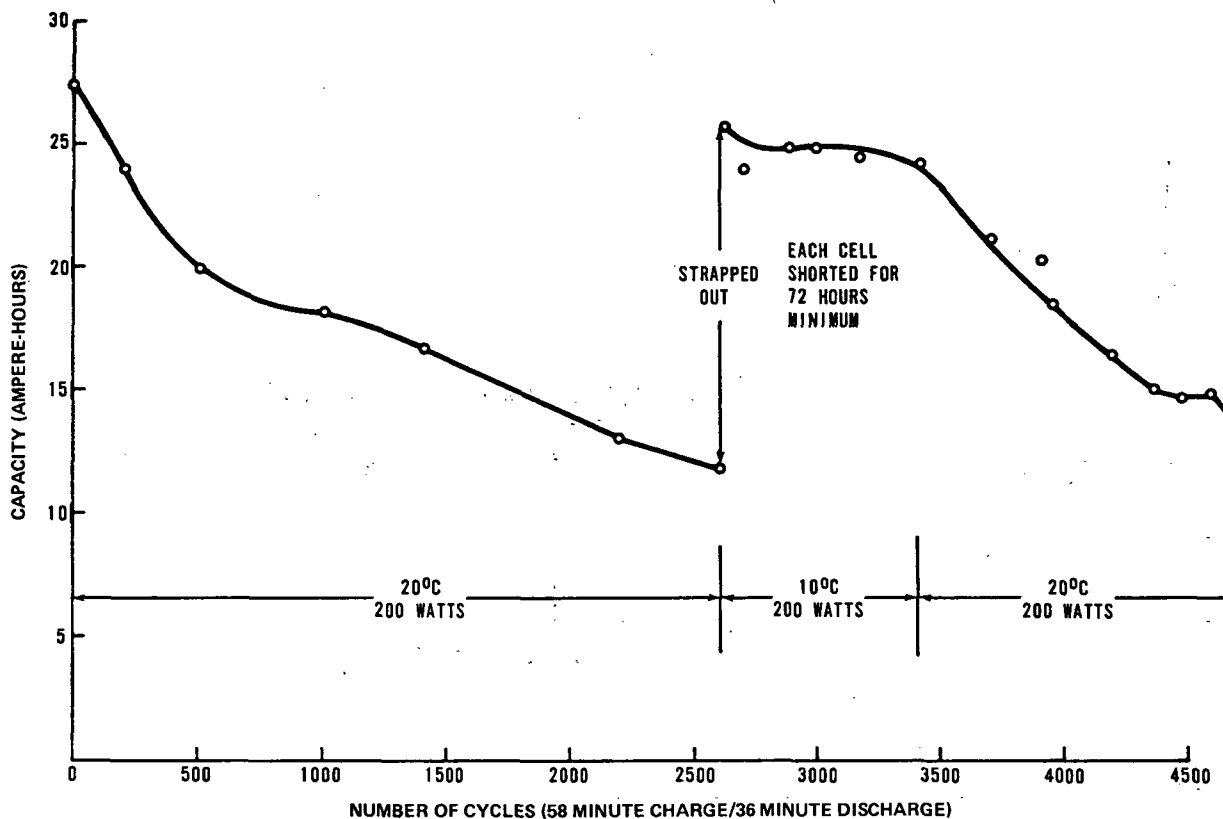


Figure 27. Battery capacity recovery as a result of complete battery discharge -- AB12 battery.

CONCLUSIONS

Based on the tests performed on the ATM cells, the conclusions reached are as follows:

1. The AB12 batteries are capable of cycling in space under the ATM orbital period for 8 months or 5000 cycles.
2. Loads of 200 W average causing a 25-percent DOD on the battery can be supplied. Short term excursions to cover rendezvous and earth resource operations can be accomplished.
3. The batteries are capable of operating in a 0° C to 30° C environment. Actual operations are expected to be on the order of 20° C or under.

Specific areas of investigation have determined effective and optimum charge control parameters. The results of these investigations are noted in the following:

Maximum cell voltage of the Ni-Cd batteries is limited by the hydrogen evolution potential, which is reported to be 1.47 to 1.55 V. On a battery basis, the maximum voltage is limited by the cell that contains the minimum capacity because this cell will be the first to reach the individual cell voltage limit. Maximum cell voltage or battery voltage is also temperature dependent. Typical maximum voltage values based on a 24-cell battery are 36.8 V at -10° C, 36 V at 10° C, and 35.6 V at 30° C. The use of the maximum voltage level as a battery charging limit appears to delay the onset of the memory phenomenon.

Charge acceptance in an Ni-Cd battery is most efficient at a 2C charge rate, but there are temperature limits. During low temperature operation, a high charge rate will cause internal cell hydrogen evolution. Quantitative values on the low temperature operation have yet to be determined. A charge rate of 0.75C has resulted in no observed cell or battery operating anomalies from temperatures of -20° C to 40° C. Single cell thermal tests provide a

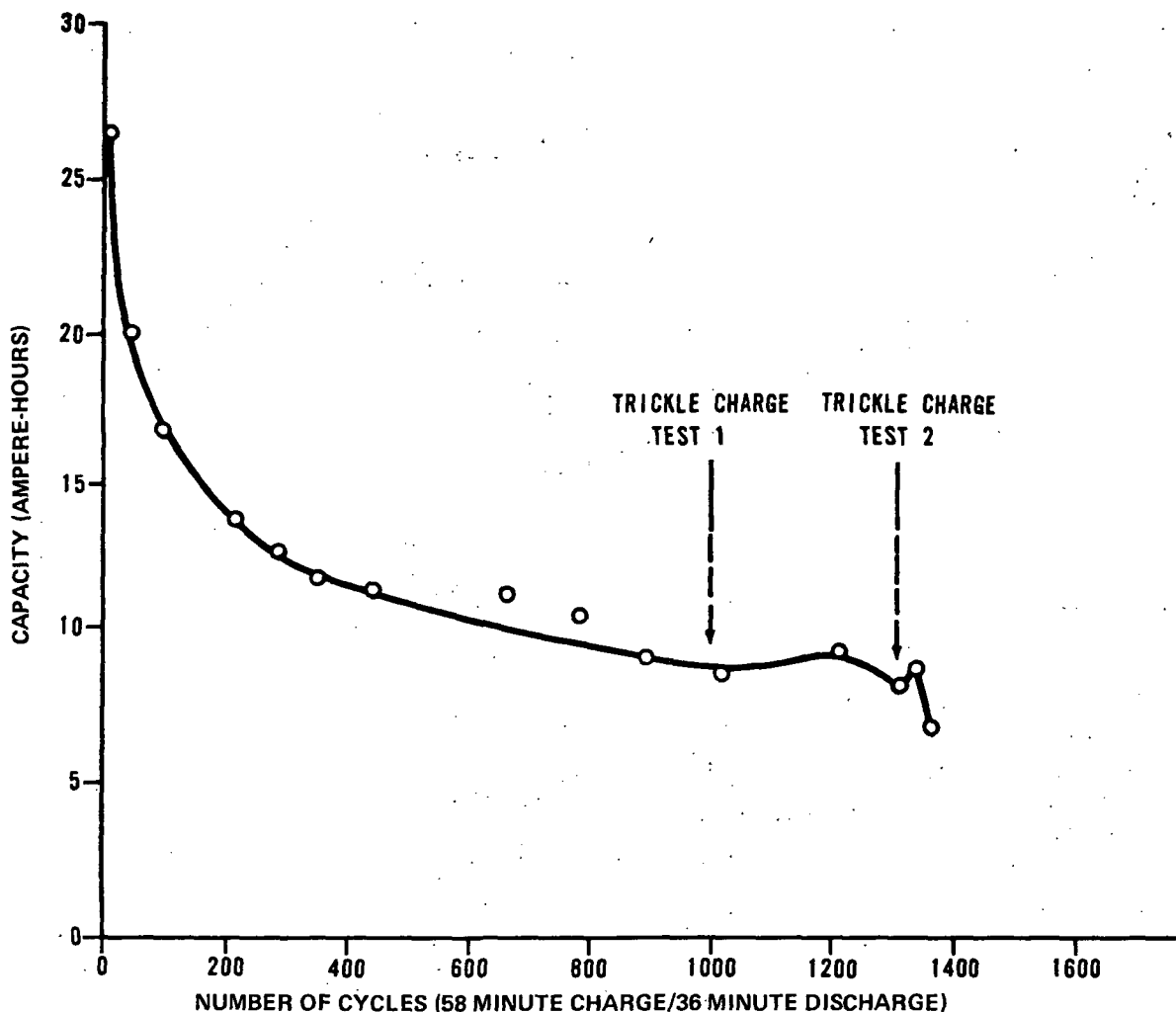


Figure 28. Battery capacity recovery as a result of trickle charge tests.

simple method of measuring instantaneous efficiency. The data obtained have been used to produce a thermal modeling program for the ATM.

Recharge requirements for 20-A-h Ni-Cd cells have been empirically determined for loads ranging from 100 W to 300 W and from -10° C to 30° C. These recharge values are a considerable improvement in the state-of-the-art. At 20° C with a 200-W electrical load, the battery recharge was decreased from 120 to 107 percent, while the battery efficiency was increased from 73 to 80 percent. Under these conditions, the heat generated per cycle has been decreased from approximately 28 W to 17 W.

The third-electrode signal characteristics tests resulted in the determination of internal third-electrode resistance, temperature response, and

nonuniformity of cell response when the cells were subjected to identical cyclic operations. When the third-electrode signal source is assumed to be a constant, then the internal resistance becomes a function of the external load resistance. Maximum internal resistance occurs when the external load is between 150 and 300 Ω. At maximum internal resistance, the third-electrode signal approaches constant current source. In the final flight battery assembly, the constant current characteristics can be used to facilitate the selection of charge-termination control signals.

The usable capacity of a battery is a variable quantity that decreases as a function of battery cyclic history, operating control temperature, and charge/discharge control parameters. Capacity degradation, which is considered a memory

phenomenon, can be delayed and under certain conditions reversed. A delay is achieved by charging all cells to their maximum allowable levels at 15° C or less. This is easily attained when the individual cell capacities are equal or matched. Once memory has developed, a complete capacity recovery can be obtained by discharging the battery and shorting each cell for a minimum of 72 hours. Normal battery cycling can be resumed after the strapout. A partial, approximately 7 A-h, battery capacity recovery can be achieved by subjecting the battery to 0° C cyclic operation, if the memory has developed during 15° C or high temperature operation.

RECOMMENDATIONS

The recording and analysis of test data in most test programs generally uncover several additional problem areas for each problem resolved. The Ni-Cd battery testing established many of the battery operating characteristics but it also indicated the need for additional specific data in several areas.

Maximum battery voltage is primarily limited by the evolution of hydrogen, which occurs somewhere between 1.47 and 1.55 V. A specific voltage value, as a function of temperature and charge rate, would be very desirable. If, as is likely, the value is a statistical quantity, then statistical variance should be determined and possibly the cell construction variations that cause the voltage variations from cell to cell should be determined.

Charge termination control data provided by the third-electrode signal also require additional quantifying. Specifically, cell third-electrode signals as a function of internal pressure and thermal characteristics must be acquired. Statistical data with a high variance would point out the need for improved manufacturing and quality control techniques. Internal cell pressure values would also provide information and data on cell operating techniques. An important factor, especially if the useful battery cyclic life is extended, is the degradation characteristics of the third-electrode signals. Proper battery recharge might not be achievable after extreme cyclic operation, if excessive third-electrode degradation occurs.

One of the most discernible battery characteristics, yet the most difficult to control, is the capacity degradation. The solution to the problem must be approached from two sides; manufacturing techniques such as chemical additives or improved plating and operating techniques such as improved charging and discharging methods. An additional capacity degradation control technique that requires further investigation is cell matching. This approach is particularly applicable to an optimal operating procedure.

Future mission applications of secondary Ni-Cd batteries will be considerably assisted by acquisition of more specific data on operating characteristics of Ni-Cd cells as outlined in the test recommendations. These recommendations would assist power system designers in optimizing secondary battery applications.

REFERENCE

1. Carson, W. N., Jr.: A Study of Nickel-Cadmium Spacecraft Batteries. NASA CR-62029, April 1966.

LOAD SHARING BETWEEN PARALLEL OPERATING DC POWER MODULES

By

Robert Kapustka

SUMMARY

Electrical load sharing between dc power modules operating in parallel has received considerable attention for application in large space electrical power systems. Various approaches will be discussed with emphasis on the solution used for the Apollo Telescope Mount (ATM) electrical power system.

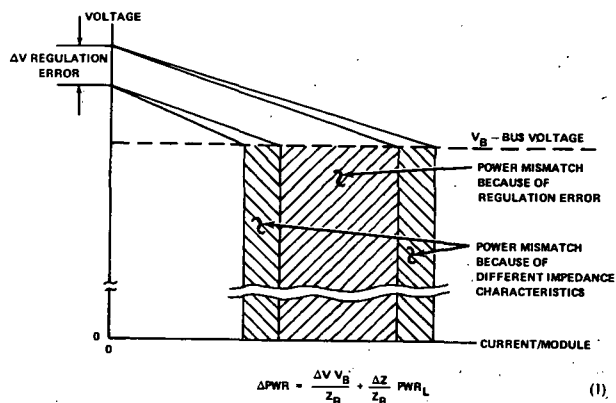
INTRODUCTION

The requirements for high reliability and easy maintenance of large space power systems indicate that modular power conversion is a desirable approach. One of the problems associated with paralleling dc power modules is load sharing among the modules; comparatively small variations in regulator output voltage characteristics reflect themselves as large differences in power outputs. This applies unbalanced stresses on the regulators and if the primary source is also modularized, as on Skylab for example, utilization of the primary source to its full capacity is degraded.

PROBLEM DEFINITION

The mismatch in the power delivered to a collection bus by any two modules is equal to the voltage at the collection bus multiplied by the differences in output currents. This is represented graphically in Figure 1. By plotting two pairs of output characteristics, one using the maximum regulation error with an average impedance and the other including maximum variation in impedance, the impact of regulation error and impedance differences can be separately identified.

Equation (1), derived from the graph in Figure 1, also defines mismatch in delivered power. The terms "bus voltage" and "average power to the load" are usually defined by system criteria. The remaining terms "regulation error," "impedance differences," and "average impedance" can be manipulated to reduce power unbalance.



where

ΔPWR = maximum possible power mismatch between any two regulators,

ΔV = maximum possible difference in the open circuit voltage of any two regulators,

V_B = voltage at collection bus,

Z_R = impedance an average regulator will present to the bus, including line impedance,

ΔZ = maximum possible difference in the impedance of any two regulators,

and

PWR_L = average power per regulator delivered to the bus.

Figure 1. Power unbalance from variation in regulator output characteristics.

TYPICAL SOLUTIONS

As shown in Table 1, there are several methods available for implementing power sharing. Increasing and matching the resistance in the distribution lines reduces both terms of equation (1). However, if the regulation error is not reasonably low, the required increase in average line resistance can involve significant power losses in the lines and also give a high impedance or "soft" regulated bus. Programming the regulator to present a certain impedance at its terminals will eliminate the extra line losses but may still result in a soft bus. A system with remote sensing to program impedance at the bus is capable of a lower impedance or "hard" bus because the second term of equation (1) is reduced.

significantly as a result of the remote sensing compensation for line impedance variations. However, it is evident that any decrease in average impedance must be accompanied by a corresponding decrease in regulation error to maintain the first term at a low value.

TABLE 1. METHODS OF POWER SHARING

METHOD	ADVANTAGES	DISADVANTAGES
UTILIZE RESISTANCE IN DISTRIBUTION LINES	• SIMPLE • RELIABLE	• EXTRA WEIGHT • RESISTANCE REQUIRED TO ACCOMPLISH SHARING MAY INVOLVE SIGNIFICANT DISTRIBUTION LOSSES • "SOFT" REGULATED BUS
PROGRAMMED REGULATOR IMPEDANCE CHARACTERISTICS	• RETAINS CHARACTERISTICS OF LINE RESISTANCE WITHOUT ASSOCIATED POWER LOSS	• COMPLEX • "SOFT" REGULATED BUS
REMOTE SENSING TO DETERMINE REMOTE PROGRAMMED IMPEDANCE	• CAPABLE OF "HARD" REGULATED BUS	• COMPLEX • REQUIRES ACCURATE AND STABLE CONTROL CIRCUITRY TO SHARE TO "HARD" BUS
MASTER-SLAVE SYSTEM	• CAPABLE OF "HARD" REGULATED BUS	• COMPLEX • MASTER MODULE BECOMES SYSTEM CRITICAL
PERIODIC MANUAL ADJUSTMENT	• FLEXIBILITY	• REQUIRES MAN-INTERFACE

A master-slave arrangement, where all modules are programmed to duplicate the output current of a master module, is also capable of a hard bus. The current tracking of the slave modules is not required to be as accurate as the voltage regulation that would accomplish the same sharing. A given percent error in current tracking will result in that same percent error in power sharing; a given percent error in voltage regulation will be multiplied by the inverse of the regulator impedance. Thus, with low output impedances, small regulation errors will be amplified into a relatively large power unbalance.

Periodic manual adjustment can add considerable flexibility to any method of power sharing, although it requires the capability for a man interface. This feature allows more variables to be taken into consideration when determining what fraction of the load should be supplied by a particular regulator.

LOAD SHARING ON THE ATM

The method chosen for use on the Skylab/ATM power system is a hybrid of the remote-programmed impedance and master-slave systems. Figure 2 is a simplified feedback diagram for implementing the remote-programmed impedance. The bus voltage is sensed, and the error signal is used to determine the regulator output current. This dependence of output current on bus voltage generates a resistance characteristic, and with sufficient loop gain, compensation can be made for the impedance in the distribution line so that it does not affect the net impedance presented to the bus.

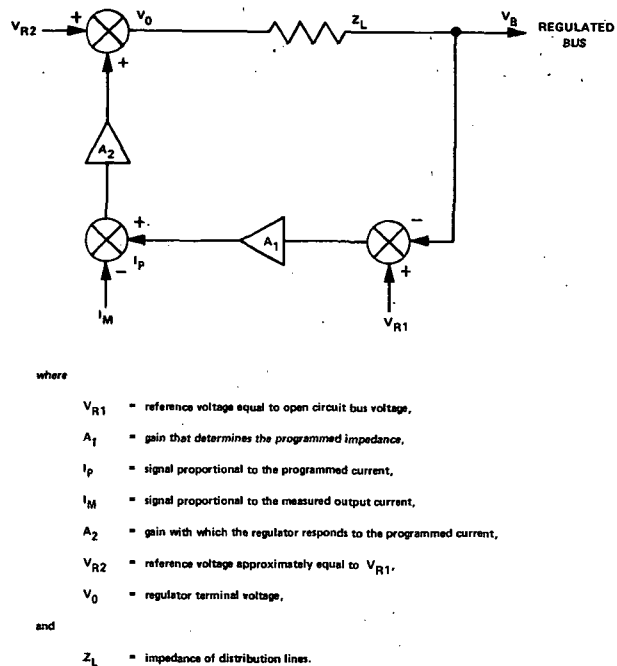


Figure 2. Simplified feedback diagram for remote sensing and programmed impedance.

The equation describing the loop can be reduced as shown in Table 2. Implementing the inequalities as shown will eliminate power mismatch because of different line impedances and will program the system for a hard bus. By examining equation (3), it can be seen that there are still sources of unbalance remaining. Variations in the V_{R1} associated with each feedback loop are equivalent to regulation errors, as is an error in offset when measuring regulator output current I_M , although the effect of any error in offset of I_M is reduced by the factor $1/A_1$; variations in the gain A_1 and the gain of the circuit measuring I_M are equivalent to impedance differences.

TABLE 2. REDUCTION OF FEEDBACK EQUATION

$V_B = \left(\frac{1}{1+A_1 A_2} \right) V_{R2} + \left(\frac{A_1 A_2}{1+A_1 A_2} \right) V_{R1} - \left(\frac{A_2 + R_L}{1+A_1 A_2} \right) I_M$	(2)
MINIMIZE EFFECTS OF VARIATIONS IN LINE RESISTANCE (R_L)	$\Rightarrow A_2 \gg R_L$
MINIMIZE EFFECTS OF VARIATIONS IN A_2 ITSELF	$\Rightarrow A_2 > 1$
PROGRAM IMPEDANCE FOR "HARD" BUS	$\Rightarrow A_1 > > 1$
THEREFORE: $\frac{1}{1+A_1 A_2} \ll 1; \frac{A_1 A_2}{1+A_1 A_2} \approx 1; \frac{A_2 + R_L}{1+A_1 A_2} \approx \frac{1}{A_1}$	
THEREFORE: $V_B \approx V_{R1} - \frac{1}{A_1} I_M$	(3)

Since the output of each regulator must be measured separately, the only way to reduce the effects of variations in the measuring circuit of I_M is to improve the accuracy of the circuit itself.

The reference voltage V_{R1} and the gain A_1 should be exactly the same in each feedback loop. The simplest way to accomplish this is to use only one circuit to generate the signal I_P and then distribute this signal to all the regulators. Thus, any drift in V_{R1} and

A_1 will be reflected by identical changes in all regulators and power sharing will not be affected. This eliminates the need for extreme stability in V_{R1} and A_1 .

Localizing as many parts of the individual feedback loops as possible has the advantages of the master-slave system but also has the corresponding disadvantage of the localized portion being system critical. In a normal master-slave system, however, an entire power regulator will be system critical whereas only one amplifier is critical in the Skylab/ATM system and redundant amplifiers are provided.

FUTURE CONSIDERATIONS

The basic feedback loop shown in Figure 2 also is capable of directly controlling variables other than output current. By replacing the input I_M with the appropriate signal, the circuit could control, for example, output power, input current, or input power. This would still retain the feature of a programmed bus impedance but the parameter to be equalized would not have to be output current.

Page intentionally left blank

MICROWAVE POWER TRANSMISSION CONSIDERATIONS FOR EARTH ORBITAL SPACE MISSIONS

By

W. J. Robinson, Jr.

An investigation was begun in May 1967 to determine ways of transferring electrical power in space other than via hard wire transmission lines (Fig. 1). This investigation revealed that the use of microwaves was feasible and that the microwaves would perform more efficiently than expected. It was also concluded that the use of a laser to transfer electrical power appeared promising.

Electrical power transfer has been demonstrated at Raytheon on two previous occasions; 102 W had been transferred over a distance of 5 m in 1963 and in October 1964 a helicopter requiring 280 W remained at 15 m altitude for 10 hr. The feasibility had been demonstrated, but an overall efficiency had not been demonstrated. It became an elusive value to establish. Microwave technology was well



Figure 1. Transfer of electrical power in space.

advanced in many applications such as radar, data transmission, and TV. Thus components for generating high powers were well advanced as compared to the development of laser components. The laser principle had only been discovered a few years earlier, and the recent CO₂ laser was quite large and developed only about 10 kW as compared to hundreds of kW developed by microwave components. Detectors for converting the laser energy to dc are in the early research phase; however, laser technology offers a promising possibility because of the smaller beam width that can be developed for power transmission. Therefore laser detector development should be pursued vigorously.

The results of our investigation led us to consider microwaves as a means of transferring electrical energy between earth orbital satellites in the late seventies or early eighties.

The components that are needed for a microwave system are a power supply, a transmitter, a transmitting antenna, a beam, and a receiving antenna as shown in Figure 2. The power supply, microwave generator, and antenna devices are devices that have been developed over a number of years and that can, with slight modifications, be used for power transfer at relatively high efficiencies. The transmitting antennas that have been designed for radar, TV, data transmission, etc., produce divergent beams and therefore are of no use in this application. However, new types, such as phased arrays and gaussian beams, that have been developed recently show promise for use in microwave power transmission.

As a result of an earlier effort by Professor George at Purdue University and Mr. William Brown at Raytheon, a comparison of the power output and the efficiency of microwave rectifiers is presented in Table 1. The device from Table 1 that promised the highest efficiency is the point contact semiconductor. The special advantages of the point contact semiconductor are an ability to operate continuously, an impedance compatible with that of electric motors, and a high power handling capability in relation to its weight. These are easily combined to form modules that handle a considerable amount of microwave power. Mr. Brown discovered that by combining the receiving antenna with the point contact semiconductors to form a "rectenna," the device collects as well as rectifies the microwave energy. The rectenna possesses the following desirable characteristics: (1) the energy is captured and rectified at a high overall efficiency of 70 percent or better, (2) the large aperture is comparatively nondirective so that it does not have to be pointed accurately in the direction of the transmitting antenna, and (3) the device handles its own dissipation through a radiative cooling process.

An in-house hardware investigation began in the fall of 1969 with the purchase of a 5-kW CW transmitter that operates on 2.45 GHz (Fig. 3). The transmitter with its variable output capability was used to construct the receiving antenna shown in Figure 4. All the dimensions such as dipole length, spacing between dipoles, and reflector distance were determined experimentally using a diode bridge at the center of the dipole and measuring the output voltage. In some cases two and three voltages were

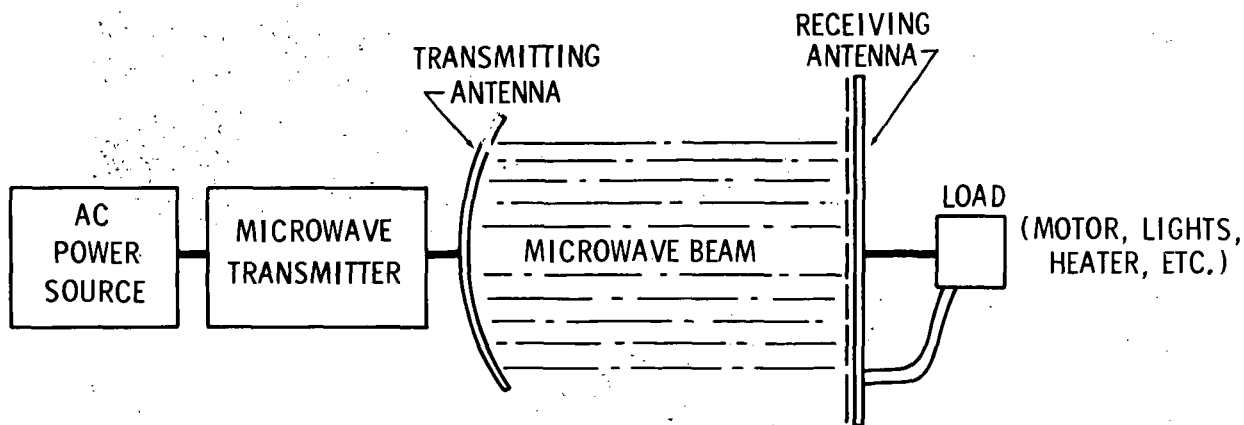


Figure 2. Components of a microwave power transmission system.

TABLE 1. COMPARISON OF POWER OUTPUT AND
EFFICIENCY OF MICROWAVE RECTIFIERS

Class	Subclass	Maximum Experimental Efficiency (Percent)	Maximum Experimental Power (W)	Frequency Band
Colinear Beam	TWT			
Colinear Beam	Klystron			
Crossed-Field	Injected Beam	42	162	S
Crossed-Field	Magnetron	22	25 000 (Peak)	L
Crossed-Field	Cyclotron	12	12 000 (Peak)	L
Diode	Multipactor			
Diode	Thermionic	55	900	S
Diode	Point Contact Semiconductor	70	0.1	S

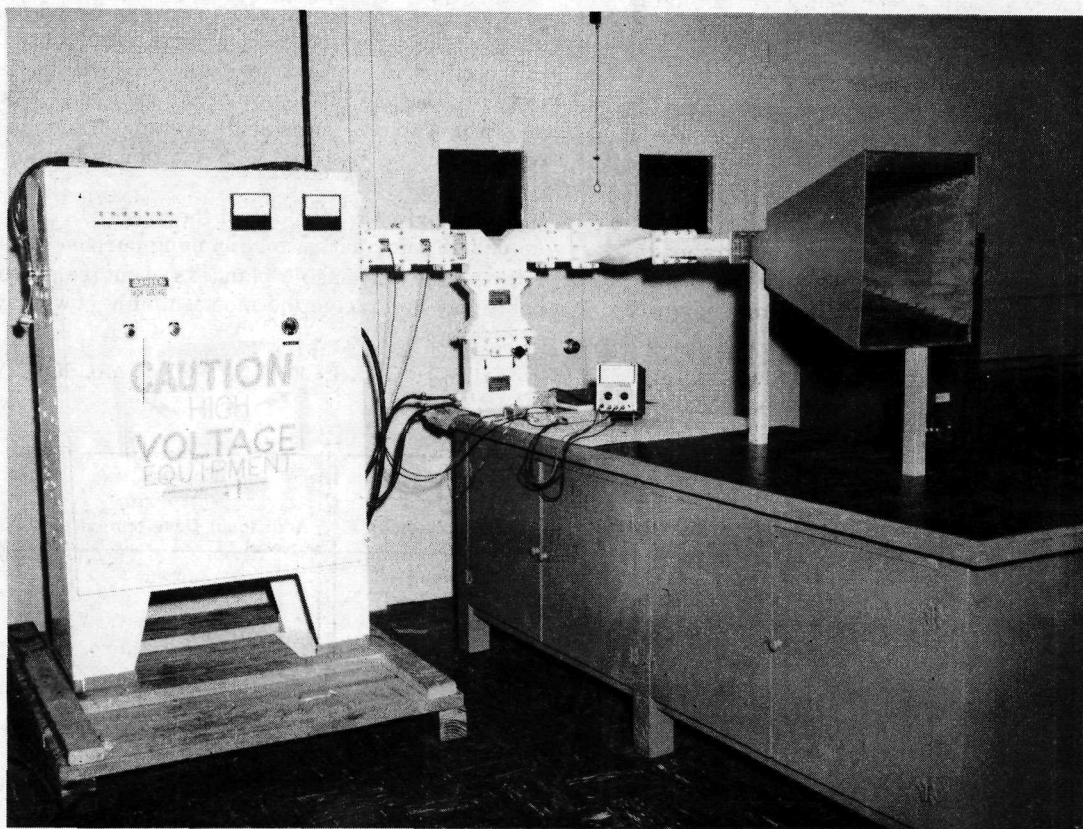


Figure 3. Microwave power supply.

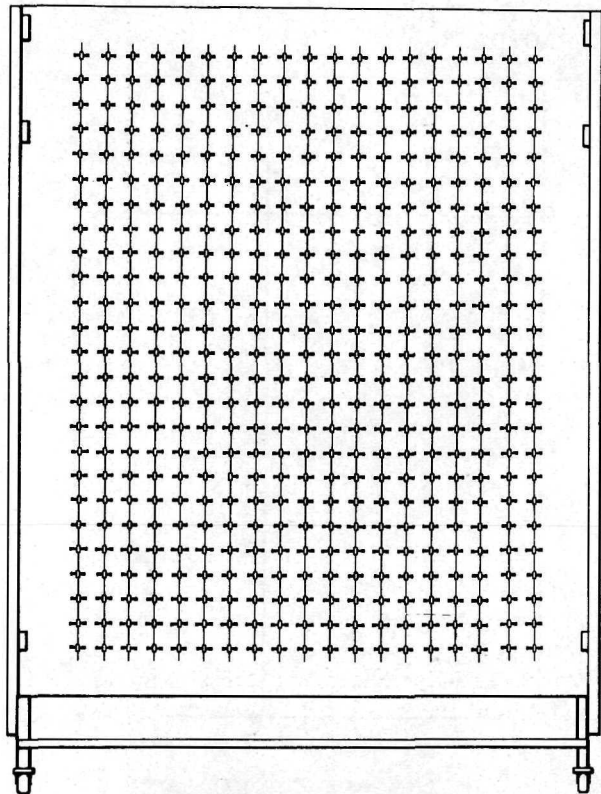


Figure 4. Microwave antenna.

necessary to determine element spacings. One of the early problems discovered was measurements that were very erratic and inconsistent; however, a check of the transmitter output power showed that it varied with line voltage changes. An accurate check on the output power changes of the transmitter was made using a string of basic elements fastened to the experimental board and a meter to monitor the power

density. The density was monitored and controlled to a specified amount at the time of each voltage measurement. When the receiving antennas are complete, all the equipment will be moved to the Astrionics Range and the measurements such as efficiency, power handling capability, and scatter will be conducted over distances of up to 200 m. Preliminary measurements at a short distance (approximately 3 m) indicate an efficiency of 40 percent from the magnetron to the load at the receiving antenna.

In December 1969 a contract was awarded to Raytheon to continue their investigations of microwave power transmission with emphasis on space application. In October 1970 a demonstration of a microwave power transmission system was made with full instrumentation. The results of those measurements are shown in Table 2. Although the measurements were made with a system using off-the-shelf items, this test established a true overall efficiency of 18.4 percent. The power supply was only 66 percent efficient, but if technology is applied in this area, an efficiency of 95 percent can be achieved easily. Also, by using better magnetic (cobalt-copper-cerium) materials, 85 percent efficiency can be achieved in the microwave generator. Based on results of efforts by Raytheon during the past year, a 56 percent efficiency can be achieved using present day technology for the rectenna. As shown in Table 2, an overall system efficiency of 67 percent can be expected with additional development.

The primary purpose of these efforts is to develop design information for planning purposes. This information will enable planners of future systems to positively determine the most suitable power system.

TABLE 2. DEMONSTRATED AND EXPECTED EFFICIENCIES OF THE ELEMENTS OF A MICROWAVE POWER TRANSMISSION SYSTEM

Component	Efficiency Demonstrated	Efficiency Expected with Present Technology	Efficiency Expected with Additional Development
Power Supply	66 percent	95 percent	97 percent
Microwave Converter	66 percent	85 percent	90 percent
Transmission			
Collection and Rectification	42.4 percent	80 } 56 percent 70 }	90 } 76.5 percent 85 }
Overall 60 Hz Input to be Output	18.4 percent	45 percent	67 percent

LARGE-AREA LUNAR SURFACE SOLAR ARRAY

By

J. L. Miller

SUMMARY

Energy requirements of 10 000 to 500 000 kW-h must be met to support a 3- to 6-man crew for up to 1 year on the lunar surface. There are essentially two feasible sources for these energy levels: (1) a nuclear source that presents increased hazards but functions continuously; and (2) a solar source that functions only during the lunar day. This paper describes a 45-kWe solar array for such a mission, and shows the design requirements and potential problem areas associated with survival in the extreme thermal environment. The paper reports on about 40 months of work performed by TRW Systems Group under contract to MSFC and references reports generated under that contract. It also describes the design, fabrication, and testing of six engineering evaluation modules and concludes by showing the design concept selected for the 1971 to 1975 time period.

PROGRAM DEFINITION

The use of solar arrays in earth orbit is routine, and the use of solar arrays in terrestrial applications is being considered seriously. Surface application of solar arrays differs from orbital application in two important respects. First, the dark-to-illuminated time ratio is much greater on the planet's surface than in orbit, and secondly, the possibility of contamination is greater on the planet's surface. The latter restriction on terrestrial array application, however, is not prevalent on the moon. With no clouds, dust storms, or precipitation, the surface of the moon seems ideal for a large-area solar array energy source. The only significant engineering constraint is the long time period of thermal excursion from -173°C at lunar night to 120°C at lunar noon. Other constraints such as those imposed by meteoroid hazards, radiation degradation, vacuum exposure, etc., are not considerably different from those in earth orbit.

To achieve thoroughness in lunar surface exploration and to promote man's capabilities to survive and work in other areas of the universe, a lunar base is essential. A logical first lunar base was defined in a NASA-funded study conducted by Chrysler Corporation Space Division [1]. This study defined a 3- to 6-man base with lunar mobile vehicles capable of 125-mile radius excursions. The expected mission duration is 1 to 5 years. Nighttime power and mobile vehicle power are supplied by hydrogen-oxygen fuel cells. A large solar array powers the base in daytime. Surplus power is used for electrolysis of the water produced by the fuel cells in the base and on the mobile vehicles. Thus, an energy depot is provided for the exchange of reactant fuels (hydrogen and oxygen) to produce water. The primary energy source must be capable of delivering an average of 45 kWe during the daylight hours to accomplish this task.

ARRAY DESIGN CONSIDERATIONS

Figure 1 shows the layout of the shelter base, electrochemical reactants production system (ERPS), and the solar array. Many tradeoffs were performed to arrive at the array design [1]. Figure 2 shows a number of the geometrical configurations considered. Of those shown here, three were felt to be worthy of detailed analysis. These were the flat laydown, lean-to, and fully oriented configurations. Consideration was given to launch package constraints, lunar surface weight for astronaut handling, and astronaut deployment and maintenance time. Energy available from any of the configurations is dependent primarily upon two major factors, the incident sunlight and the array temperature. Since the array power decreases approximately 0.5 percent per degree centigrade, it is readily apparent that power will fluctuate broadly as the array experiences the lunar surface temperature changes. Of great concern in this area is the fact that the radiative view factor of the surface array is very limited; i.e., deep space

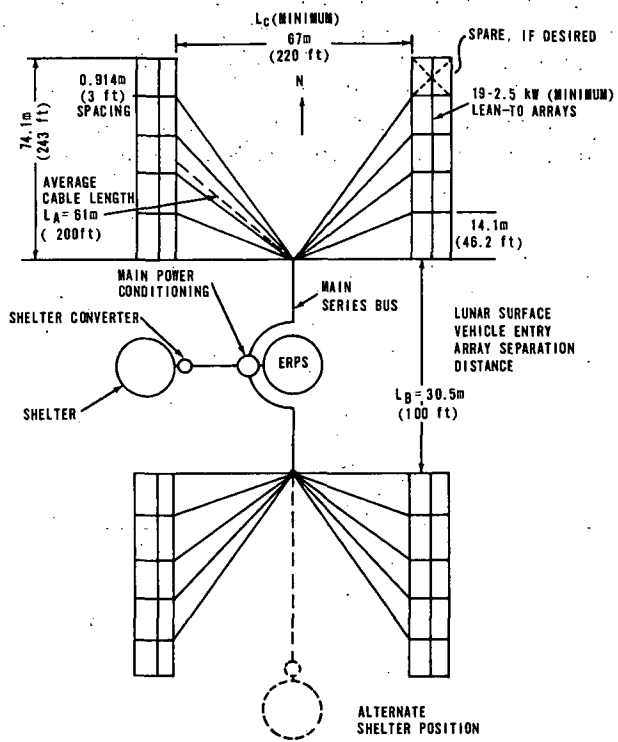


Figure 1. Schematic of an electric power system for a lunar base (47.5-kW minimum gross power).

is viewed in something less than a hemisphere. It was learned during this study that the heat burden could be greatly reduced by the use of thermal skirting. The skirts are aluminized Mylar blankets that serve as reflective surfaces around the array sections and prevent buildup of high temperatures on that portion of the lunar surface adjacent to and underneath the solar cell panels. An added benefit of the skirt blankets is that they will serve as vibration buffer pads between the solar panels during launch and landing. Activity near the deployed thermal skirts would be minimized to prevent coating the reflective surfaces with lunar dust.

Power available as a function of lunar half-day (the other half-day is the same since the lunar morning and evening are considered to be the same) is shown in Figure 3. For the same total energy, the 51-deg lean-to requires the greatest total area, 1003 m^2 ($10,800 \text{ ft}^2$). This results from its double-cosine shaped curve consisting of two contributing panels. The flat laydown configuration is next largest because of the more ineffective shape of its

TYPE	CONFIGURATION	REL. EFFECTIVENESS*	
		REL. WEIGHT	REL. AREA
1. FLAT ARRAY - FLAT ON LUNAR SURFACE	AREA A	1.0	1.0
2. TIPPED ARRAY - NORMAL TO SUN AT NOON	LATITUDE L	1.12	0.86
3. LEAN-TO ARRAY - RIGID RECTANGULAR SOLAR ARRAY		0.87	0.90
4. LEAN-TO ARRAY - FLEXIBLE RECTANGULAR SOLAR ARRAY		0.98	0.92
5. LEAN-TO ARRAY - PRESSURIZED RECTANGULAR SOLAR ARRAY		1.72	0.89
6. SPHERE - PRESSURIZED		2.22	2.22
7. FULLY ORIENTED ARRAY	*	0.71-1.38	0.55

*ARRAY TEMPERATURE EFFECTS NOT CONSIDERED

SELECTED FOR MORE DETAILED STUDY

Figure 2. Relative effectiveness of various solar array configurations.

single-cosine curve. Also, the single-cosine shape is more difficult to use because of its large excursion of available power. The oriented array naturally has the smallest area, but it requires the greatest amount of astronaut time to maintain proper orientation. The alternative is to provide an automatic sun tracker at a considerable increase in complexity and cost. With all advantages and disadvantages considered, the lean-to configuration was selected as the most advantageous primarily because of its ease of deployment, its freedom from maintenance, and the shape of its power-available curve.

Selection of array voltage was accomplished considering total system weight and performance requirements. High voltage was necessary for water electrolysis and to minimize line losses. Extremely high voltages required greater cell spacing and heavier line insulation; also, very high voltages were considered to be an astronaut safety hazard. Therefore, 300 Vdc was chosen as optimum.

Breakup of the 45-kWe solar array into 2.5-kWe units was performed for two reasons, which also

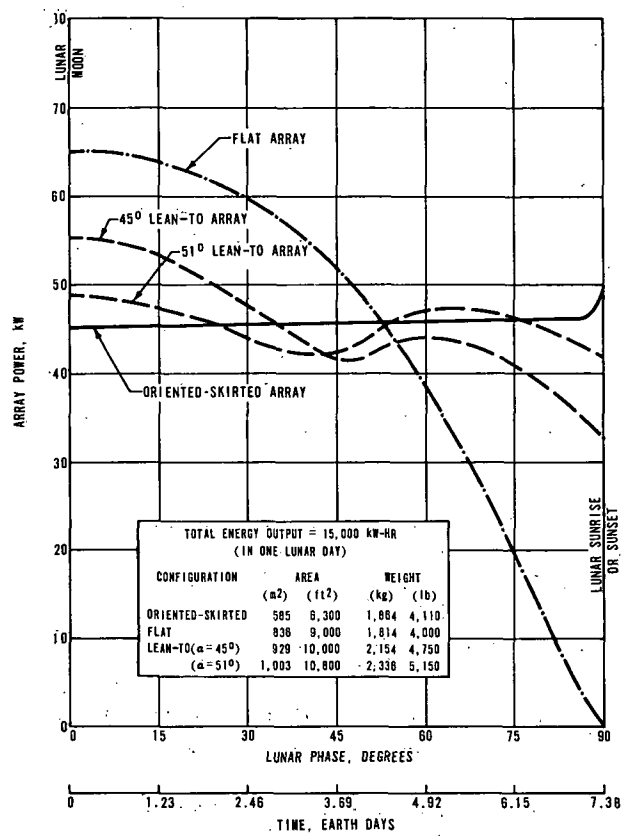


Figure 3. Comparison of solar array configurations for a constant total energy output.

determined panel size: (1) for ease in launch packaging (Fig. 4) and (2) to minimize astronaut handling time (Fig. 5). The panels are 76.2 by 122 cm (30 by 48 in.), and 20 such panels make up each side of the lean-to. The entire array consists of 18 such lean-to configurations, each redundantly wired into the central bussing system. This should provide the greatest system flexibility with maximum reliability and should require minimum astronaut time.

SUBSTRATE TRADEOFFS

In arriving at an appropriate substrate design, considerable emphasis was placed on the use of technology developed under other programs, especially those programs involving rollup arrays

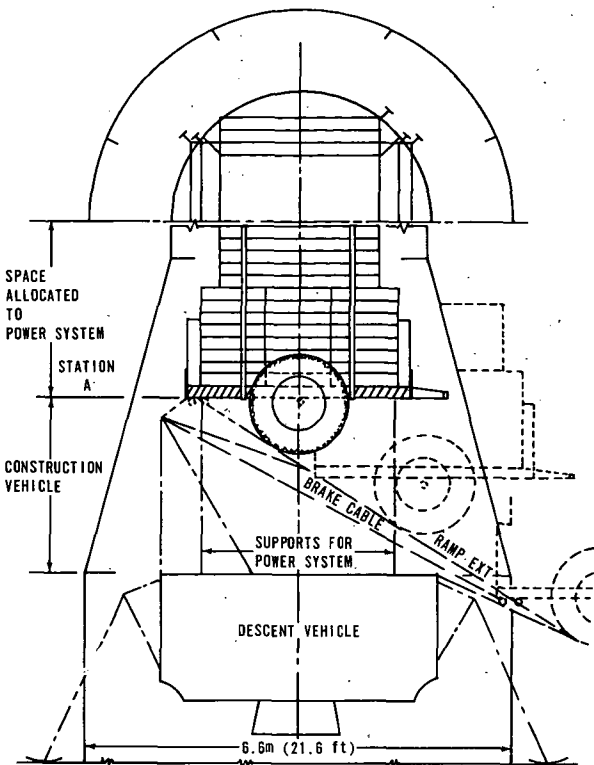


Figure 4. Stowage and unloading of foldout solar array.

and large foldout arrays. Two of the techniques chosen draw heavily from work performed for the Jet Propulsion Laboratory by Boeing and General Electric. Figure 6 shows the first of these designs, which is an aluminum box-beam frame with a fiberglass lattice diaphragm upon which the cells are installed. This design is commonly referred to as the "tennis racket" approach and uses a thin wall aluminum extrusion as the frame to support the fiberglass lattice. Since the fiberglass tapes are tensioned to about 4 kg each, the aluminum beam must have sufficient torsional strength to prevent warping and twisting under the resulting load. The 1.91- by 1.27-cm cross section with 0.063-cm thick walls provided sufficient strength; however, for the large 76- by 122-cm module, a cross member was required to brace the long dimension.

Figure 7 shows the second design approach which uses the flexible kapton technique developed for the rollup arrays. In this design the cells are bonded to

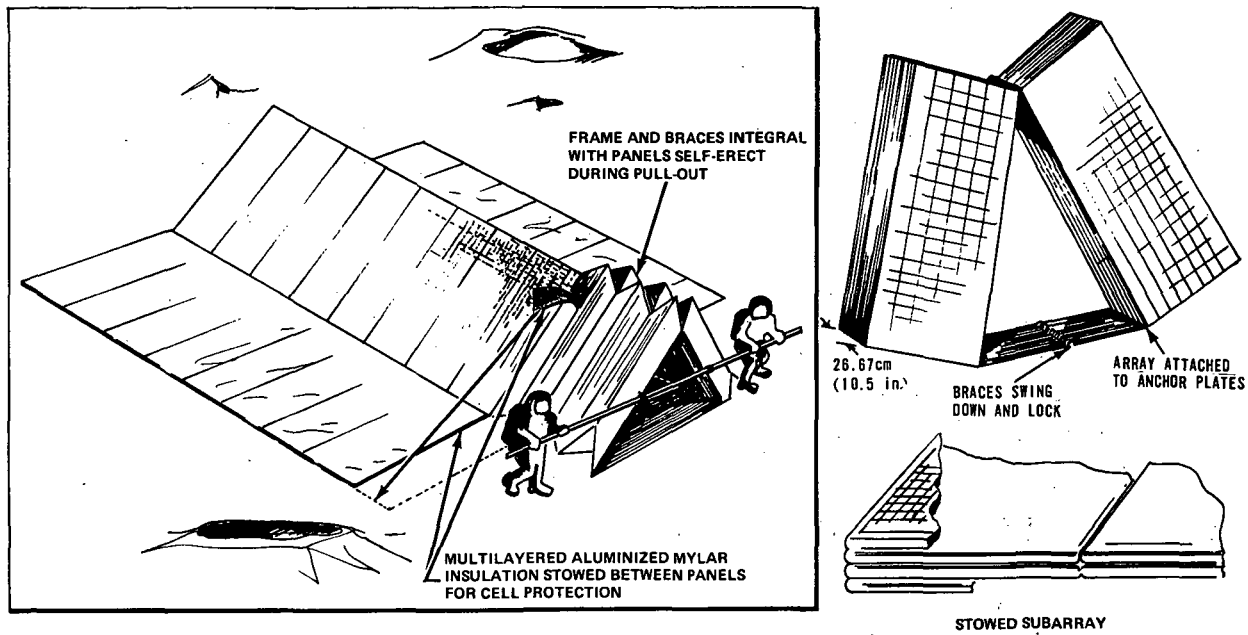


Figure 5. 2.5-kW subarray panel pullout integral mounting structure — concept III.

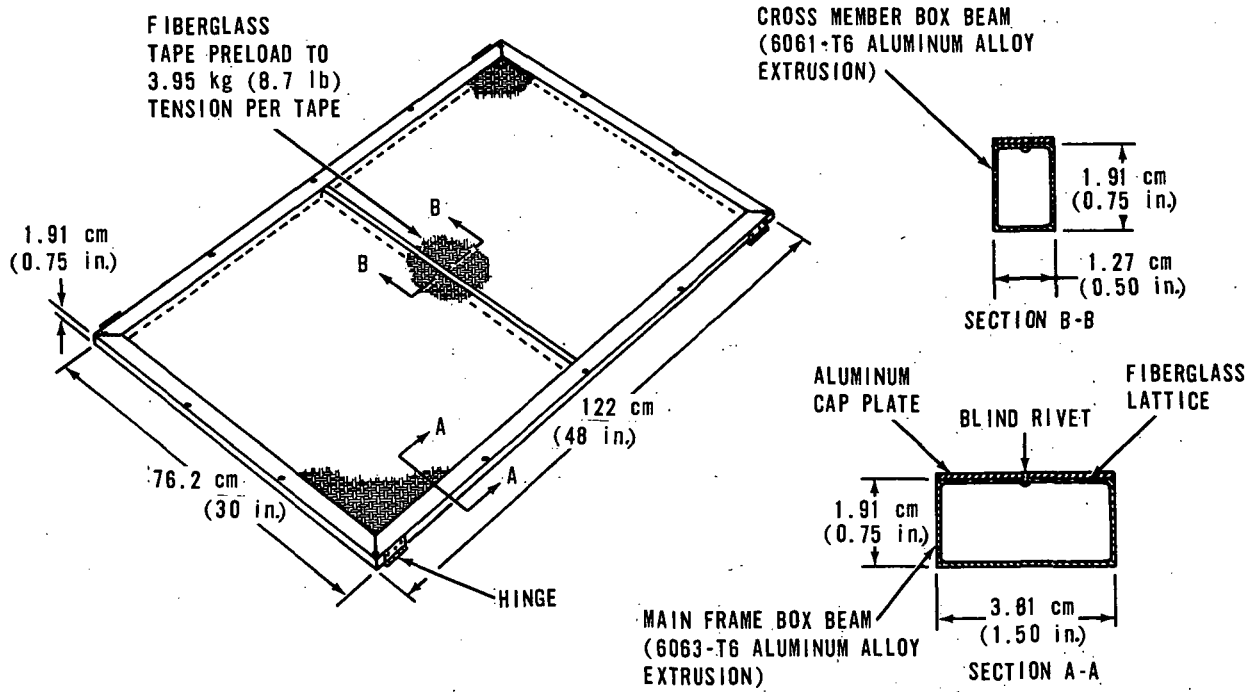


Figure 6. Substrate for engineering test model no. I — aluminum box-beam frame with a fiberglass lattice diaphragm.

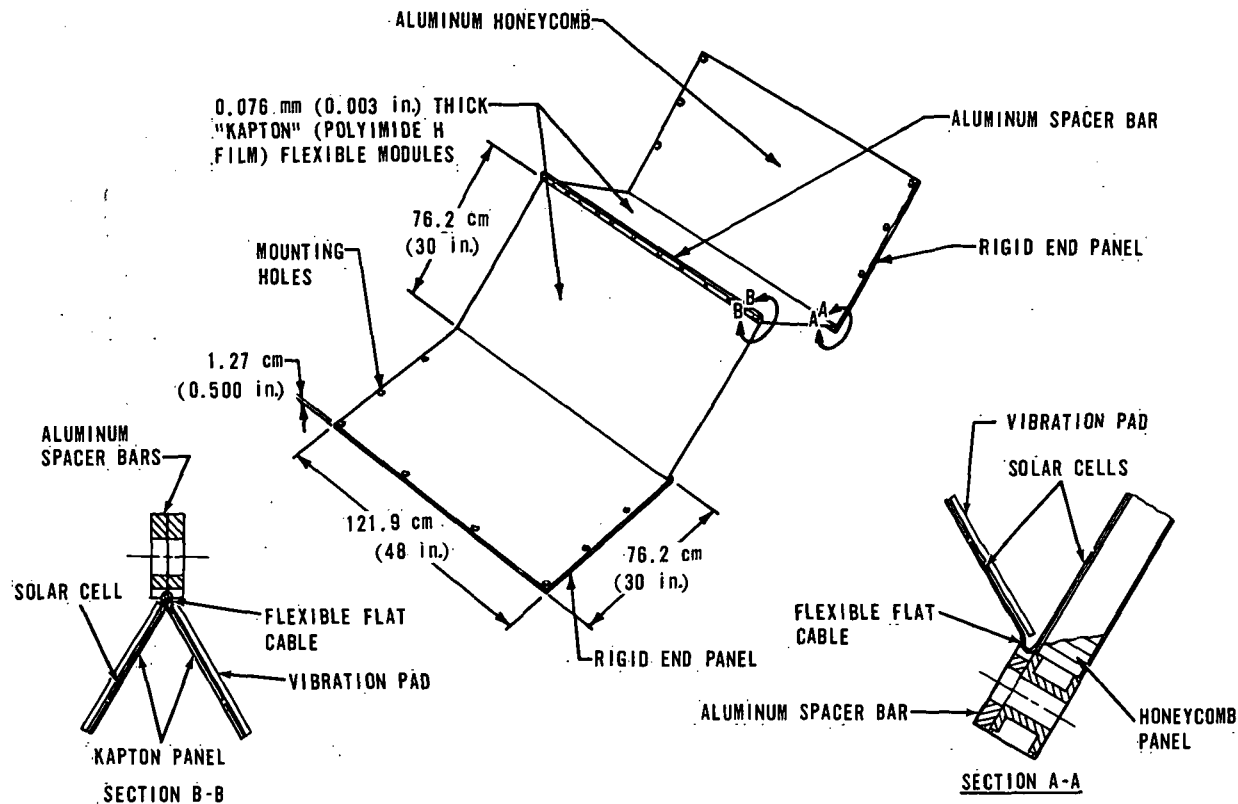


Figure 7. Substrate for engineering test model no. II — aluminum honeycomb end plates with intermediate flexible kapton modules.

0.076-mm thick kapton (H-film) modules that are 76 by 122 cm in area, and aluminum spacer bars are used at the module edges to maintain reasonable planeness of the cell faces. Conceptually, there would be rigid honeycomb panels at each end of the module groups to enable firm tie-down to the lean-to framework. The minimum weight advantage of the kapton would then be realized on the 18 intermediate modules that constitute 90 percent of the total area for each lean-to.:

Since the "tennis racket" and flexible kapton approaches are considered to be beyond the present state-of-the-art, it was felt that one design should be considered that incorporates present day technology to the best advantage for use in a very early mission. The aluminum honeycomb core with graphite-filament-reinforced fiberglass epoxy face sheets shown in Figure 8 meets this objective. For

the 76- by 122-cm module size, sufficient strength and rigidity are obtained with a 0.952-cm thick core and three-ply face sheets consisting of 0.076-mm thick graphite composite outer plies on either side of a 0.076-mm thick fiberglass inner ply. The graphite composite sheet is Morganite Type II and uses NARMCO-5505 epoxy resin filler. The face sheets are bonded to the core with NARMCO-252 adhesive.

A comparison of the important characteristics of each of the three designs is given in Table 1. As was predictable, the flexible kapton design has the highest specific power, the greatest packing factor, and the lowest specific weight. However, it offers the greatest design risk. On the other hand, the graphite filament offers the lowest specific power with the highest specific weight and has the same packing factor as the flexible kapton. Also it offers

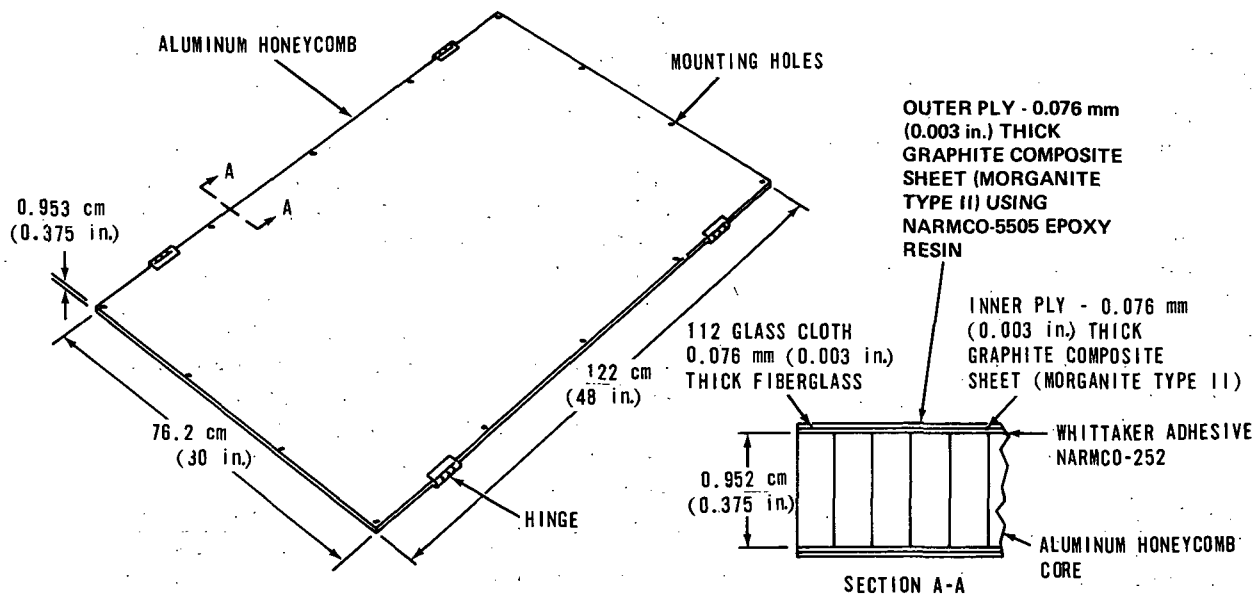


Figure 8. Substrate for engineering test model no. III — aluminum honeycomb core with graphite filament/fiberglass epoxy face sheets.

TABLE 1. COMPARISON OF MODULE CHARACTERISTICS

	ETM I Fiberglass Lattice	ETM II Flexible Kapton	ETM III Graphite Filament
Specific Weight, kg/m ² (lb/ft ²)	2.920 (0.600)	2.280 (0.468)	3.140 (0.644)
Specific Power, W/kg (W/lb)	37.00 (16.75)	47.2 (21.4)	34.1 (15.5)
Packing Factor, percent	74.0	84.4	84.4

the lowest design risk since it uses less sophisticated technology. In comparing the three designs, it was obvious that neither had sufficient advantage to justify dropping the other two. Therefore, all three designs were fabricated and tested. The test plans and results (sharing acoustic exposure, vibration levels, and thermal excursions) are presented in Reference 2. Essentially, the test consisted of exposure to dynamic levels encountered

in a Saturn launch and thermal exposure encountered on the lunar surface. Failures occurred in the aluminum box-beam frame, all electrical interconnects, cell bonding adhesives, and the cell silicon structure.

The failure of the aluminum box-beam frame was primarily superficial and consisted of surface cracking (which did not penetrate the aluminum) and some

slight twisting and bowing action resulting from the fiberglass tensioning. These were concluded to be insignificant margin-of-design problems that were correctable by prestressing the aluminum extrusion and by increasing the cross section stiffness if necessary.

The cell interconnect failures resulted from work-hardening and breaking of the kovar interconnect material because of excessive flexure requirements imposed upon the interconnect. Excessive flexures resulted from normal vibration motions and from cell twisting. Substrate vibration amplitude is adjustable through design changes to shift resonant frequency. The cell twisting resulted from very small bonding dots that were not centrally located under the cells. This is correctable through the use of larger area bonds and through better process controls. Also, a more flexible interconnect material such as silver or copper could be used.

Adhesive bond failures were of two types. First were the failures within the small area adhesive bonds which resulted because of poor process control and the bonds being too small. Also a very wide variation in adhesive bonding ability was in evidence that indicated nonhomogeneity in the material used. The other failures appeared to result from cell and substrate cleanliness; insufficient cleaning prior to bonding was indicated. It was decided that better process controls, greater care in cleaning, and higher design margins in adhesive bond requirements would resolve the adhesive failure problems.

The cell silicon failure (cell spalling) results in a portion of the cell (silicon) retaining its bond to the substrate while the remainder of the cell drops away. The spalling occurs within the silicon crystal and follows very precisely the outline of the adhesive bond. From the appearance of a spalled cell, it is apparent that an interaction between the silicon and adhesive results in stresses in the silicon that exceed the yield limit. To gain additional insight into the relative effects of crystal orientation, solder coating, type of adhesive, thickness of adhesive, and area of bond, a second set of smaller modules was fabricated and tested. Figure 9 shows the matrix of cell and adhesive properties evaluated. In addition to the RTV 3145 adhesive used earlier, three additional types were included.

These were RTV 118, PR 1538, and a 50/50 mixture of RTV 511 and RTV 577. An attempt was made to control bond dot diameters to 0.635, 0.965, and 1.905 cm for each of two bond thicknesses, 0.254 cm and 0.127 cm. In addition to the various adhesive types, thicknesses, and diameters, there were essentially three cell variables that were included. These were: preferred versus random crystal orientation, zone soldered versus fully solder backed, and 2- by 2-cm versus 2- by 4-cm cell size. To incorporate the effects of the substrate, the 49.53- by 42.42-cm module size shown in Figure 9 was built for each of the three module types (fiberglass lattice, flexible kapton, and graphite filament). The modules underwent essentially the same testing as did the original set. The results are described in detail in Reference 3. In general, cell spalling was shown to be a predictable phenomenon based upon design margins and exposure to low temperature. Also, the PR 1538 proved not to be a good solar cell adhesive, and the RTV 118 gave the most satisfying overall results.

CELL SPALLING

During phase II thermal cycle testing of the three engineering test models shown in Figures 6, 7, and 8, spalling of many of the cells occurred at the adhesive bond line. A primary objective of phase II of the program was to investigate the nature of the cell spalling phenomenon. This was accomplished through an analytical assessment of the failure mode combined with an experimental program to evaluate adhesive properties primarily at low temperature (-173°C). Results of the experiments showed that modulus of elasticity (E) and coefficient of linear expansion (α) vary over a considerable range for the adhesives tested (RTV 3145, RTV 511/577, RTV 118, and PR 1538). These measurements reflect a high degree of inconsistency from batch to batch and quite often between samples within a batch.

A computer program was set up to analyze the stresses at various locations within the silicon. Figure 10 shows the effective stress distribution on both sides of the adhesive/silicon interface around the periphery of the bond. The negative distances are those inside the bond periphery and the positive distances are those outside the bond periphery. Effective stresses are shown for four levels within the

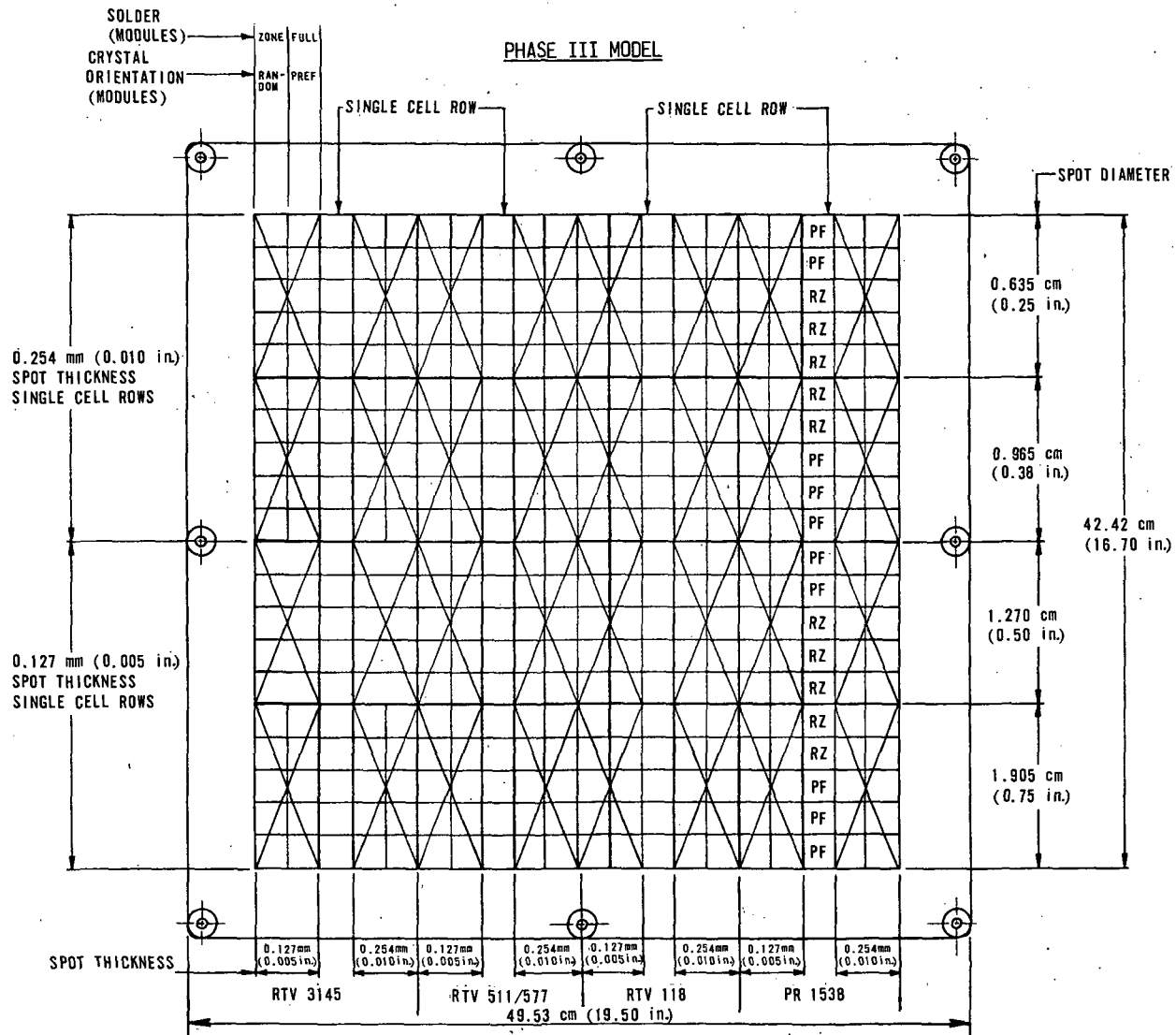


Figure 9. Engineering test model for phase III matrix evaluation.

silicon; 4.3 μm , 17.0 μm , 33.8 μm , and 67.8 μm from the adhesively bonded surface of the silicon. It is noteworthy that the highest effective stresses are very near the surface of the silicon just outside the bond periphery. This implies that even higher stresses might be expected at depths less than 4.3 μm from the surface. This trend declines for deeper levels until at level 4 (67.8 μm) the higher stresses are shown to exist within the periphery of the bond. Since the high peak on the level 1 curve exceeds the ultimate tensile strength of silicon, it

would suggest that the spalling begins at a point outside the bond periphery and propagates underneath the bond through stress concentrations at the leading edge of the fault.

To better understand the effects of adhesive thickness on cell spalling, the curve in Figure 11 was generated. The same computer program was used as for the curves in Figure 10, but instead of assuming 0.508 mm of adhesive, values between 0.150 and 0.500 mm were used. The trend of the curve was

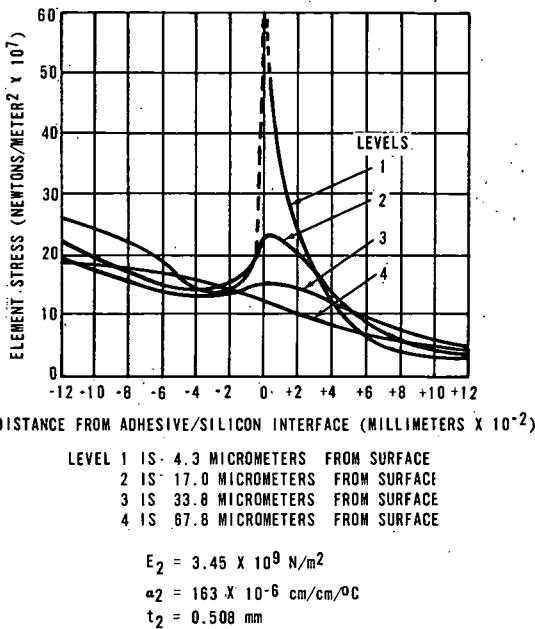


Figure 10. Silicon cell effective stress distribution.

estimated for the very thin adhesive thicknesses but those values are of little practical value. For the curve in Figure 11, adhesive properties of $689 \times 10^6 \text{ N/m}^2$ for modulus of elasticity and $1.22 \times 10^{-4} \text{ cm/cm}^\circ\text{C}$ for thermal coefficient of linear expansion were used. Figure 12 shows curves of solutions to the same stress relation but plotting thermal coefficient of linear expansion versus maximum effective silicon stress for three hypothetical adhesive moduli of elasticity. These curves reflect the situation at the 4.3- μm silicon level for an adhesive thickness of 0.244 mm.

From a number of computer runs similar to those in Figure 12, in which adhesive thickness, modulus of elasticity, and thermal coefficient of linear expansion were varied over realistic ranges of interest, a set of design criteria was generated. These criteria are shown in Table 2 which lists the maximum allowable modulus and coefficient of expansion for each of four thicknesses. Designs that remain within the criteria boundary therefore should not suffer spalling over the lunar surface

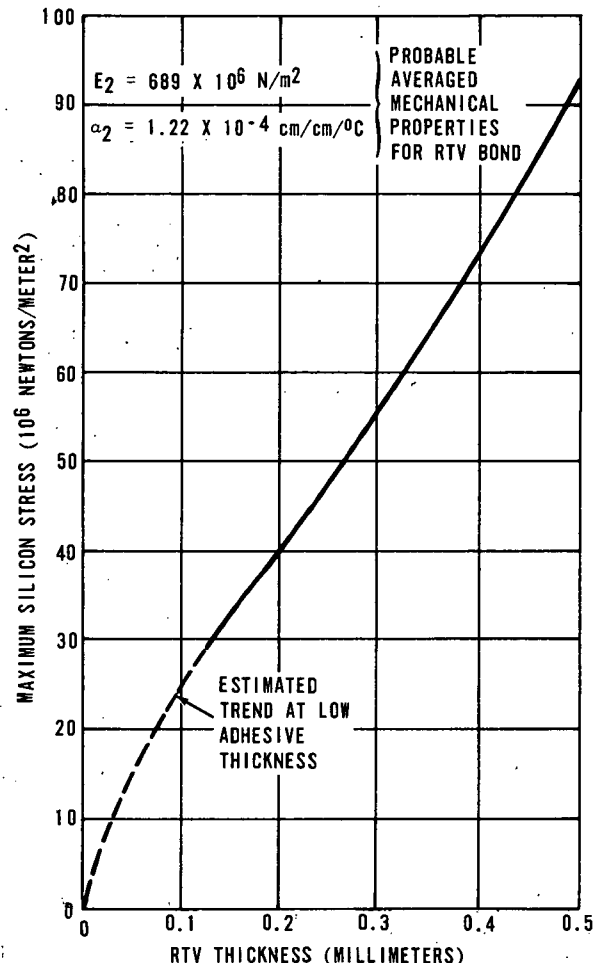


Figure 11. Maximum effective stress in silicon as a function of RTV adhesive thickness.

range of thermal exposure. For other thermal ranges of interest, similar criteria tables may be derived [3].

CONCLUSIONS

The feasibility of a large (45-kWe) solar array for support of a lunar-based water electrolysis depot has been demonstrated through analytical study and through prototype hardware fabrication and test. The required energy could be obtained from flat laydown, lean-to, or fully oriented array sections. Voltage

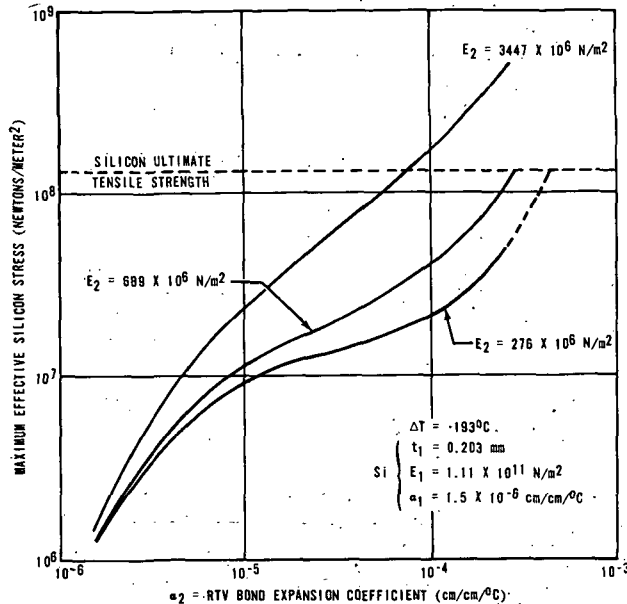


Figure 12. Silicon thermal stress - RTV adhesive thickness, $t = 0.254$ mm at a 4.3- μ m stress level.

levels required for water electrolysis equipment can be provided with no great difficulty, and the hostile lunar thermal environment may be tolerated with proper cell stack design. Array panel stacks using at least three different advanced technology module designs have been proven feasible from a fabrication and endurance test standpoint, and packaging within the allowable launch envelope has been demonstrated in preliminary design detail. A novel scheme was devised for use of the interpanel launch vibration padding. These blankets are folded outward onto the lunar surface adjacent to the lean-to and serve as highly reflective thermal control skirts that prevent high temperature buildup over that area of the lunar surface.

TABLE 2. ALLOWABLE ADHESIVE PROPERTIES VERSUS t

RTV Thickness	Maximum Average Adhesive Properties	
t_2	$E_2, 10^6 \text{ N/m}^2$	$\alpha_2, \text{ cm/cm/}^\circ\text{C}$
0.127 mm (0.005 in.)	275	7.5×10^{-4}
	689	4.6×10^{-4}
	3447	1.4×10^{-4}
0.254 mm (0.010 in.)	275	4.3×10^{-4}
	689	2.7×10^{-4}
	3447	7.3×10^{-5}
0.381 mm (0.015 in.)	275	3.8×10^{-4}
	689	2.2×10^{-4}
	3447	4.9×10^{-5}
0.508 mm (0.020 in.)	275	3.3×10^{-4}
	689	1.7×10^{-4}
	3447	3.7×10^{-5}

From the six large panels that were fabricated and tested, the graphite filament reinforced fiber-glass face sheet panel was selected for final qualifications. This design offers the optimum tradeoff of power-to-weight ratio and technology risk. It is felt that this design will not become obsolete through the 1975 time period. Design criteria generated relating to the cell spalling phenomenon should be very beneficial to other high thermal excursion solar array designs indefinitely, both on the lunar surface and in deep space.

REFERENCES

1. Second Phase Report on Study of a Water Electrolysis System to Support an Intermediate Size Lunar Mission. Chrysler Corporation Space Division Report HGS-R14-69, Huntsville, Ala., April 30, 1969.
2. Boretz, John: Study to Establish Criteria for a Solar Cell Array for Use as a Primary Power Source for a Lunar-Based Water Electrolysis System Phase I. Final Technical Report, TRW Systems Group, June 30, 1968.
3. Boretz, John: Study to Establish Criteria for a Solar Cell Array for Use as a Primary Power Source for a Lunar-Based Water Electrolysis System Phase III. Final Technical Report, TRW Systems Group, December 15, 1970.

THERMOELECTRIC GENERATOR TEST PROGRAMS AT MSFC

By

L. E. Young

SUMMARY

This paper describes the results of two thermoelectric generator test programs. In one of these programs a SNAP-19 radioisotope thermoelectric generator was evaluated, and in the other a compact thermoelectric module, TEM-9U, is presently being evaluated.

The SNAP-19 generator test program, completed in 1970, consisted of a 23 687-hr thermal-vacuum endurance test that revealed generator degradation effects, performance characteristics, and response to thermal cycling. The overall power decrease from 25.0 to 14.1 W was primarily caused by an increase in internal resistance. During the test the maximum power point gradually shifted from 2.24 V at 11.2 A to 2.08 V at 6.79 A. Post-test inspection of the generator revealed some degree of lead-telluride couple sublimation resulting from the near-vacuum final internal pressure. The test program provided important first-hand data and experience needed for future Marshall Space Flight Center (MSFC) flight application of similar generators.

The TEM-9U compact thermoelectric module test program has been underway since April 1970, and more than 6000 hr of test time have been accumulated. At 5600 hr the power output degradation rate was 0.7 percent per 1000 hr. Tests were made to evaluate both steady-state and transient performance characteristics and additional tests are planned. Computerized math models have been developed that can closely predict generator thermal/electrical performance.

INTRODUCTION

Thermoelectric generator test programs at MSFC include the SNAP-19 radioisotope thermoelectric generator endurance test completed in February 1970 and the TEM-9U tubular module performance and endurance test that has been in progress since April 1970. The primary purpose of the test programs

is to evaluate thermoelectric devices for applicability to future MSFC flight programs.

The SNAP-19 test program revealed the effects of long term thermal-vacuum operation on the generator. The test was conducted in a thermal-vacuum chamber to simulate a space environment with various heat sink temperatures. The generator was electrically heated.

As of February 1971, the TEM-9U generator had accumulated a total run time of 5750 hr of which the first 112 hr were conducted by the developer, Westinghouse Astronuclear Laboratory. The module, designed to be heated with flowing liquid metal alloy (sodium-potassium--NAK-78), is a static test version that is electrically heated and is cooled by air flow.

SNAP-19 GENERATOR TEST PROGRAM

Description of SNAP-19 Generator

The SNAP-19 test generator, serial number 19 (SN 19), was built by the Martin-Marietta Corporation (now Isotopes, A Teledyne Company). The SN 19 generator differs from previous SNAP-19 generators in that it uses 2N-2P elements that failed to pass a visual examination for surface defects but were electrically acceptable [1].

The generator is shown in Figure 1. The body of the generator is approximately 27.30-cm high and 20.32 cm in diameter. The overall diameter is approximately 48.26 cm. The fins and body have a thermal coating of zirconia to enhance heat dissipation. A cross section of the generator and its instrumentation is shown in Figure 2. The internal thermocouple (TC) leads, the output leads, and the heater power input leads exit through two potted electrical connectors on the generator casing. The output leads terminate at a bus bar on the side of the generator for connection to external circuitry.

The SNAP-19 is a low voltage, high current electrical generator designed to produce approximately

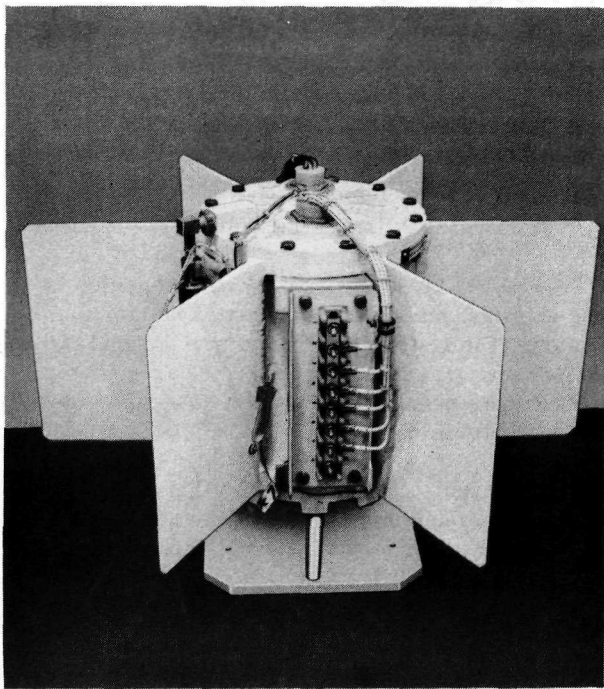


Figure 1. SNAP-19 radioisotope thermoelectric generator, SN 19.

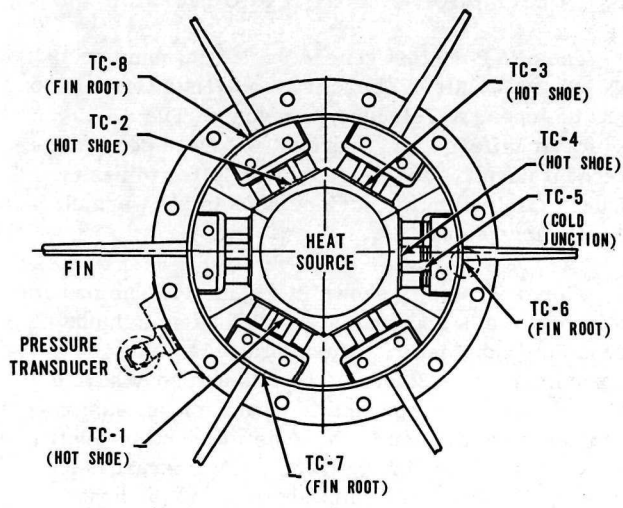


Figure 2. SNAP-19 cross section and instrumentation.

30 W at 2.5 V to 2.7 V. It generates electricity by utilizing the Seebeck effect between junctions of dissimilar materials maintained at different temperatures. The 2N-2P lead-telluride (Pb-Te) thermoelectric elements are located in the heat path between the fuel block and the thermal radiating surfaces. The hot junctions are surface-mated to the fuel block, which in this case is simulated by an electrical resistance heater. Critical SNAP-19 operational parameters recommended by the manufacturer are as follows:

1. Hot junction temperature shall not exceed 538°C.
2. Fin root temperatures shall not exceed 196°C.
3. Change in fin root temperature shall not exceed 18°C in 10 min.

The thermoelectric elements are assembled in 6 modules of 15 couples arranged in a series-parallel matrix. Each module contains five rows of three couples in parallel. Each row is electrically in series with the next row. Since each module is also in series with the next module, the generator consists of a matrix of couples, 3 in parallel by 30 in series. The elements are 1.27-cm long and 0.957 cm in diameter.

SNAP-19 Test Setup Description

The thermal vacuum facilities used for SNAP-19 tests are located in the MSFC Astrionics Laboratory. Redundant and isolated pumping systems were used to preclude test failure resulting from loss of vacuum. The test chamber (Fig. 3) was capable of obtaining 1.33×10^{-3} N/m² vacuum and -90°C to 120°C thermal shroud temperature limits with an operating SNAP-19 inside.

The test equipment was specially designed to provide automatic monitoring of test parameters and to ensure reliability throughout the test program. Redundant power supplies were used for test cabinet internal power and for input power to the SNAP-19 heater. In case of commercial power failure, a facility emergency generator automatically provides power. Two controllers were used in the test equipment; a power supply controller and alarm panel, and a fin root and hot junction controller. The data acquisition system was a Hewlett-Packard, Model 2010A, 25-channel digital scanning system.

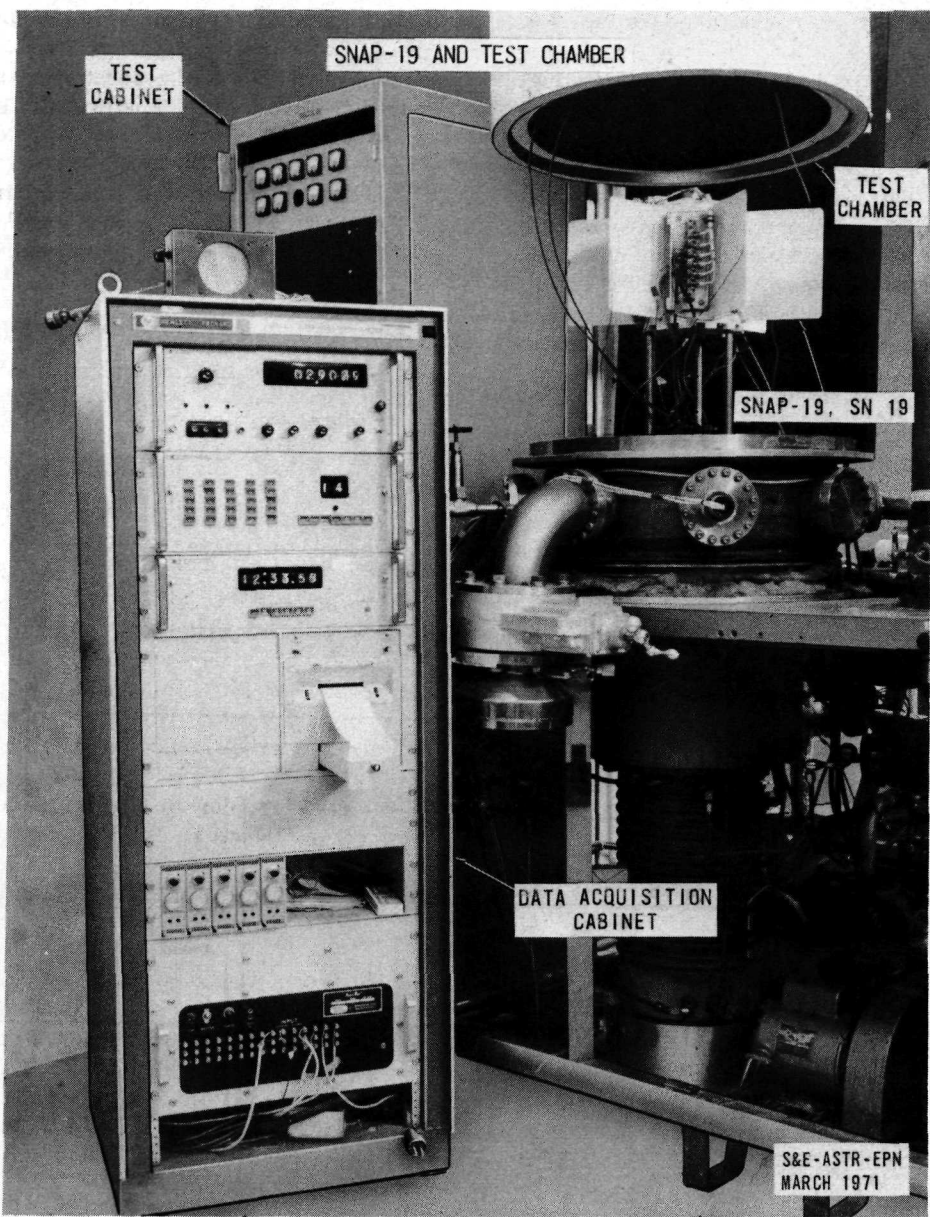


Figure 3. SNAP-19 test chamber and test equipment.

Endurance Test Description

The SNAP-19 generator was subjected to a 23 687-hr endurance test. The generator was initially tested by the manufacturer for 5651 hr in an ambient environment. The manufacturer's test [1] was conducted in air (1 atm) with insulating "boots" placed over the fins to raise generator temperatures to the values expected in an orbital environment. The environmental conditions and thermal input power were

essentially constant during the manufacturer's test. The final 18 036 hr of testing were conducted at MSFC in a thermal-vacuum chamber that was maintained at a 1.33×10^{-3} N/m² pressure level, or less, for all vacuum tests. Thermal power input to the SNAP-19 was maintained at a nominal 570 W.

The five-phase MSFC test consisted of a thermal cycle test, hot soak test, cold soak test, second hot soak test, and an ambient temperature soak test.

Parametric (performance) tests were performed before, during, and after endurance testing.

During the initial 8600 hr of vacuum testing, the vacuum chamber shroud temperature was cyclicly varied between 90°C and -10°C to generate a fin root temperature cycle as shown in Figure 4. Following the thermal cycle test, a hot soak test was conducted at a temperature of approximately 88°C for approximately 1500 hr, and a cold soak test was conducted at approximately 90°C for about 250 hr. Then, a second hot soak test and an ambient temperature soak test were conducted for approximately 2900 hr and 3600 hr, respectively.

During endurance testing, measurements were recorded hourly for hot junction temperature, fin root temperature, fin tip temperature, shroud temperature, load voltage and current, heater voltage and current, chamber pressure, and generator internal pressure.

Six ambient and four vacuum parametric tests were made to determine generator performances at

three stable load points and to enable calculation of the maximum power point. At each load point, instantaneous open-circuit voltage was measured to enable calculation of generator internal resistance and effective Seebeck coefficient. From the data measurements, the following were calculated:

Effective generator Seebeck coefficient,

$$\alpha = \frac{V_{OC}}{T_{HJ} - T_{CJ}}$$

Generator internal resistance,

$$R_g = \frac{V_{OC} - V_L}{I_L}$$

Load resistance,

$$R_L = \frac{V_L}{I_L}$$

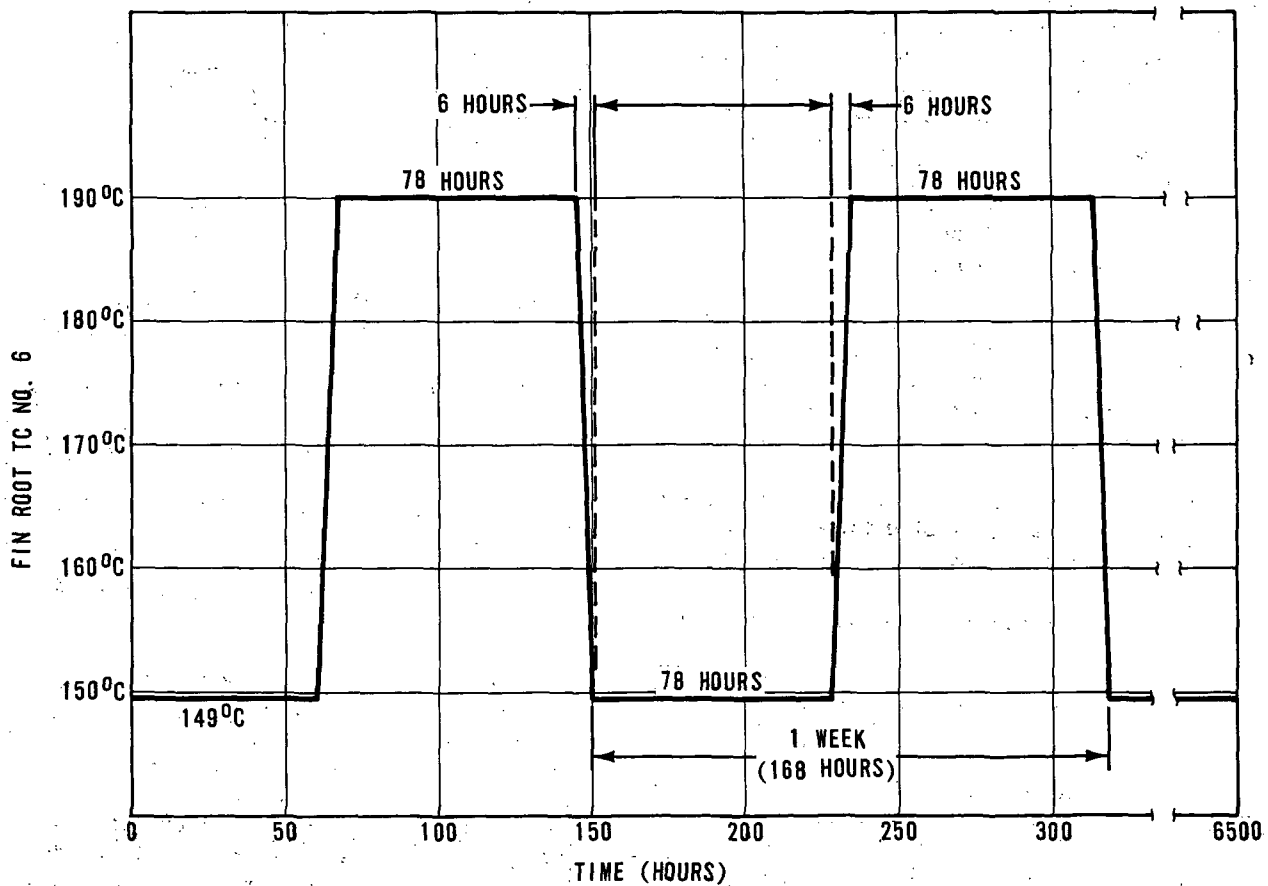


Figure 4. Thermal test cycle (fin root).

Power Output,

$$P_O = V_L I_L$$

Parameters T_{HJ} , T_{FR} , V_{OC} , R_L , R_G , V_L , and P_O were then plotted versus load current I_L . The maximum power point was obtained by determining a least squares fit for the voltage-current curve and mathematically computing the maximum point on the power-current parabola.

SNAP-19 Generator Test Results and Performance

PARAMETRIC DATA

Performance Comparison. Of principal interest is a comparison of the parametric test results that represent the SNAP-19 performance at the beginning of MSFC testing in December 1967 and at the end of MSFC testing in February 1970. The parametric tests shown in Figures 5 and 6 are the initial ambient parametric tests and the final vacuum parametric tests performed. These tests were made with approximately the same cold junction temperature and with the same power input, and a meaningful comparison can be made. In Figures 7 and 8 the V-I and P-I curves of these parametric tests are compared.

As shown, the initial maximum power of 21.39 W occurred at 2.24 V and 9.6 A. After 22 months of operation, the maximum power had decreased to 14.55 W at 2.15 V and 6.78 A. This was largely a result of the increase in internal resistance.

Table 1 shows a comparison of all major operating parameters at the initial and final maximum power conditions. As shown, the changes were:

1. A 32-percent decrease in maximum power P_{MAX} .
2. A 9-percent increase in hot junction temperature T_{HJ} .
3. A 47-percent increase in internal resistance R_I .
4. A 4-percent decrease in load voltage V_L .

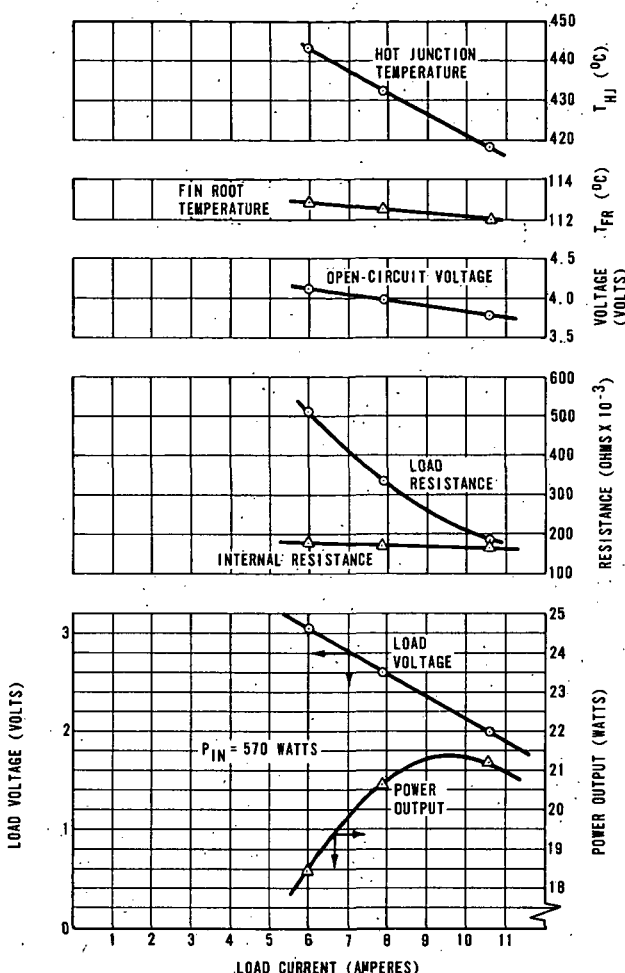


Figure 5. SNAP-19 parametric test, ambient, fins uninsulated, December 1967 (5667 hr).

5. A 30-percent decrease in load current I_L .
6. No change in open-circuit voltage V_{OC} .
7. A 12.4-percent decrease in Seebeck coefficient α .
8. A 1.2-percent decrease (arithmetical) in efficiency η .

Table 2 gives a comparison at equal voltages (2.6 V). Other comparisons of interest are given in Tables 3 and 4 which compare major parameters on the basis of equal load current and equal load resistance, respectively. In each case the percentage changes closely represent the generator performance changes that would have occurred had the generator been maintained at 6-A load or at 0.5Ω external

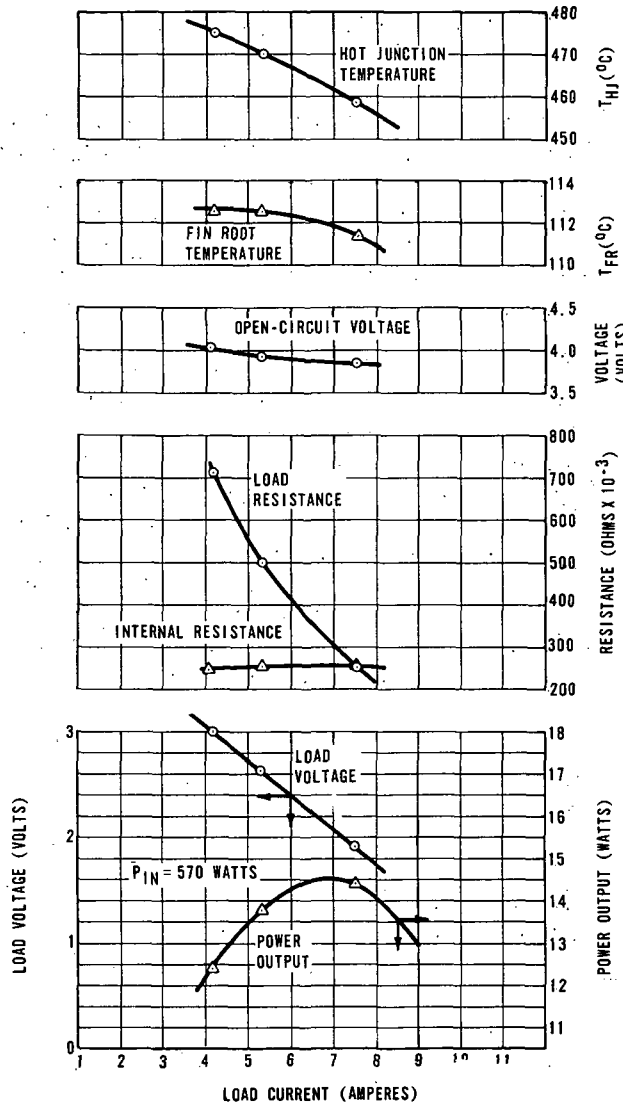


Figure 6. SNAP-19 parametric test, vacuum, February 1970 (23 420 hr).

resistance for the entire thermal-vacuum test period.

Power Degradation Analysis. An analysis was made to identify the components of the maximum power degradation. The final internal resistance was approximately 0.08Ω greater (a 47-percent increase) than the initial value. Therefore, the final load voltage would have been $0.08 I_L$ V higher if the internal resistance had not changed; also the power would have been greater by $0.08 I_L^2$. By

making these corrections, the adjusted curves (dotted) previously shown in Figures 7 and 8 are obtained. The maximum power point was obtained by computing the maximum value of $V_L I_L$ from

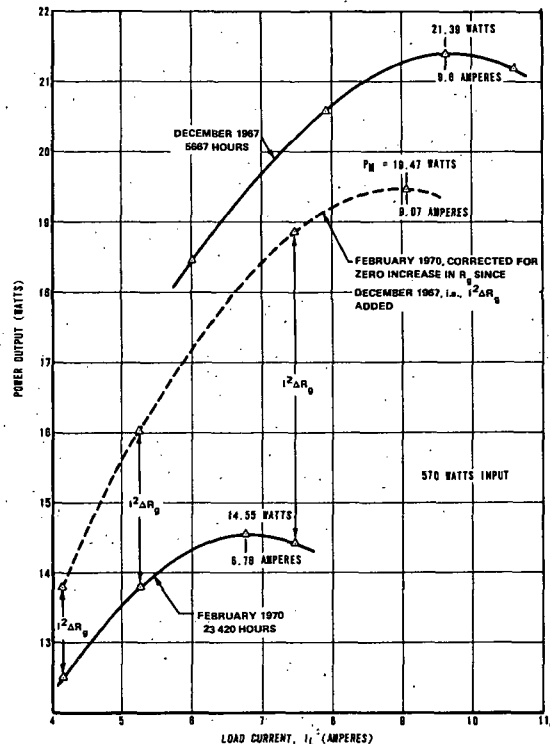


Figure 7. SNAP-19 power comparison, December 1967 versus February 1970.

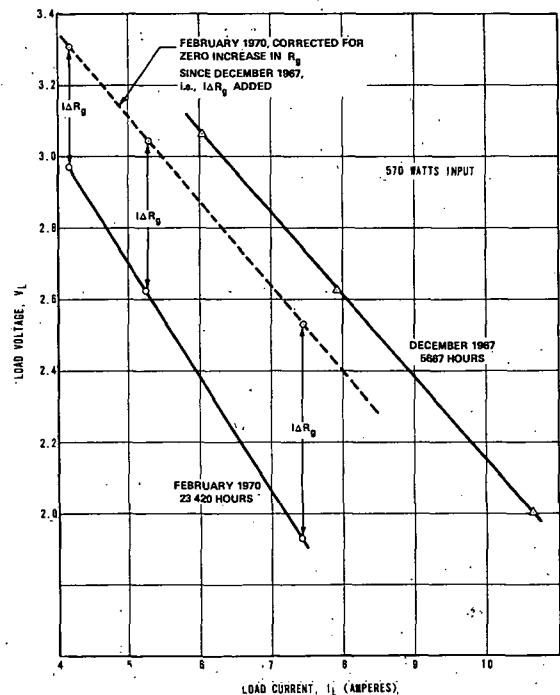


Figure 8. SNAP-19 voltage comparison, December 1967 versus February 1970.

TABLE 1. COMPARISON AT MAXIMUM POWER

Parameter	December 1967	February 1970	$\Delta\%$
P_{MAX} (W)	21.4	14.5	-32
T_{HJ} ($^{\circ}$ C)	423	462	+9
T_{FR} ($^{\circ}$ C)	112	112	0
R_g (Ω)	0.17	0.25	+47
V_L (V)	2.23	2.15	-4
V_{OC} (V)	3.85	3.85	0
I_L (A)	9.60	6.78	-30
η (%)	3.76	2.56	-1.20 ^a
α (mV/ $^{\circ}$ C)	13.87	12.15	-12.4

a. Arithmetical difference in initial and final efficiency.

TABLE 2. COMPARISON AT EQUAL VOLTAGE OF 2.6 V

Parameter	December 1967	February 1970	$\Delta\%$
P_{MAX} (W)	20.8	14.0	-33
T_{HJ} ($^{\circ}$ C)	431	469	+9
T_{FR} ($^{\circ}$ C)	112	112	0
R_g (Ω)	0.17	0.25	+47
V_{OC} (V)	3.95	3.95	0
I_L (A)	7.99	5.40	-33
η (%)	3.64	2.46	-1.18 ^a
α (mV/ $^{\circ}$ C)	13.89	12.15	-12.4

a. Arithmetical difference in initial and final efficiency.

the best-fit straight line representing V_L versus I_L (least squares fit).

From these adjusted curves, several observations can be made:

1. The maximum power P_{MAX}' is within 1.9 W of the initial P_{MAX} .

TABLE 3. COMPARISON AT EQUAL CURRENT OF 6.0 A

Parameter	December 1967	February 1970	$\Delta\%$
T_{HJ} ($^{\circ}$ C)	443	466	+5
T_{FR} ($^{\circ}$ C)	112.8	112.3	~0
R_g (Ω)	0.170	0.250	+47
V_L (V)	3.1	2.4	-23
P (W)	18.4	14.3	-23
V_{OC} (V)	4.1	3.9	-5
η (%)	3.23	2.51	-0.72 ^a
α (mV/ $^{\circ}$ C)	13.90	12.15	-12.6

a. Arithmetical difference in initial and final efficiency.

TABLE 4. COMPARISON AT EQUAL LOAD RESISTANCE OF 0.5 Ω

Parameter	December 1967	February 1970	$\Delta\%$
T_{HJ} ($^{\circ}$ C)	443	470	+6
T_{FR} ($^{\circ}$ C)	112.8	112.6	~0
R_g (Ω)	0.170	0.250	+47
V_L (V)	3.1	2.6	-16
P (W)	18.4	13.8	-25
V_{OC} (V)	4.1	3.9	-5
I_L (A)	6.0	5.3	-12
η (%)	3.23	2.42	-0.81 ^a
α (mV/ $^{\circ}$ C)	13.90	12.00	-13.7

a. Arithmetical difference in initial and final efficiency.

2. P_{MAX}' occurs at the same voltage as the final maximum power, but at 9.07 A instead of 6.78 A.

3. If R_g had not increased, the power decrease would have been only 9 percent compared to an actual decrease of 32 percent.

4. The adjusted V-I curve, in the current range of 6 to 7 A, is below the initial V-I curve by approximately 0.2 V, which nearly equals the decrease in open-circuit voltage (measured at equal current values). Therefore, had the open-circuit voltage not decreased, the adjusted V-I and P-I curves would tend to coincide with the initial curves of December 1967.

From these observations it is concluded that the major components of the 6.8-W power degradation are (1) the increase in generator internal resistance and (2) the decrease in effective Seebeck coefficient, where (1) accounts for 4.9 W and (2) accounts for 1.9 W.

It is also of interest to examine the percentage power loss resulting from internal resistance. From examination of Table 1 the initial $I^2 R_g$ loss was 15.7 W, or 73 percent of P. The final $I^2 R_g$ loss was 17 W or 116 percent of P_0 .

In-Process Parametric Tests. Several in-process ambient and vacuum parametric tests were conducted between December 1967 and February 1970. These tests were conducted at various fin root temperatures and are useful primarily for tracing changes in maximum power, Seebeck coefficient, and internal resistance. Based on the initial, in-process, and final vacuum parametric tests, Figures 9 and 10 show the changes in P, α , and R_g during testing.

Maximum Power Versus Load Current. In all of the parametrics it is noted that the maximum output occurs at a lower current value than where the load resistance R_L equals the generator

internal resistance R_I . The "matched load" point is where the load voltage drop is equal to one-half the instantaneous open-circuit voltage V_{OC} . A linear V-I curve connecting the point $V = V_M$ and $I = I_M$ (corresponding to $R_L = R_I$) with the point $V = V_{OC}$ and $I = 0$ would have the equation

$$V = V_{OC} - \frac{V}{I_M} I$$

where V/I_M is the slope of the line and E_{OC} is constant and not current dependent. Based on this equation, the maximum value of VI occurs at $I = I_M$. Therefore, maximum power would occur where $R_L = R_I$. Since the SNAP-19 was operated at constant thermal input power, lowering of the load current below the matched load current results in reduced Peltier cooling of the hot junction causing higher hot junction temperature and higher Seebeck voltage (V_{OC}). This results in a V-I curve with a greater slope than V/I_M and causes the maximum value of VI to occur at a lower current than I_M ,

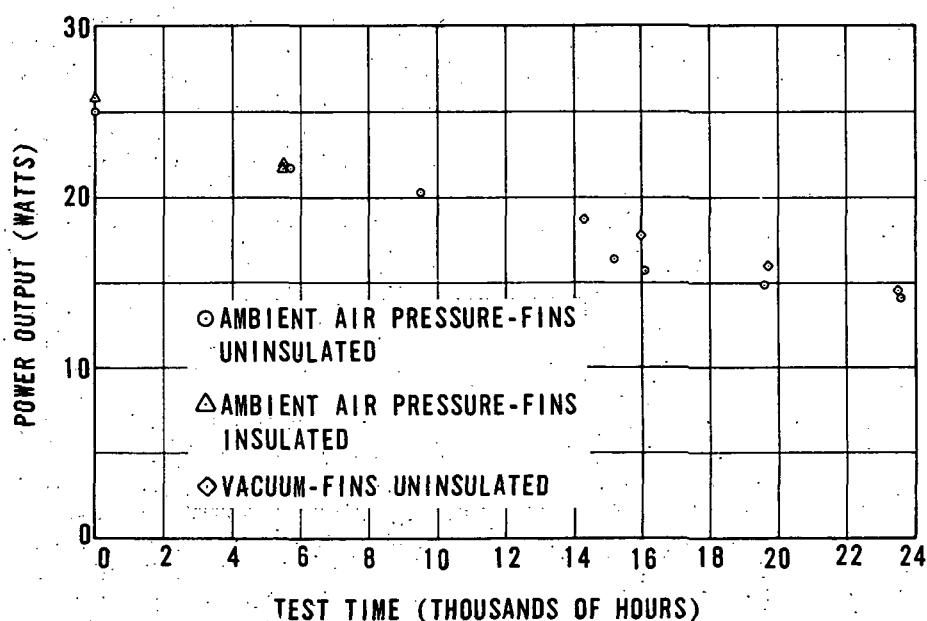


Figure 9. Peak power versus time (from parametric tests).

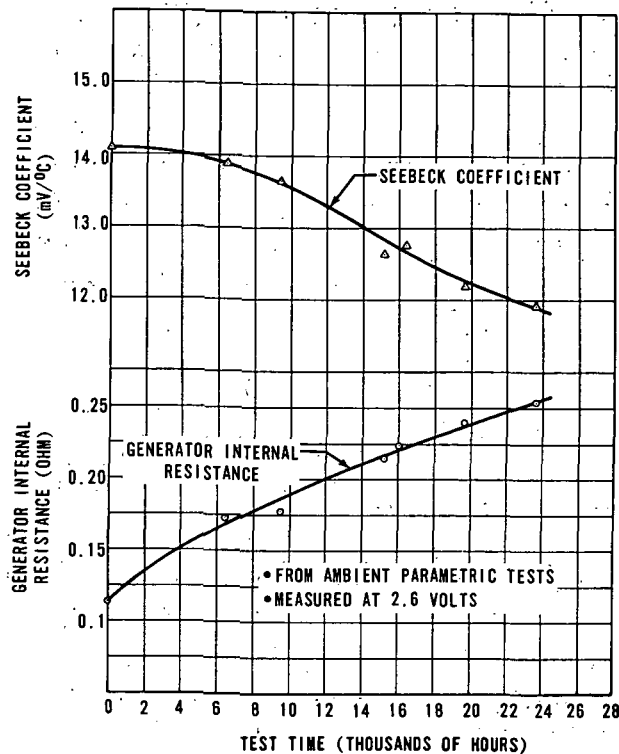


Figure 10. Seebeck coefficient and internal resistance versus time.

a behavior that has also been observed for other thermoelectric generators.

Comparison of Initial and Final Ambient Performance. Based on the manufacturer's initial ambient parametric test performed at MSFC in February 1970, the following basic changes occurred over the 23 687-hr testing duration:

	Manufacturer's Initial Test	Final MSFC Test	Percent Change at Maximum Power Point
P _{MAX} (W)	25.0	14.1	43-% decrease
α (mV/°C)	14.1	12.2	14-% decrease
R _I (Ω)	0.115	0.253	120-% increase
η (%)	4.39	2.48	1.91% (arithmetical)

ENDURANCE TEST OVERALL PERFORMANCE

During the life of the SN 19 generator, 5651 hr of testing were performed by the manufacturer. Of this amount, 5460 hr were devoted to an endurance

test in air with the fins insulated to raise the fin root temperature to the expected mission operating temperature of 171°C, and 191 hr were devoted to parametric testing. The 18 036 hr of thermal-vacuum testing at MSFC included 1328 hr of parametric testing. Total generator operating time was 23 687 hr when the test was terminated for program reasons.

The generator was still operating at an output power of 13.7 W at 2.6 V and with an efficiency of 2.39 percent at test termination. Generator power output during the 2.25 years of MSFC testing is shown in Figure 11.

The generator internal pressure history is shown in Figure 12. The apparent decrease of internal pressure to 0 N/m² (0 psia), as indicated by the pressure transducer, was a major influence in continuing the test beyond 16 000 hr. Under relatively high operating temperature conditions and with low residual internal gas pressure, sublimation of Pb-Te material at hot shoe junctions that could result in a more rapid deterioration of generator performance was postulated. The fact that this was not observed is apparent in the approximately linear decrease in output power with time as shown in Figure 11. Parametric tests also failed to show an accelerated change in the internal resistance. Because of the apparent absence of significant sublimation, doubt was cast upon the validity of the pressure transducer indication of internal pressure. Post-test examination and calibration checking of this transducer was performed. However, it should be noted from Figure 12 that the transducer indicated pressure rises in the generator corresponding to the times when the vacuum chamber was opened and the generator exposed to atmospheric pressure externally. This could indicate either a leak into the generator or into the pressure transducer. As previously shown in Figure 11, the rate of power decrease was 0.782 W per 1000 hr during the generator testing at the manufacturer. During the testing at MSFC, the rate of power change decreased to 0.469 W per 1000 hr. This difference in degradation rate is not definitely explained. Degradation can usually be attributed to: (1) diffusion into the couple elements that results in internal composition change affecting the internal resistance or Seebeck coefficient or (2) material transport that reduces contact area or cross-sectional area and increases the generator internal resistance. Hence, these effects would normally be accelerated by operating the generator at higher hot junction temperatures. As indicated by Figure 13, the SNAP-19

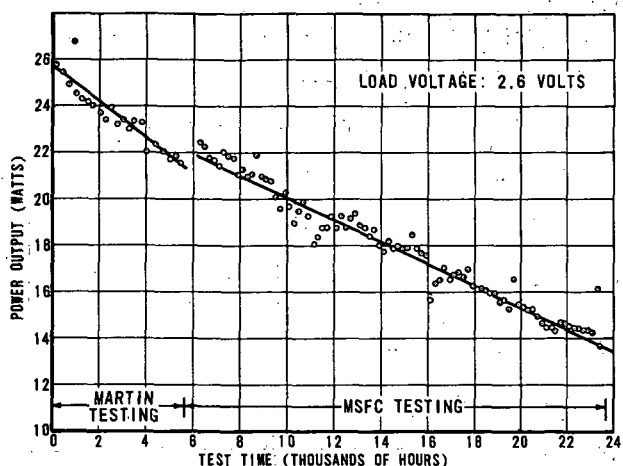
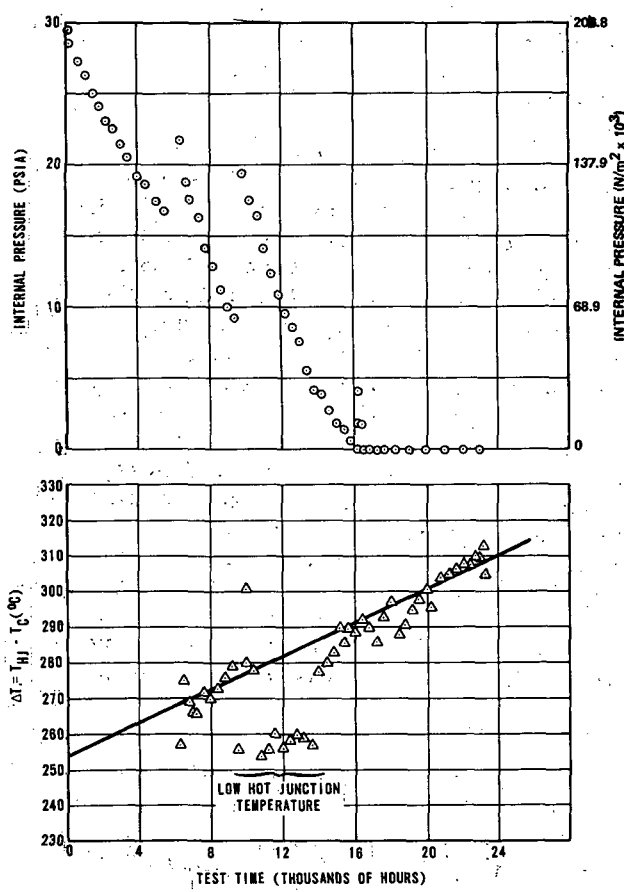


Figure 11. SNAP-19 power history.

Figure 12. SNAP-19 internal pressure and ΔT history.

was operated at MSFC with generally higher hot junction temperatures than in the tests by the manufacturer, except for the low temperature period of the MSFC thermal cycling test.

PRINCIPAL RESULTS AND CONCLUSIONS

The principal results and conclusions of the SNAP-19 endurance test are as follows:

1. The generator operated successfully for 23 687 hr with no malfunctions occurring and no maintenance required in the conversion system.
2. Maximum power decreased from 25.0 W to 14.1 W, a decrease of 1.85 percent per 1000 hr. This degradation rate was slightly less than that reported for the two SNAP-19 generators flying on the Nimbus weather satellite [2].
3. Initial efficiency at maximum power was 4.39 percent; final efficiency at maximum power was 2.48 percent.
4. The power degradation was caused principally by a rise in the internal resistance, which increased by 120 percent over the 23 687-hr test. During the 18 036 hr of testing at MSFC, the decrease in maximum power attributed to an increase in internal resistance was 4.9 W; the remainder of the decrease, 1.9 W, was attributed to the decrease in effective Seebeck coefficient.
5. The pressure of the argon cover gas within the generator decreased until the pressure transducer indicated zero pressure at 16 000 hr. Generator performance showed no accelerated effects resulting from vacuum sublimation of thermocouple material, or from air leakage into the generator during exposure to atmosphere.
6. The hot junction to cold junction temperature difference, ΔT , increased approximately 40°C. This was attributed to a decrease in Peltier cooling of the hot junctions with the lower generator currents and an increase in thermal impedance of the generator.
7. The final open-circuit voltage at maximum power was slightly greater than the initial open-circuit voltage. This was a result of the increased ΔT which offset the decrease in Seebeck coefficient.
8. During the 23 687-hr test period, the maximum power point shifted from 2.24 V at 11.2 A to 2.08 V at 6.79 A.

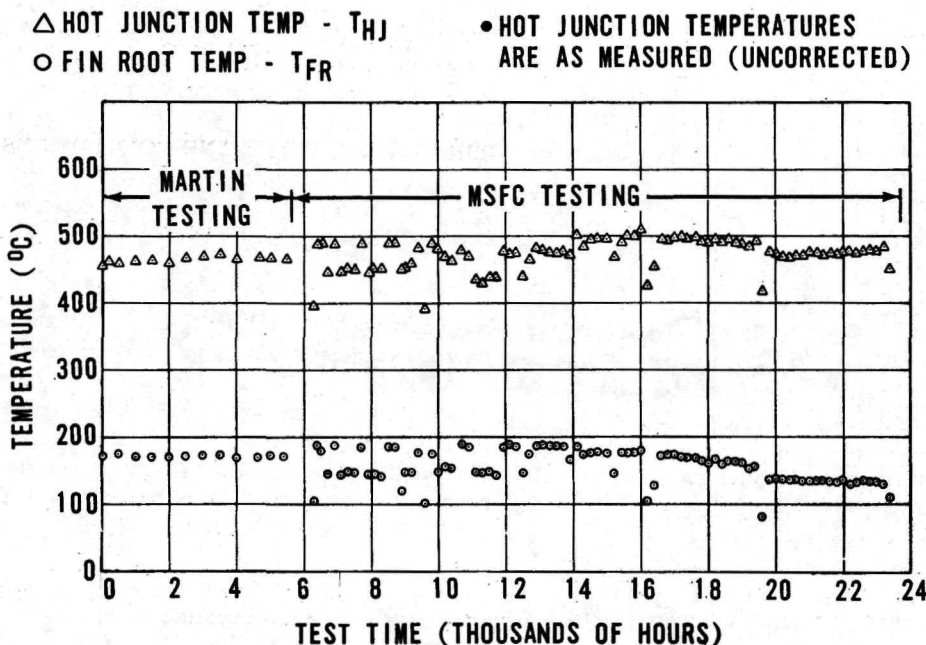


Figure 13. Temperature versus test time.

TEM-9U TUBULAR MODULE TEST PROGRAM

The TEM-9U tubular thermoelectric module (SN 17) has been under test at MSFC since April 1970. It is being evaluated for potential flight application as a prime energy converter for a reactor/thermoelectric power system. The test item is an 18.288-cm (7.2 in.) active length, electrically heated, air-cooled module developed by Atomics International and Westinghouse Astronuclear Division for the Atomic Energy Commission. It is being evaluated with regard to load performance, internal properties, transient performance, power degradation versus time, and system integration considerations. In addition, computerized mathematical models are being developed to predict thermal/electrical performance parameters.

Description of TEM-9U Generator and Test Equipment

The TEM-9U module, SN 17, is one of a series of compact tubular modules using 2N-2P lead-telluride thermoelectric couples. With respect to previous modules, it incorporates design improvements that are intended to result in reduced power

degradation versus operating time. The SN 17 module is shown in Figure 14. The lead-telluride thermoelectric elements are washer-shaped and are stacked within a metal enclosure. In normal operation hot liquid metal (NaK) would flow through the inner bore, and the outer surface would be cooled with cooler NaK, with the resultant ΔT producing electrical power. The test module, however, is heated by an electrical heater immersed in captive NaK within the inner bore. Heat is removed from the outer surface by air flowing over attached cooling fins. Inner and outer surface temperatures are monitored by means of 26 chromel-alumel thermocouples mounted as shown in Figure 15.

The module is mounted within a test console as shown in Figure 16. The console is made up of:

1. A variable speed air blower.
2. An automatic controller for regulation of heater power and hot side temperature.
3. A thermocouple reference junction for module temperature monitoring.
4. A resistive load bank.
5. An overtemperature circuit breaker.

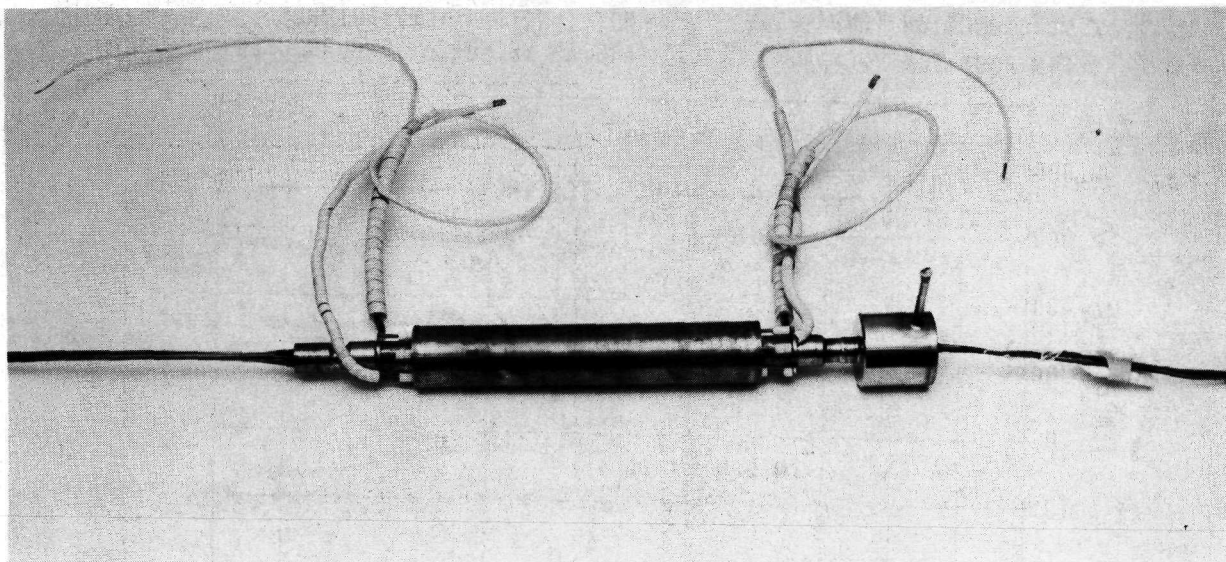


Figure 14. TEM-9U module assembly, less cooling fins.

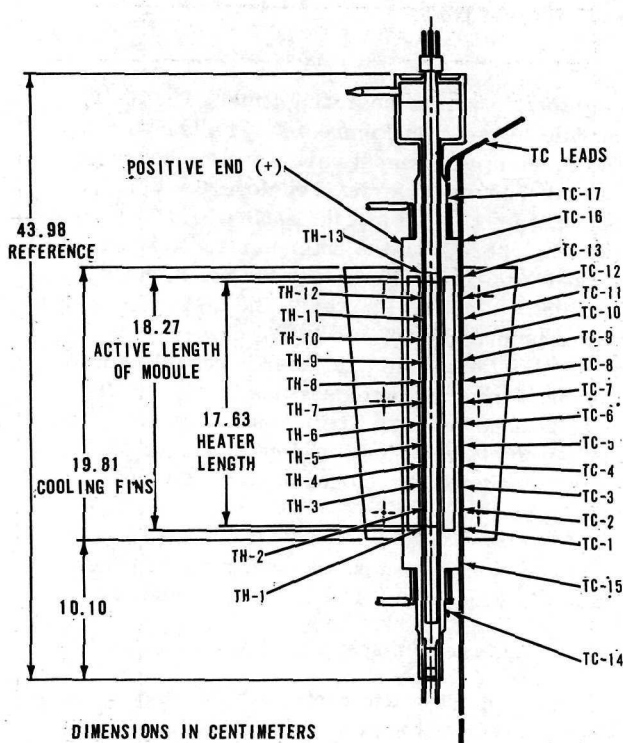


Figure 15. Overall dimensions and thermocouple installation — TEM-9U module.

Also shown in Figure 16 is an MSFC-built programmable electronic load bank. An overall schematic of the TEM-9U test arrangement is shown in Figure 17.

Module current flow can be controlled by an input voltage signal equal to one-tenth of the desired current. Provisions exist for inputs of either a constant voltage, a square wave voltage at 0.002 to 10 000 Hz, or a sine wave voltage at 1 to 100 000 Hz.

The data acquisition system includes an integrating digital voltmeter, clock, printer, two 25-channel scanners, and a tape punch. Table 5 lists measured data and calculated data.

Test Description

OPERATING CONDITIONS

The module is presently being operated at a nominal average hot side temperature of 538°C (1000°F) with the cold side temperature at approximately 200°C (392°F) when at matched load (internal resistance = external circuit resistance). The air flow rate is maintained constant. For parametric tests in which the load resistance is varied to established performance parameters versus load,

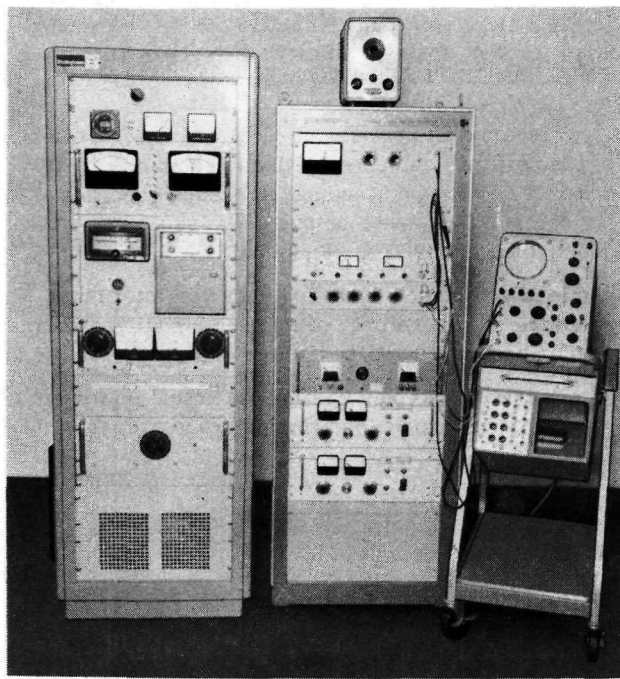


Figure 16. TEM-9U test console and electronic load bank.

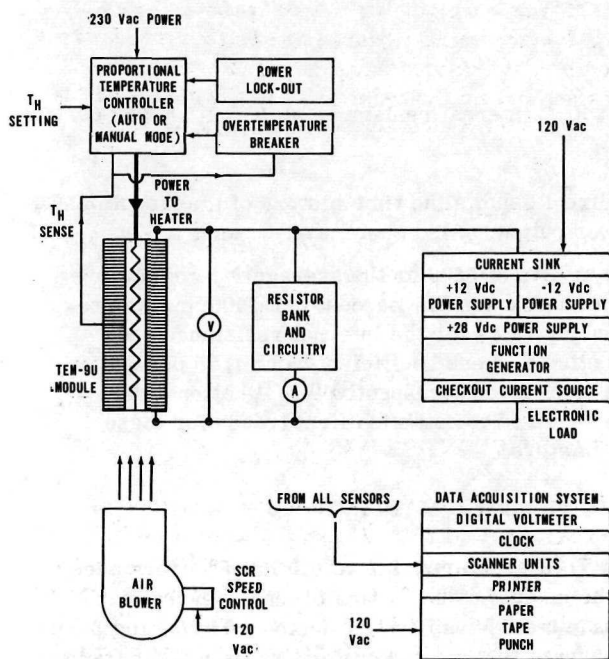


Figure 17. Simplified schematic of TEM-9U test arrangement.

TABLE 5. TEM-9U DATA ACQUISITION AND REDUCTION

Measured Data	Symbol
Hot Side Temperatures (11 points)	T_H
Cold Side Temperatures (13 points)	T_C
Load Voltage	V_L
Load Current	I_L
Main Heater Input Power	Q_M
Instantaneous Open Circuit Voltage	V_{OC}
Blower Speed	B_S
Inlet Air Temperature	T_I
Calculated Data	Symbol
Average Hot Side Temperature ($^{\circ}\text{C}$)	\overline{T}_H
Average Cold Side Temperature ($^{\circ}\text{C}$)	\overline{T}_C
Power Output (W)	P_O
Module Average Temperature	T_{AVE}
Internal Resistance (Ω)	R_g
Effective Seebeck Coefficient ($\text{V}/^{\circ}\text{C}$)	α
Module Thermal Conductance ($\text{W}/^{\circ}\text{C}$)	k
Module/Air Heat Transfer Coefficient ($\text{W}/^{\circ}\text{C}$)	C
Normalized R_g	R_{gn}
Normalized α	α_n
Normalized Power Output	P_N

both the hot side and cold side temperatures vary according to Peltier heat pumping (which is a function of current). Two operating modes are used. One is the "constant Q_M " mode in which input power is held constant and the modular temperatures vary with current level. The other is the "constant T_H " mode in which a proportional controller maintains the hot side temperature constant by varying the input power Q_M as the current is changed. In both modes, the blower speed is held constant to maintain a reference heat rejection condition. During endurance testing, the constant T_H mode is used.

ENDURANCE TESTING

Of primary interest is the way in which module performance degrades with time because of physical changes in the lead-telluride couples. Past development history has shown that performance changes can occur because of thermal distortion and/or intercouple diffusion of tellurium. Measurable parameters that reflect such changes are (1) module internal resistance, (2) effective Seebeck coefficient, and (3) module thermal conductivity. Endurance testing reveals the way in which these key parameters change with time.

PERFORMANCE TESTING

Various performance tests have been conducted at selected intervals during the endurance test. These were:

1. Parametric tests — The load current is varied in steps, and after module temperatures have stabilized, all parameters are measured. The results are plotted versus load current. Either the constant T_H or the constant Q_M mode is used.
2. Impedance measurement — The module current is varied sinusoidally at various frequencies and with a constant current amplitude. V_{RMS} and I_{RMS} are measured, and the resulting impedance is plotted versus frequency.
3. Transient response — While in the constant Q_M mode, the current is varied in a square wave manner, and the module response is measured.

Test Results

ENDURANCE TEST (0 TO 5600 HR)

Since module power output is a strong function of temperature and external load resistance, it is desirable to have a standard reference condition for determining power output. The reference condition used is based on $\bar{T}_H = 538^\circ\text{C}$, $\bar{T}_C = 200^\circ\text{C}$, and load resistance equal to generator internal resistance. Therefore, after each module performance check, a normalized power output P_N is determined based on adjusting the actual power output to the reference condition using

$$P_N = \frac{\alpha^2 (\bar{T}_H - \bar{T}_C)^2}{4R_g} ,$$

where

α = effective Seebeck coefficient at

$$T_{AVE} = \frac{T_H + T_C}{2} = 369^\circ\text{C}$$

and

$$R_g = \text{internal resistance at } T_{AVE} = 369^\circ\text{C} .$$

Figure 18 shows the time history of the module power output. Also shown are α and R_g at 369°C . As of 5600 hr the average rate of power degradation was 0.7 percent per 1000 hr. Corresponding rates for the internal resistance and effective Seebeck coefficient were 1.25 percent and 0.25 percent, respectively. Additional data are required to establish firm trends for these parameters.

PERFORMANCE MAPPING

To characterize the equilibrium performance of the module as a function of load, several parametric tests have been conducted. During the initial 3600 hr of testing, the current range was limited to approximately 33 to 37 A. Figure 19 shows a typical parametric test mode at 1400 hr (June 23, 1970)

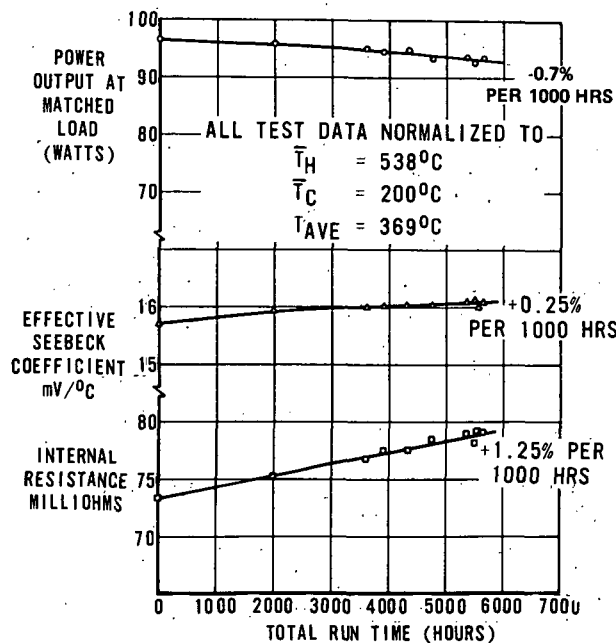


Figure 18. Endurance test results — normalized.

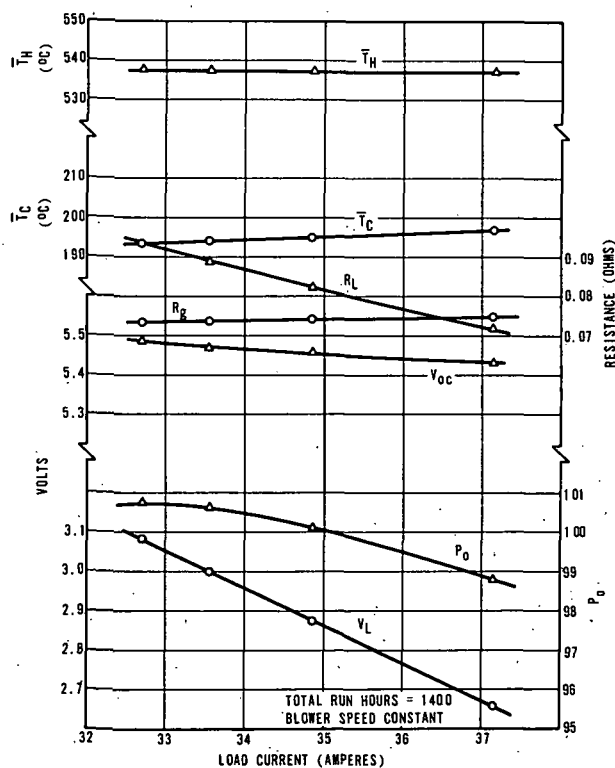


Figure 19. TEM-9U parametric test.

and with constant \bar{T}_H . All parameters are plotted versus load current since current has a major influence on performance because of Peltier and Joule heating effects ($\alpha T_c I$ and $I^2 R_g$). Figure 20 shows a parametric test mode at 3803 hr at constant hot side temperature. As is evident, increasing the current has the following effects:

1. The required input power Q_M increases because of increasing Peltier cooling of the hot junctions (note that Q_M increases almost 30 percent as the current goes from 0 to 45 A).
2. The cold side temperature \bar{T}_C increases because of increased heat flow to the cooling air (constant air flow rate).
3. As the ΔT decreases, the instantaneous open circuit voltage V_{OC} decreases ($V_{OC} = \alpha \Delta T$). This in turn causes the load voltage to decrease at a faster rate.

4. As \bar{T}_C increases, the average module temperature increases causing a rise in the internal resistance R_g , which further contributes to the increasing dropoff of load voltage.

5. Although not shown, the effective Seebeck coefficient decreases slightly with increasing average temperature. However, the actual value, which must be calculated from actual junction temperatures, increases as is normal for lead-telluride.

It should be noted that if \bar{T}_C were forced to remain constant, R_g , α , and V_{OC} also would remain constant, the V-I plot would be a straight line, and the P-I curve would be a true parabola. For this particular run, maximum power was 94.5 W at 3.0 V with an efficiency of 6.15 percent.

When operating with constant input thermal power Q_M , module thermal/electrical performance is somewhat different, as shown in Figure 21. In this mode of operation, increasing current has the following effects:

1. \bar{T}_C changes very little because of the relatively constant heat rejection rate.

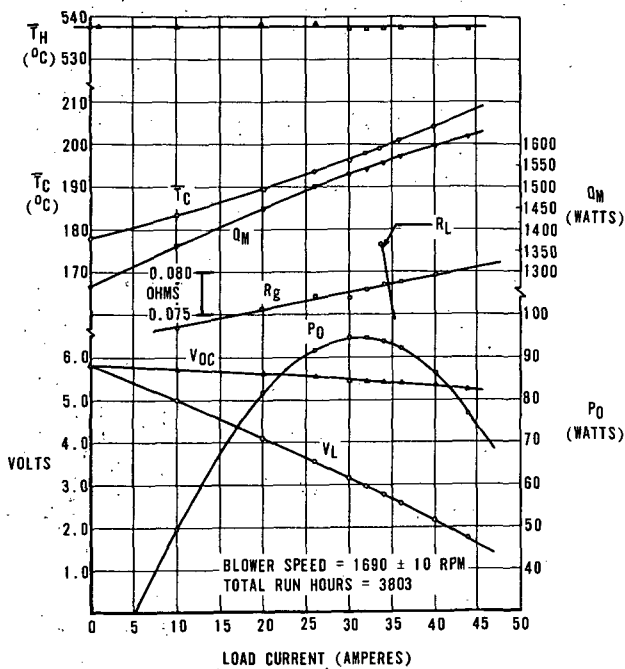


Figure 20. TEM-9U parametric test at constant hot side temperature.

2. T_H decreases sharply because of increasing Peltier cooling of the hot junctions.

3. R_g decreases because of decreasing average temperature.

4. As in the constant T_H mode, V_{OC} decreases because of decreasing ΔT .

5. Because of the preceding effects, V_L decreases at a decreasing rate.

For this test the maximum power was 98 W at 3.4 V with an efficiency of 6.3 percent. Note that for this test the load current was not adjusted below 20 A so as not to exceed a 570°C hot side temperature.

IMPEDANCE TEST

Utilizing the electronic load bank with a sine wave signal input, module impedance was measured as a function of frequency. The results are plotted in Figure 22. Note that above approximately 1000 Hz, the module begins to exhibit inductive reactance. From these data the module inductance at its nominal operating temperature was estimated to be 0.87 μ H.

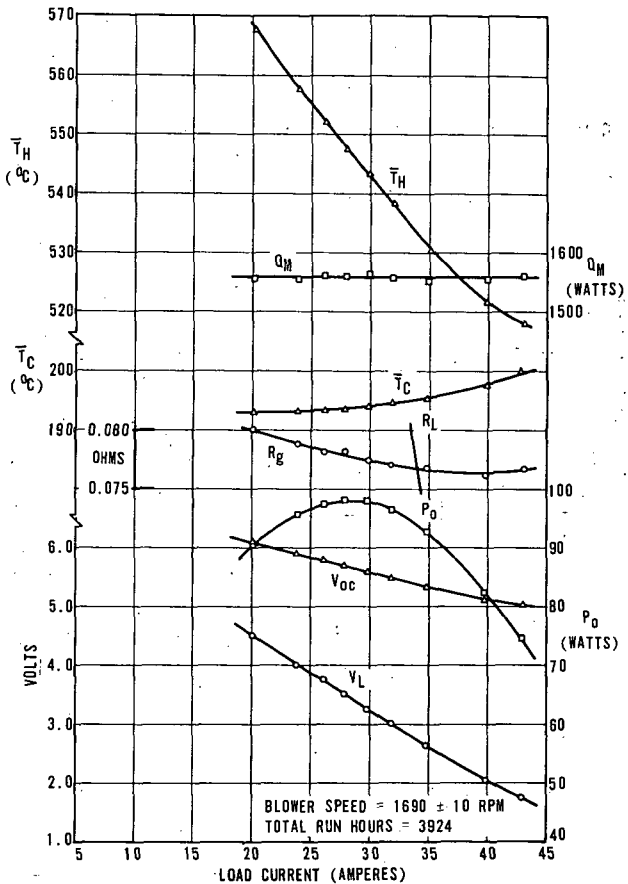


Figure 21. TEM-9U parametric test at constant thermal input.

TRANSIENT RESPONSE TEST

Step Transient. Figure 23 shows the module response to an instantaneous current change from 35 to 30 A, followed by a return to 35 A after a 15-min period. This test was made with constant heat input and starting at stabilized conditions. As shown, the module voltage stabilizes in approximately 3 min (as a result of thermal stabilization at new temperatures). Note that within 1 min after the initial current step the total voltage drift from 3.10 to 3.26 V is approximately 80 percent complete.

Square Wave Transient Test. In this test the module was subjected to a square wave current ripple of 30 ± 5 A at frequencies from 1000 Hz down to 0.1 Hz. The objective was to determine the frequency at which module temperature oscillations become evident. This point was reached at approximately 0.2 Hz where the current dwell period was 2.5 s. The test was conducted with constant heat input.

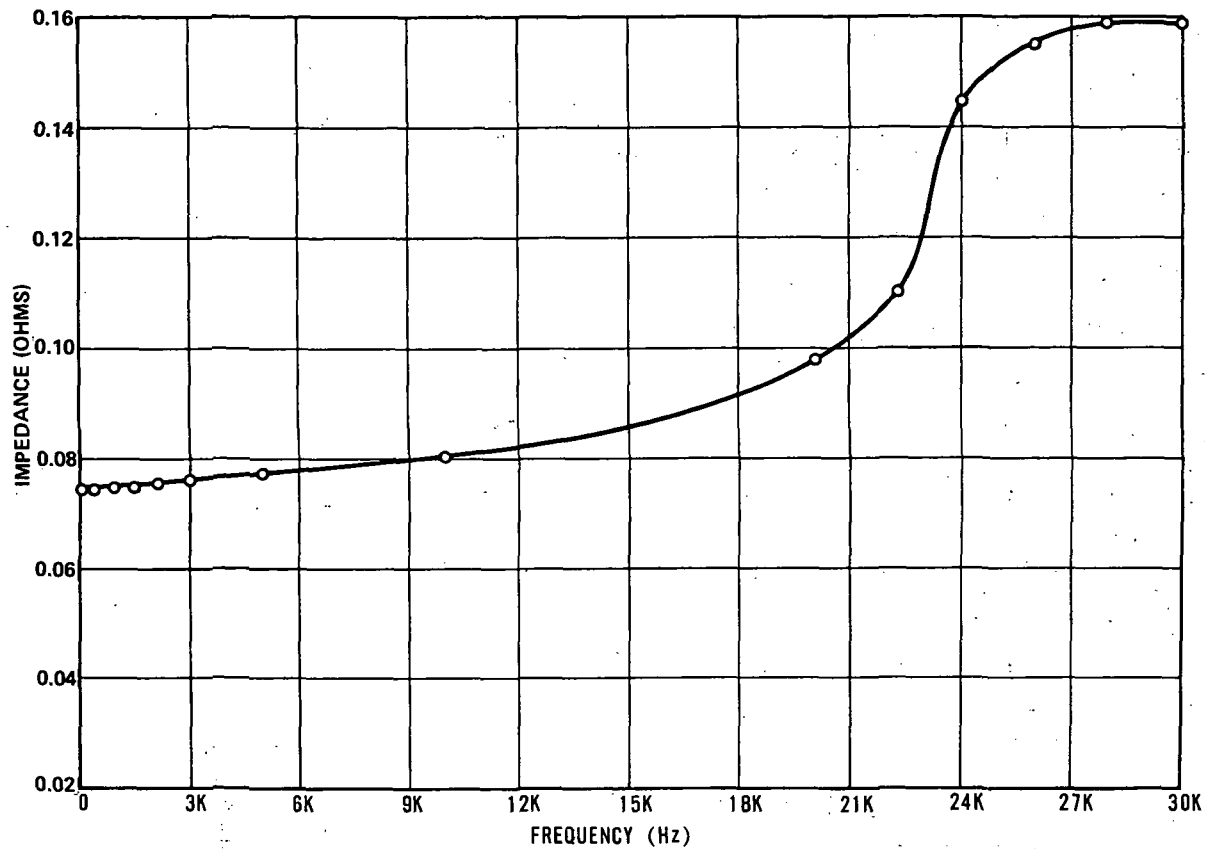


Figure 22. Module impedance versus frequency.

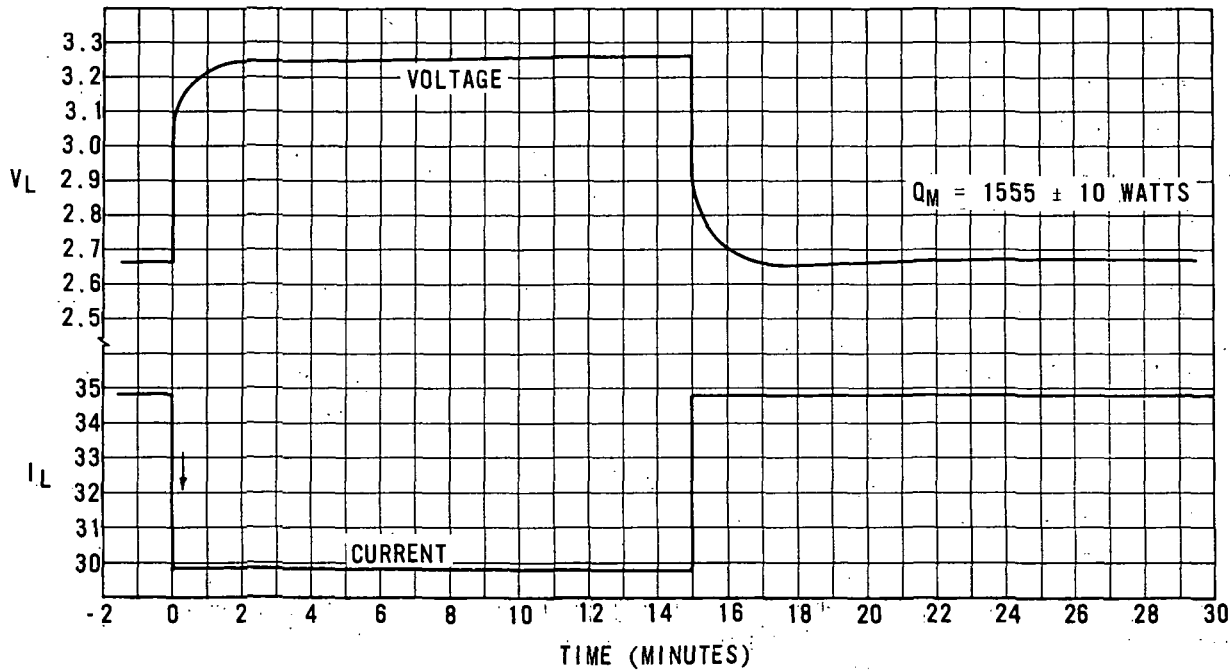


Figure 23. Step transient test.

PRESENT STATUS

At present the module is being endurance tested at near maximum power with a 1000 Hz, ± 5 A current ripple.

Computer Modeling of TEM-9U

As an analytical tool for evaluating the TEM-9U module and for future use in design integration studies, computerized math models are being developed in conjunction with the test program.

The objective is to be able to predict module thermal/electrical performance versus load as a function of (1) module physical properties, (2) specified control parameters, and, (3) coolant inlet conditions. The general approach is to relate K , α , and R_g to module average temperature, T_{AVE} , and to relate these to all other applicable variables using the following basic equations:

$$Q_M = K(T_H - T_C) + \alpha I_L T_H - \frac{1}{2} I_L^2 R_g , \quad (1)$$

$$V_{OC} = \alpha(T_H - T_C) , \quad (2)$$

$$V_L = V_{OC} - I_L R_g , \quad (3)$$

$$T_{AVE} = \frac{T_H + T_C}{2} , \quad (4)$$

$$Q_M = Q_R + I_L V_L , \quad (5)$$

and

$$Q_R = C(T_C - T_i) ; \quad (6)$$

and

$$K = f(T_{AVE}, t) , \quad (7)$$

$$\alpha = f(T_{AVE}, t) , \quad (8)$$

and

$$R_g = f(T_{AVE}, t) ; \quad (9)$$

where

$$Q_M = \text{heat input (W)} ,$$

$$V_{OC} = \text{instantaneous open circuit voltage (Seebeck voltage),}$$

$$V_L = \text{load voltage} ,$$

$$I_L = \text{load current (A)} ,$$

$$Q_R = \text{rejected heat (W)} ,$$

$$C = \text{effective heat transfer coefficient between module cold side and air coolant (W/C)} ,$$

$$T_i = \text{coolant inlet temperature (°K)} ,$$

and

$$t = \text{module operating time, total} .$$

During module testing, linear expressions have been determined experimentally for K , α , R_g and C (C is proportional to blower rpm, hence flow-rate).

MODELS

For the operational case in which cold side temperature and heat input are specified (controlled) and the external load is R_L ohms,

$$V_L = \frac{1}{2} \left\{ \left[\frac{\alpha T_C + \frac{K}{\alpha} (R_L + R_g)}{\frac{2R_L + R_g}{R_L}} \right]^2 + \frac{8Q_M R_L^2}{2R_L + R_g} \right\}^{1/2}$$

$$- \frac{\alpha T_C + \frac{K}{\alpha} (R_L + R_g)}{\frac{2R_L + R_g}{R_L}}$$

which then permits straightforward calculation of current, power, and hot junction temperature. Since α , R_g , and K are functions of $(T_H + T_C)/2$, an iterative approach is used. In summary, the input and output parameters of the computer model are:

<u>Input</u>	<u>Output</u>
T_C	V_L
Q_M	V_{OC}
R_L	I_L
	P_O
T_H	

For the case in which hot side temperature is specified (maintained constant by heat input control) and coolant inlet conditions are specified, a similar approach is used. With this model, a direct simulation of the module operating with the hot junction temperature controller can be made. Input and output parameters are:

<u>Input</u>	<u>Output</u>
T_H	P_O
rpm	V_L
	V_{OC}
T_i	T_C
I_L	Q_M

With this program, the data of Figure 20 have been simulated with 2-percent accuracy.

For the case in which heat input Q_M is specified (maintained constant) and coolant inlet conditions are specified, a program was also prepared to simulate module performance versus load. In this case, as for the SNAP-19 generator, both hot side and cold side temperatures vary with load. Input and output parameters are:

<u>Input</u>	<u>Output</u>
Q_M	P_O
rpm	V_L
T_i	V_{OC}
I_L	T_H
	T_C

Figure 24 shows a comparison of test data and simulated data. In this case the computer program is particularly useful in predicting module performance at temperatures beyond established test limits.

PRESENT STATUS AND FUTURE PLANS

The TEM-9U test program has now progressed to the point where a significant amount of useful data have been obtained and the basic performance and life characteristics of the module have been established. Several thousand additional hours of endurance testing are planned, and further performance testing and computer simulation will be conducted. A study of various control concepts is planned including testing of a peak power tracking technique. Additional future plans include testing of TEM modules operating with flowing NaK, with heat supplied from a simulated reactor heat source.

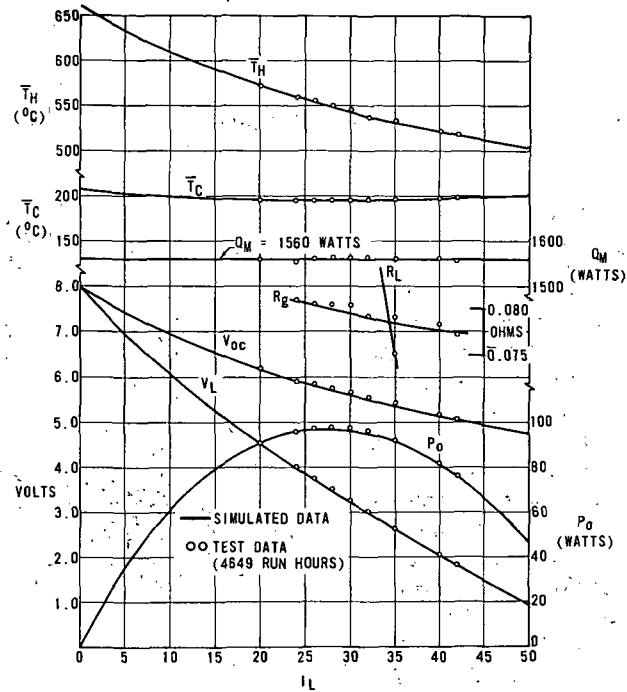


Figure 24. TEM-9U performance with constant heat input — comparison of test data with computer simulation data.

REFERENCES

1. Ganz, D. C.; and Lieberman, A.: SNAP-19 Generator S/N 19 Summary Report On Testing at Martin Marietta Corporation. Martin Marietta Corporation, Nuclear Division Report No. MND-3607-212, Prepared for USAEC (AT (30-1)-3607), Baltimore, Maryland, November 1967.
2. Evaluation of the SNAP-19 Performance on Nimbus III Including Prelaunch Characteristics. Hittman, Associates, Inc. Report No. HIT-407, Prepared for Goddard Space Flight Center (NAS5-11661), Columbia, Maryland, August 15, 1969.

INCREASED HYDROX FUEL CELL PERFORMANCE

By

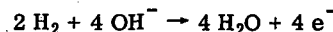
John R. Morgan

INTRODUCTION

Space Shuttle studies have recommended the use of hydrogen-oxygen fuel cells as the primary power source of the Shuttle. Power system requirements clearly indicate that improvements in present fuel cell system technology are required. The power density capabilities attainable by present technology are adequate to meet most proposed mission requirements; however, operating efficiency improvements would greatly reduce system weight since more than 85 percent of a fuel cell power system weight for a typical Shuttle mission is fuel and its tankage. Research is being conducted at the Marshall Space Flight Center (MSFC) to identify system limitations and to investigate methods of reducing these limitations. This report presents a proposed method for improving cathodic efficiency, which is being studied at MSFC.

FUEL CELL MODEL DEVELOPMENT

In simplest form, the hydrogen-oxygen alkaline fuel cell is a pair of complementary chemical reactions occurring at a three-phase interface as shown in Figure 1. The reactant gas comes in contact with the liquid electrolyte at the surface of a solid catalyzed electrode. At the anode, the hydrogen gas reacts at the three-phase interface consuming hydroxyl ions and producing electrons and water as given by the half-cell reaction,



At the cathode, the oxygen gas reaction consumes water and electrons and produces hydroxyl as given by the cathode reaction,

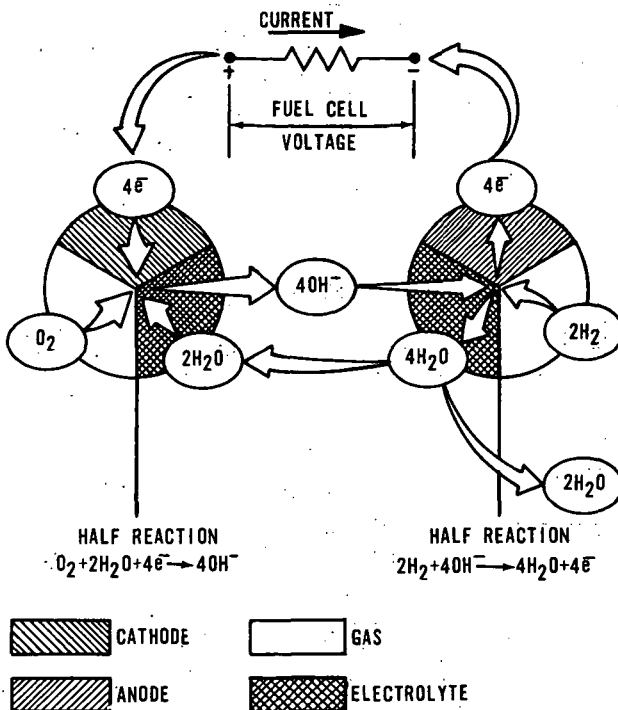
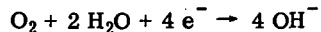


Figure 1. Simplified fuel cell reactions.

In general, the electrolyte serves as the transport medium for the hydroxyl ions and the water molecules between the electrodes.

A typical volt-ampere curve, as shown in Figure 2, illustrates that there are three classifications of losses over the fuel cell performance range. At very low current densities, the losses, as indicated by the sharp initial decrease in terminal voltage, are related to the basic activity of the electrode catalysts. Development of high activity catalysts has been conducted through NASA-funded research since 1962. The internal resistance (IR) polarization region, or the flat portion of the volt-ampere curve, is characterized by the electrolyte concentration and electrolyte containment techniques. Performance in this region can be improved by using

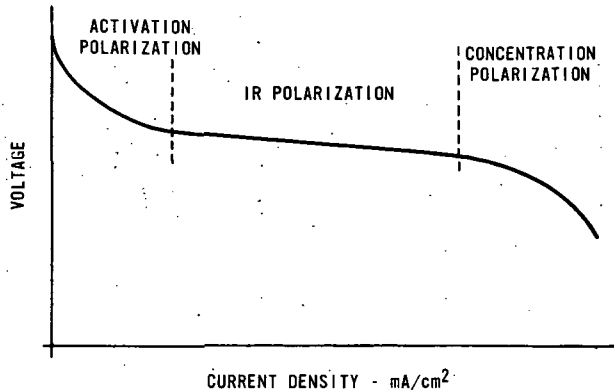


Figure 2. Typical performance curve.

higher electrolyte concentrations within the constraints imposed by cell material. Another method of improving performance within the IR region is to use a thinner and/or more porous electrolyte containment material. At high current densities, performance is limited by concentration deficiencies. At the anode, performance is limited by an excess accumulation of water or a shortage of hydrogen and hydroxyl ions. Cathode performance is limited by a shortage of oxygen and/or water molecules or an excess of hydroxyl ions.

In a closer analysis of the electrode performance, a math model was developed using a simplified pore model of the electrode structure (Fig. 3). Some considerations used in developing the model include pore size variations, pore size distributions, and the fact that the reaction does not occur entirely at the electrolyte meniscus within the pore. A large portion of the reaction occurs after the reactant gas diffuses through the electrolyte to a catalyzed electrode reaction site. A computerized solution of the model revealed that anode polarization losses were very small when compared with cathode polarization. The model shows that the maximum electrode current can be given by

$$I_M = \frac{2eLnFDc}{3R^2 \ln [R/(R-d)]}$$

where

e = electrode porosity ,

L = average pore length (cm) ,

n = "moles" of electrons per mole of reactant consumed ,

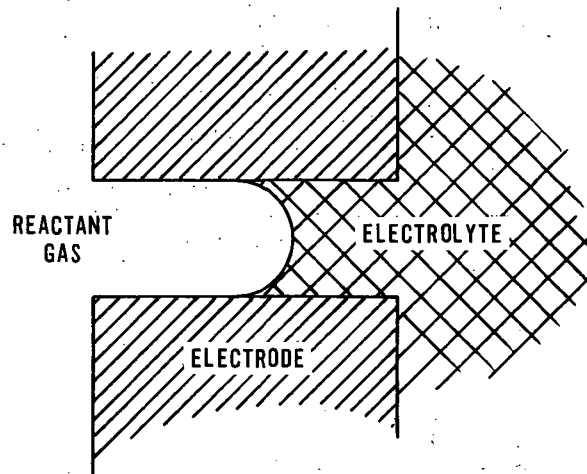


Figure 3. Simplified model of a gas-diffusion electrode.

F = Faraday's constant (coulombs/equivalent) ,

D = reactant gas diffusivity (cm²/s) ,

C = reactant gas solubility (moles/cm³) ,

R = pore radius (cm) ,

and

d = finite electrolyte meniscus thickness (cm) .

The effect of electrolyte concentration on cathode performance was determined by solving the model using the solubility and diffusivity parameters of various electrolyte concentrations. It is noted that these parameters vary inversely with electrolyte concentration for potassium hydroxide (KOH) electrolytes. The results plotted in Figure 4 show improved cathode efficiencies with decreasing KOH concentrations. However, when the total cell performance is modeled, the performance decreases with decreasing KOH concentrations because the ionic conductivity of the electrolyte varies directly with KOH concentration.

LABORATORY TESTING AND RESULTS

Using the model as a basis, laboratory experiments were conducted to analyze cathode efficiency improvements. The test objectives were to increase the cathode efficiency by decreasing the KOH concentration at the three-phase reaction site, while maintaining a high KOH concentration in the bulk

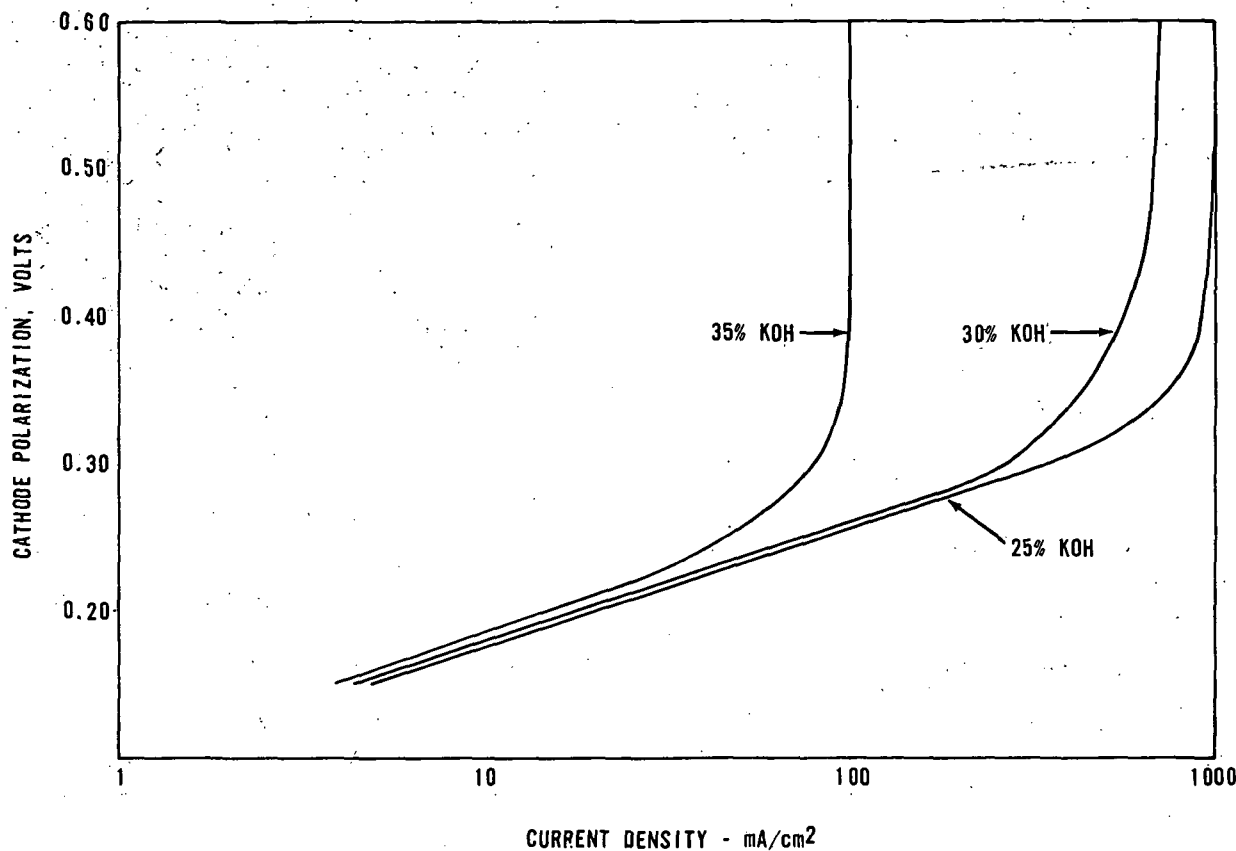


Figure 4. Effect of KOH concentration on cathode polarization.

electrolyte by humidifying the oxygen gas. In addition to improving cathode efficiency in the IR region, cathode concentration polarizations related to water shortages are reduced. Laboratory data for porous gas-diffusion electrode testing (Fig. 5) and thin-film electrode (Fig. 6) testing demonstrate the feasibility of the proposed technique. Testing demonstrates that a 5 to 10 percent performance improvement is possible. Improvements of this magnitude would definitely be advantageous for missions similar to the proposed Space Shuttle profile.

The gas-diffusion fuel cell electrode tests were conducted at MSFC using single-cell hardware developed by Allis-Chalmers. This hardware is representative of the present state-of-the-art capabilities of gas-diffusion electrode fuel cells. The gas-diffusion electrode requires the reactant gas to have a longer diffusion path than does a screen-electrode fuel cell. Since one system being

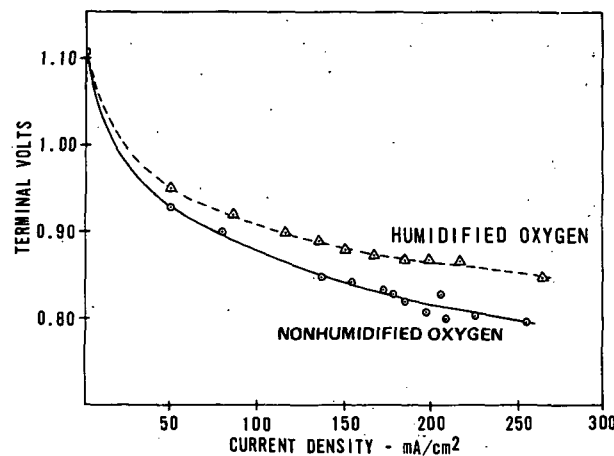


Figure 5. Humidification effects at 363°K using gas-diffusion electrodes.

considered for the Space Shuttle uses a screen electrode, thin-film testing was conducted to

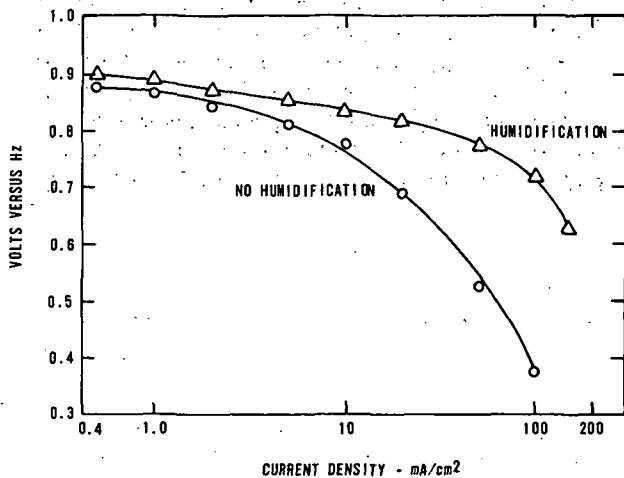


Figure 6. Humidification effects at 373°K using thin-film electrodes.

evaluate the effects of humidification on thinner electrode structures. The thin-film testing was conducted by ESSO Research.

Presently two methods of achieving oxygen humidification are being considered. One method, as shown in Figure 7, uses an external saturator very similar to the test facility used at MSFC. The oxygen would enter a saturator and collection tank that receives water via an automatic vacuum trap from the water removal portion of the fuel cell stack. This tank could also serve as the coolant accumulator for the system. The projected weight increase of such a system is 10 percent, which would result in no power density increase although the total mission fuel requirements could be reduced. This method would have minimal impact on present fuel cell stack designs.

A second concept being considered is electrochemical humidification. This concept can be implemented with no increase in system weight but would result in an impact on present fuel cell stack designs. Electrochemical humidification is best understood by first reviewing fuel cell construction using a static moisture removal technique, as shown in Figure 8. The hydrogen and oxygen gases enter their respective cavities and come in contact with the anode and cathode, respectively, which are separated by the electrolyte and its containment material. Excess water produced at the anode diffuses through the moisture removal membrane to the moisture removal cavity because of concentration gradients. The electrochemical

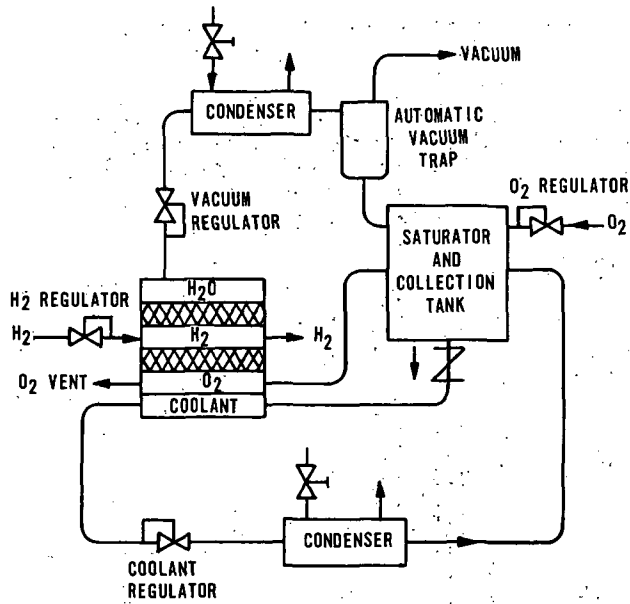


Figure 7. Fuel cell system with external humidifier.

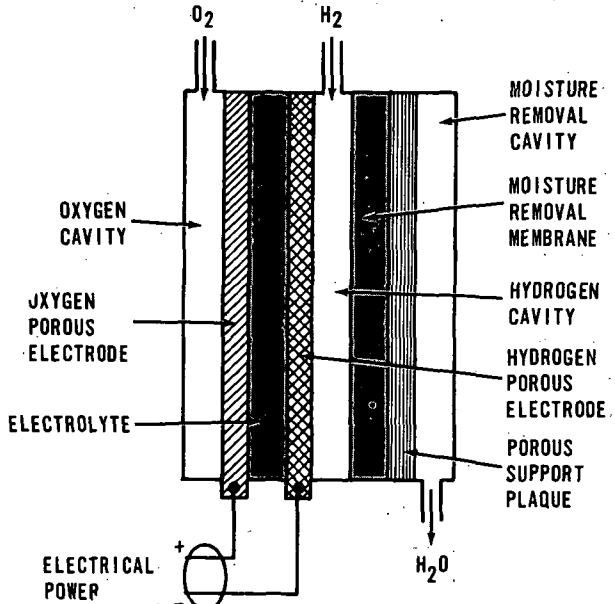


Figure 8. Fuel cell construction using static moisture removal system.

humidifier (Fig. 9) retains the same construction for the reactant gas chambers with the oxygen passing through its cavity as was previously used for the

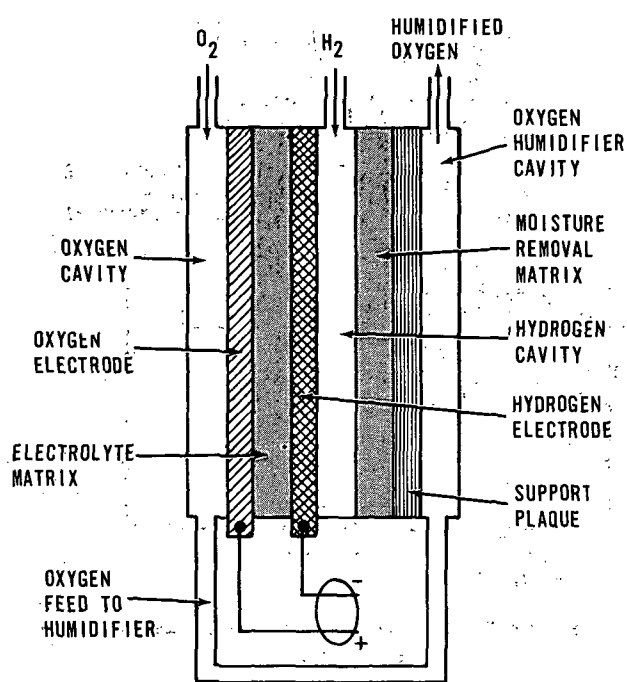


Figure 9. Fuel cell construction using integral oxygen humidifier.

moisture removal cavity. Less than one-fifth of the cells in a fuel cell stack would need to be electrochemical humidifiers to supply the quantity and quality of humidified oxygen required for the remainder of the stack. Obviously the humidifier cells will operate at lower efficiencies and higher stress levels than the remainder of the cells.

CONCLUSIONS AND FUTURE PLANS

Analytical and experimental data demonstrate the advantages and feasibility of oxygen humidification as a method of increasing cathode efficiency. Additional testing is being conducted to evaluate humidification effects on life characteristics of gas-diffusion fuel cells. Another test program is being planned to investigate the life capabilities of an electrochemical-humidifier cell as a function of current density and humidified oxygen output. If a humidifier cell can be developed that has adequate life capabilities (3000- to 6000-hr lifetime), a small stack will be constructed using an integrated humidifier technique.

Page intentionally left blank

HIGH FREQUENCY DC-TO-DC CONVERSION

By

R. M. Acker

INTRODUCTION

The push-pull dc-to-dc converter shown in Figure 1 is used in many aerospace applications. Its main function is to convert power at one voltage level to power at another voltage level and to provide isolation between the input and output voltages. Converters of this type range in size from a few hundred milliwatts to more than a kilowatt.

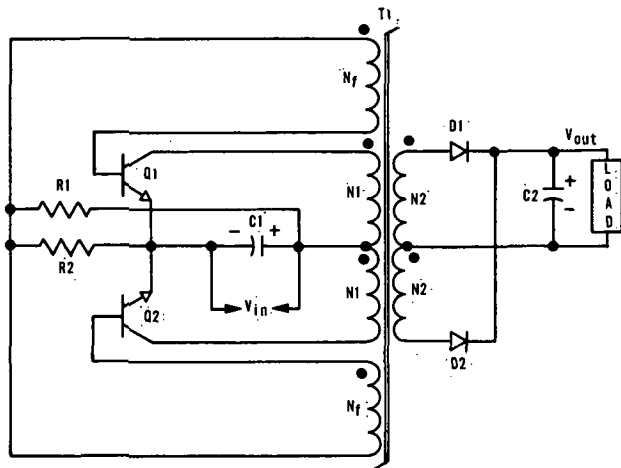


Figure 1. Dc-to-dc converter no. 1.

An effort has been initiated to standardize the circuit design, packaging, and fabrication of these converters and at the same time reduce their size and weight. By operating these converters in the frequency range of 50 to 100 kHz, instead of the 5 to 10 kHz normally used in most converters, a reduction in size and weight can be realized. With proven circuit designs, modular packaging, and controlled fabrication techniques, a family of highly reliable dc-to-dc converters can be made available for future space programs.

ACCOMPLISHMENTS

To date, efforts have been directed toward using 28 Vdc as the input and output voltage, with loads of

from 1 to 2 A and an operating frequency of 100 kHz. The advantages of high frequency operation are reductions in size, weight, and filtering capacitance. Reliable power semiconductors are becoming available today that permit the production of converters having operating efficiencies greater than 90 percent at 100 kHz. Studies conducted on lower (50 kHz) and higher (200 kHz) frequencies did not lead to significant package size changes, since the power transformer is the main variable under these conditions.

The circuit shown in Figure 2 is a result of the latest efforts and is a modified version of the previous circuit. The principle of operation is different in that the inductor L1 is designed to saturate before the main transformer saturates, thereby forcing the switching of transistors Q1 and Q2 by removing their base drive. In Figure 1, T1 has to saturate to remove the base drive from the transistors. By switching Q1 and Q2 without T1 saturating, large current transients in the collector circuits are eliminated, thus enabling the transistors to operate more efficiently and reliably with a reduction in generated electromagnetic interference.

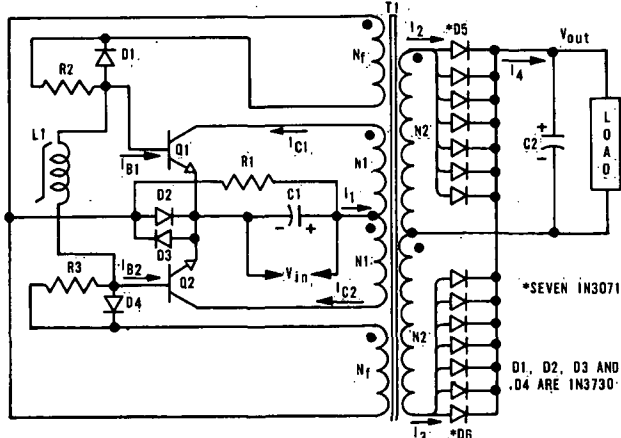


Figure 2. Dc-to-dc converter no. 2.

The transformer used in this converter is constructed with a toroid core of ferrite that has very

low losses when operated at 100 kHz. L1 is a bobbin-wound toroid constructed of 31.75×10^{-7} m (0.125 mil) nickel-iron tape. When the transformer is designed for efficient high frequency operation, the volts-per-turn ratio is a major consideration. If this ratio is large (greater than 1 V per turn), the number of turns in the feedback (or base drive) winding is difficult to adjust for efficient biasing of Q1 and Q2. Also, it becomes difficult to adjust the number of turns in the output windings for an output voltage less than the input voltage. Consequently, to maintain efficient operation, a reasonable volts-per-turn ratio must first be established; then the size of the power transformer becomes more a function of power and voltage to be converted. During the development of this circuit, it was necessary to incorporate diodes D2 and D3 for proper operation of L1. D2 along with D1 and D4 reduces the turnoff time of Q1 and Q2 and at the same time enables startup of the converter. D3 provides a path for base current to flow when Q1 or Q2 is conducting.

The converter is designed to deliver 50 W at 28 Vdc and is being built in an 82 cm^3 volume using cord-wood construction. To maintain a 90 percent efficiency, either IN3730 or IN3071 diodes are used because of their fast recovery time. Transistors Q1 and Q2 are special SDT6115 types that are specified to have a breakdown voltage of 65 V minimum and a V_{CE} saturation of 0.5 V maximum at $I_C = 4 \text{ A}$ and $I_B = 0.4 \text{ A}$. The f_T should be 350 to 450 MHz. The windings N1 and N2 of T1 are each composed of seven strands of number 30 AWG wire. This construction provides a larger surface to reduce losses resulting from skin effect at high frequencies and provides a separate effective winding for each diode.

The waveforms shown in Figure 3 illustrate the collector voltages of the transistors, V_{CE1} and V_{CE2} , and current waveshapes, I_{C1} and I_{C2} , along with the base current waveshapes of the transistors, I_{B1} and I_{B2} . The collector current has a ramp or saw-toothed shape, which is primarily a result of the recovery or switching times of the transistors and output rectifiers. The transistors used to obtain these waveforms have an f_T of 150 MHz. In using transistors and rectifiers that will switch faster, the collector current will be more square in shape, giving a smaller peak-to-average ratio. The efficiency of the converter increases as the peak current comes closer to being equal to the average current. There

is an additional increase in efficiency as the switching time is reduced. With the combination of faster transistors and diodes, the converter's efficiency can approach 95 percent.

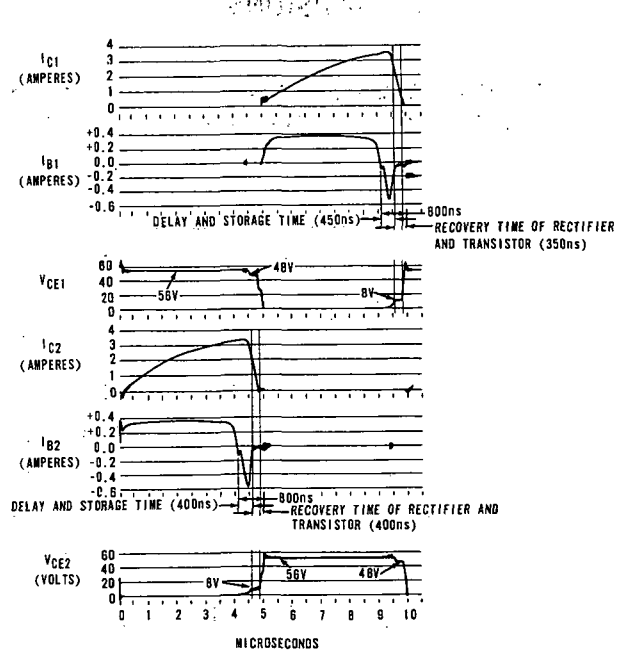


Figure 3. Transistor voltage and current waveshapes.

FUTURE EFFORTS

Future efforts to improve this converter will include using transistors with faster switching times, and the use of Schottky barrier diodes. The Schottky barrier diode has a lower forward drop (approximately 0.5 V) and a faster recovery time (less than 5 ns). Only a few companies have worked with this diode in microwave applications. Consequently, the diodes are not presently available for use as power rectifiers. Currently, two companies are developing Schottky barrier diodes for rectifier application, and by June 1971, these devices should be available for use in the push-pull dc-to-dc converter. The addition of the Schottky barrier rectifier will improve the efficiency of the 50-W converter from 2 to 4 percent.

To further decrease package size and still maintain or increase the reliability of the present converters, future efforts will use the hybrid multilayer

thick-film and thin-film techniques that are now state-of-the-art in many areas of electronics.

CONCLUSIONS

The work effort to date has proven the feasibility of reliable high frequency push-pull dc-to-dc power

conversion. With faster switching transistors (f_T greater than 350 MHz) and Schottky barrier diodes, conversion efficiencies of 95 percent may be achieved. By using hybrid multilayer thick- and thin-film packaging techniques along with high frequency design, a family of high reliability standardized dc-to-dc converters that are small in size can be developed for aerospace applications.

February 1972

APPROVAL

NASA TM X-64642

RESEARCH ACHIEVEMENTS REVIEW
VOLUME IV REPORT NO. 4

The information in these reports has been reviewed for security classification. Review of any information concerning Department of Defense or Atomic Energy Commission programs has been made by the MSFC Security Classification Officer. These reports, in their entirety, have been determined to be unclassified.

These reports have also been reviewed and approved for technical accuracy.

F. B. Moore

F. B. MOORE
Director, Astrionics Laboratory

1. Report No. NASA TM X-64642	2. Government Accession No.	3. Recipient's Catalog No.	
4. Title and Subtitle RESEARCH ACHIEVEMENTS REVIEW, VOL. IV, REPORT NO. 4 Electrical Power Systems Research at MSFC		5. Report Date February, 1972	
		6. Performing Organization Code	
7. Author(s) C. B. Graff, Roy Lanier, Jr., J. L. Miller, W. L. Crabtree, L. E. Paschal, Robert Kapustka, W. J. Robinson, L. E. Young, J. R. Morgan, and R. M. Acker		8. Performing Organization Report No.	
		10. Work Unit No.	
9. Performing Organization Name and Address George C. Marshall Space Flight Center Marshall Space Flight Center, Alabama 35812		11. Contract or Grant No.	
12. Sponsoring Agency Name and Address National Aeronautics and Space Administration Washington, D.C. 20546		13. Type of Report and Period Covered Technical Memorandum	
15. Supplementary Notes Prepared by Astrionics Laboratory, Science and Engineering		14. Sponsoring Agency Code	
16. Abstract Recent research in electrical power systems has been concentrated on the Skylab, Space Station, and Space Shuttle equipment. Research has been initiated into new and improved concepts of electrical power generation and conversion, to meet the predicted requirements for the reusable Space Shuttle and the Space Station. The sequence and contents of the 10 papers in this review of Electrical Power Systems Research at MSFC are as follows:			
<ol style="list-style-type: none"> 1. The operation of the Apollo Telescope Mount and Airlock Module electrical power systems, their unique features, and the technology required to develop them are presented. 2. The effect of "hot spots" and "voltage breakdowns" caused by open or shadowed cells in the OWS is analyzed. 3. The use of the solar cell characteristic curve for the checkout of large area solar arrays is presented. 4. A nickel-cadmium battery investigation conducted to determine optimum and acceptable battery performance within the Skylab mission requirements is presented. 5. Various approaches for electrical load sharing between dc power modules, operating in parallel, are discussed with emphasis on the solution used for the ATM electrical power system. 6. Transmission of several hundred watts of microwave power over a distance of 76.2 to 101.6 cm (30 to 40 ft) to a 12.70 by 17.78 cm (5 by 7 ft) collector antenna is described. 			
Continued			
17. Key Words (Suggested by Author(s)) Apollo Telescope Mount nickel-cadmium battery Airlock Module load sharing electrical power systems microwave power Orbital Workshop thermoelectric generator solar cell fuel cell solar arrays dc-to-dc converter		18. Distribution Statement Unclassified — Unlimited <i>John J. Hopkins STE-R, MSFC</i>	
19. Security Classif. (of this report) Unclassified	20. Security Classif. (of this page) Unclassified	21. No. of Pages 120	22. Price* \$3.00

7. A study to generate criteria for the design of a 45 kWe solar array for use on the lunar surface is discussed. Developmental test hardware is described and results of testing are given.

8. The status and results of two thermoelectric generator test programs are considered. A SNAP-19 radioisotope thermoelectric generator and a compact thermoelectric module, TEM-9U, are evaluated.

9. Primary losses within low temperature, alkaline hydrogen-oxygen fuel cells are related to oxygen electrode polarization. The performance improvements obtained by humidification of the reactant gases are derived and the results as verified by single cell testing are explored.

10. The development of a 100-kHz dc-to-dc converter is described. Inherent advantages of high frequency operation, techniques used, and components developed to allow 100-kHz switching frequencies are discussed.

Page Intentionally Left Blank

CALENDAR OF REVIEWS

FIRST SERIES (VOLUME I)

REVIEW	DATE	RESEARCH AREA	REVIEW	DATE	RESEARCH AREA	REVIEW	DATE	RESEARCH AREA
1	2/25/65	RADIATION PHYSICS	9	6/24/65	GROUND TESTING	16	10/28/65	ASTRODYNAMICS
2	2/25/65	THERMOPHYSICS	10	6/24/65	QUALITY ASSURANCE AND CHECKOUT	17	1/27/66	ADVANCED TRACKING SYSTEMS
3	3/25/65	CRYOGENIC TECHNOLOGY	11	9/16/65	TERRESTRIAL AND SPACE ENVIRONMENT	18	1/27/66	COMMUNICATIONS SYSTEMS
4*	3/25/65	CHEMICAL PROPULSION	12	9/16/65	AERODYNAMICS	19	1/6/66	STRUCTURES
5	4/29/65	ELECTRONICS	13	9/30/65	INSTRUMENTATION	20	1/6/66	MATHEMATICS AND COMPUTATION
6	4/29/65	CONTROL SYSTEMS	14	9/30/65	POWER SYSTEMS	21	2/24/66	ADVANCED PROPULSION
7	5/27/65	MATERIALS	15	10/28/65	GUIDANCE CONCEPTS	22	2/24/66	LUNAR AND METEOROID PHYSICS

SECOND SERIES (VOLUME II)

REVIEW	DATE	RESEARCH AREA	REVIEW	DATE	RESEARCH AREA	REVIEW	DATE	RESEARCH AREA
1	3/31/66	RADIATION PHYSICS	6	1/26/67	CHEMICAL PROPULSION	10	9/28/67	TERRESTRIAL AND SPACE ENVIRONMENT
2	3/31/66	THERMOPHYSICS	7	3/30/67	CRYOGENIC TECHNOLOGY	11	11/30/67	MANUFACTURING
3	5/26/66	ELECTRONICS	8**	5/25/67	COMPUTATION	12	1/25/68	INSTRUMENTATION RESEARCH FOR GROUND TESTING
4	7/28/66	MATERIALS	9	7/27/67	POWER SYSTEMS			
5	9/29/66	QUALITY AND RELIABILITY ASSURANCE						

THIRD SERIES (VOLUME III)

REVIEW	DATE	RESEARCH AREA	REVIEW	DATE	RESEARCH AREA	REVIEW	DATE	RESEARCH AREA
1	3/28/68	AIRBORNE INSTRUMENTATION AND DATA TRANSMISSION	5	11/21/68	COMMUNICATION AND TRACKING	10	12/18/69	MATERIALS RESEARCH FOR SHUTTLE AND SPACE STATION
2	5/22/68	ASTRODYNAMICS, GUIDANCE AND OPTIMIZATION	6	1/30/69	THERMOPHYSICS	11	1/29/70	MICROELECTRONICS RESEARCH FOR SHUTTLE AND SPACE STATION
3	7/25/68	CONTROL SYSTEMS	7	3/27/69	RADIATION PHYSICS	12	3/26/70	COMPUTATION RESEARCH (PART I)
4	9/26/68	AEROPHYSICS	8	6/26/69	METEOROID PHYSICS			
			9	9/25/69	COMPUTATION RESEARCH (PART II)			

FOURTH SERIES (VOLUME IV)

REVIEW	DATE	RESEARCH AREA	REVIEW	DATE	RESEARCH AREA	REVIEW	DATE	RESEARCH AREA
1	5/28/70	STRUCTURES	4	3/25/71	ELECTRICAL POWER SYSTEMS	6	8/5/71	CHEMICAL PROPULSION
2	10/29/70	CRYOGENICS	5	5/27/71	QUALITY AND RELIABILITY ASSURANCE	7	9/28/71	PRODUCT ENGINEERING AND PROCESS TECHNOLOGY
3	11/19/70	INSTRUMENTATION				8	12/2/71	AEROSPACE ENVIRONMENT

*Classified. Proceedings not published.

**Proceedings summarized only.

Correspondence concerning the Research Achievements Review Series should be addressed to:
Research Planning Office, S&I-R, Marshall Space Flight Center, Alabama 35812